A Numerical and Experimental Study of Additively Manufactured Compact Cold Plates for Electronics Cooling Applications

by

Zane Lee Oligee

A thesis submitted to the Graduate Faculty of
Auburn University
in partial fulfillment of the
requirements for the Degree of
Master of Science

Auburn, Alabama
December 11, 2021

Keywords: Additive Manufacturing, Heat Transfer, Compact Heat Exchanger, CFD

Approved by

Dr. Roy W. Knight, Chair, Associate Professor Emeritus of Mechanical Engineering
Dr. Nicholas Tsolas, Co-chair, Assistant Professor of Mechanical Engineering
Dr. Mark Hoffman, Assistant Professor of Mechanical Engineering

Abstract

This research assesses the viability of metal Additive Manufacturing (AM) to create Compact Cold Plate Heat Exchangers. Unique arrays of offset strip fins were used to increase heat transfer and reduce pressure drop. Cold plates were manufactured utilizing a Laser-Powder Bed Fusion (L-PBF) AM process. Numerical simulations were performed in ANSYS Fluent to predict performance of novel fin array designs. A dimensionless ratio including thermal and hydrodynamic performance, j/f_{app}, was found for each array to quantify changes in heat transfer and pressure drop. Results indicate a 20% increase in j/f_{app} for the 200µm-300µm fin array when compared to the baseline geometry. Experiments were performed with the printed samples and the measured f_{app} across each of the cold plates was found to be between 3% and 46% above simulation predictions. Print orientation was found to have a significant effect on print quality and pressure loss across the final product. Overall, AM is a promising method for producing cold plates; however, thermal performance must be characterized before widespread industry adoption can occur.

Acknowledgements

I would like to thank the members of my advisory committee: Dr. Roy Knight, Dr. Nicholas Tsolas, and Dr. Mark Hoffman. I would especially like to thank Dr. Roy Knight for his tutelage, patience, and commitment to quality over the course of this project. I would also like to thank Dr. Bart Prorok for his assistance in obtaining the many x-ray CT scans utilized in this study.

Thank you to Dr. Don George, Dr. Joel Johnson, and Peter Fassman for their constant support, feedback, and willingness to share their extensive knowledge.

As always, I would like to thank my family and friends whose support has meant so much to me these years.

Table of Contents

List of Figures:

List of Tables:

Nomenclature:

Acronyms:

AM	Additive Manufacturing
BC	Boundary Condition
BP	Build Plate
CFD	Computational Fluid Dynamics
CT	Computed Tomography
DFAM	Design For Additive Manufacturing
FMEA	Failure Modes and Effects Analysis
HTC	Heat Transfer Coefficient
MUSCL	Monotone Upstream-Centered Scheme for Conservation Laws
NDE	Non-Destructive Evaluations
PAO	Polyalphaolefin
PETG	Polyethylene Terephthalate Glycol
PSV	Principle Solution Variant
SOP	Standard Operating Procedure
SOW	Statement of Work

TIM	Thermal Interface Material
TSM	Taylor Series Method
WEG	Water Ethylene Glycol

English Letter Symbols:

Ac	Cross-sectional area
A	Surface area
c_p	Specific Heat
f_f:	Fanning Friction Factor
f_{app}	Apparent Fanning Friction Factor
h	Fin height
$\bar{h}$	Average Convective Heat Transfer Coefficient
l	Fin length
k	Conductivity
L	Cold plate length
$\dot{m}$	Mass flow rate
Nu	Nusselt number
Pr	Prandtl number

Re	Reynolds number
s	Channel width
T	Temperature
t	Fin thickness
$u_{flow\ rate}$	Uncertainty in flow rate sensor
$u_{pressure}$	Uncertainty in pressure sensor
W	Cold plate width

Greek Letter Symbols:

α	Thermal diffusivity
$\bar{\alpha}$	Dimensionless fin parameter based on fin height and spacing
$\bar{\delta}$	Dimensionless fin parameter based on fin thickness and length
$\bar{\gamma}$	Dimensionless fin parameter based on fin thickness and spacing
ρ	Density of working fluid
Θ	Dimensionless thermal resistance
σ_L	Standard deviation in length of cold plate
σ_{Dh}	Standard deviation in hydraulic diameter

$\sigma_{\Delta P}$	Standard deviation in pressure loss
σ_{ρ}	Standard deviation in fluid density
σ_{μ}	Standard deviation in fluid viscosity
μ	Dynamic viscosity of working fluid
ν	Kinematic viscosity of working fluid

Subscripts:

app	Apparent
channel	Channel
h	Hydraulic
f	Fluid

Chapter 1: Introduction

1.1 Compact Heat Exchangers and Cold Plates

Today the ability to fit an ever increasing number of electrical components into significantly smaller housings has driven the need for enhanced cooling solutions. Compact heat exchangers can provide a high rate of heat removal with a minimal footprint. However, further improvements to Compact Heat Exchangers will need to be made to match the cooling requirements set by advances in electronics packaging technologies.

The term Heat Exchanger refers to a device that transfers heat from a hot fluid to a cold fluid, and they are further classified by their size, flow arrangement, and construction [1]. Heat Exchangers are classified as "compact" when their surface area available for heat transfer to volume ratio exceeds 700 m^2/m^3 (213 ft^2/ft^3) [5]. Several examples of different core arrangements for Compact Heat Exchangers are shown in **Figure 1.**

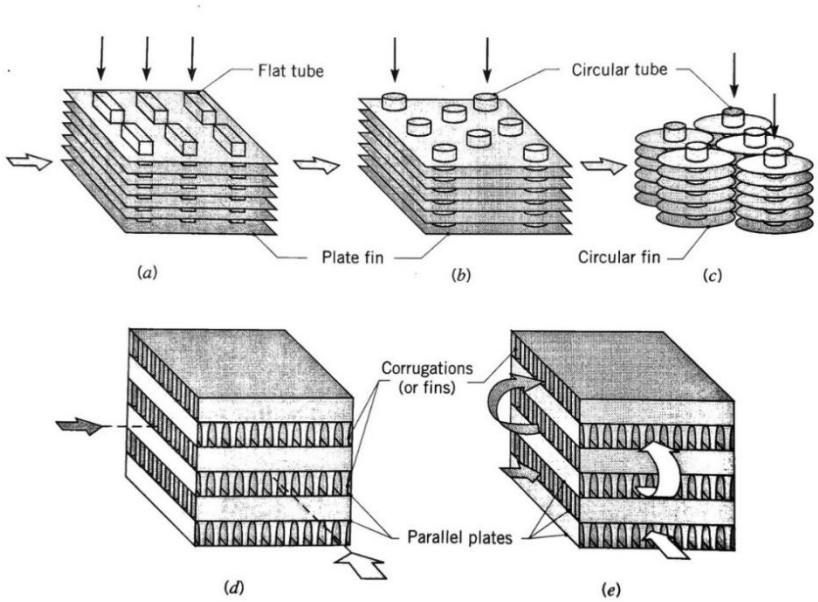

Figure 1: Examples of Secondary Surfaces for Cold Plates: (a) Lanced Offset Strip Fins, (b) Rectangular Channel Fins, (c) Wavy Channel Fins, (d) Elliptical Pin Fins, (e) Rectangular Offset Strip Fins [3]

Cold plates are devices that transfer heat from a “hot” surface, frequently some electronic package, to a working fluid; this working fluid is usually part of a larger liquid cooling system. To increase cooling capabilities, cold plates aim to increase the amount of surface area exposed to the fluid. This is done through the addition of secondary surfaces, commonly arrays of fins, to the flow path. Several examples of secondary surfaces are shown in **Figure 2**.

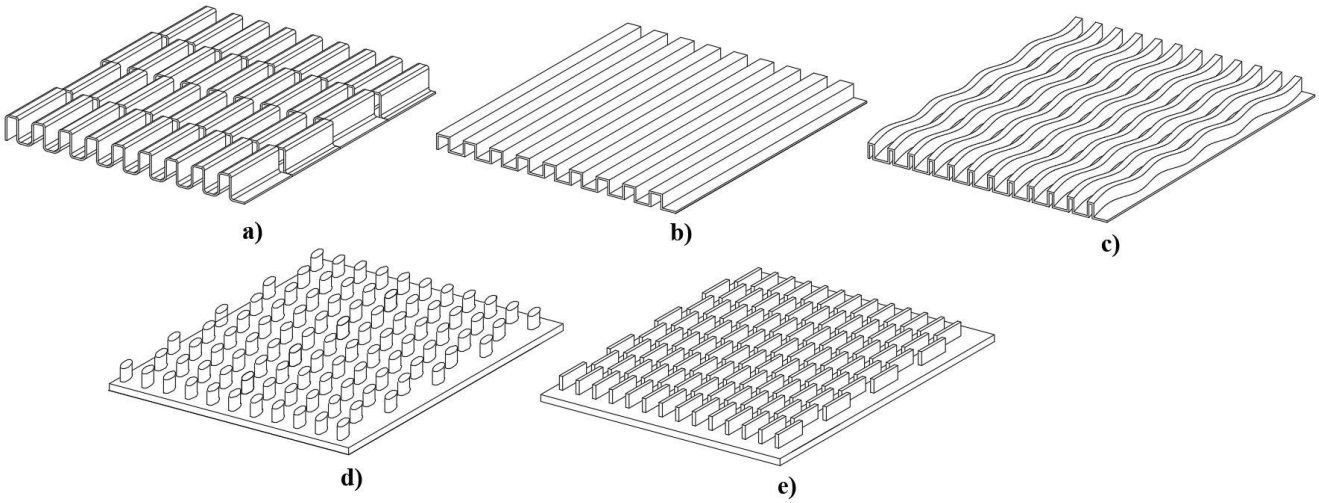

Figure 2: Examples Compact Heat Exchangers Cores as provided by Incropera and DeWitt [1]: (a) Flat Fin-Flat Tube, (b) Flat Fin-Circular Tube, (c) Circular Fin – Circular Tube, (d) Plate Fin Single Pass, (e) Plate Fin Multipass

Arrays of fins are typically machined or brazed into the flow path. An array of interrupted fins is used to both increase the surface area available for heat transfer and increase the convective heat transfer coefficient by interrupting thermal boundary layer formation. This greatly increases the thermal performance of a heat exchanger, but negatively affects hydraulic performance, resulting in higher pressure losses across the core [4].

Additionally, sizing constraints typically limit the maximum volume that a Cold Plate can occupy. This naturally leads to optimization of Cold Plate designs becoming necessary, where the goal is to increase the area available for heat transfer while minimizing volume and pressure losses. An optimized design will result in a balance between pressure loss, thermal performance, cost, manufacturability, and reliability.

1.2 Additive Manufacturing of Metals

Additive Manufacturing (AM) is the process of joining materials to make objects from 3D modeling data, usually in a layer by layer manner [3]. Although polymer additive manufacturing has become common and inexpensive even for hobbyists, AM of metals is still a relatively rare and expensive process, requiring expensive materials and ancillary machines such as furnaces, sifters, vacuums, and chillers to function.

Metal AM can be broken down into two main groups: Directed Energy Deposition (DED) and Powder Bed Fusion (PBF). DED involves fusing of metal powders with a focused high energy source while the metal powder is being deposited, similar to wire feed MIG welding. PBF is the process by which a thermal energy source selectively fuses material in a bed of powder along a specific scan path [6].

PBF can be further broken down by the type of thermal energy source used to fuse the metal powder. Powder Bed Fusion–Laser (PBF-L) denotes a machine utilizing a laser as the energy source, whereas Powder Bed Fusion–Electron Beam (PBF-EB) uses a beam of electrons to melt the metal powder. In both processes, the energy source fuses tracks of powder in a specific pattern to create the cross section of the 3D model. When a single layer is complete, the powder bed will

lower itself by some increment, and a new layer of powder is dosed out [6]. This process is shown in ***Figure 3***.

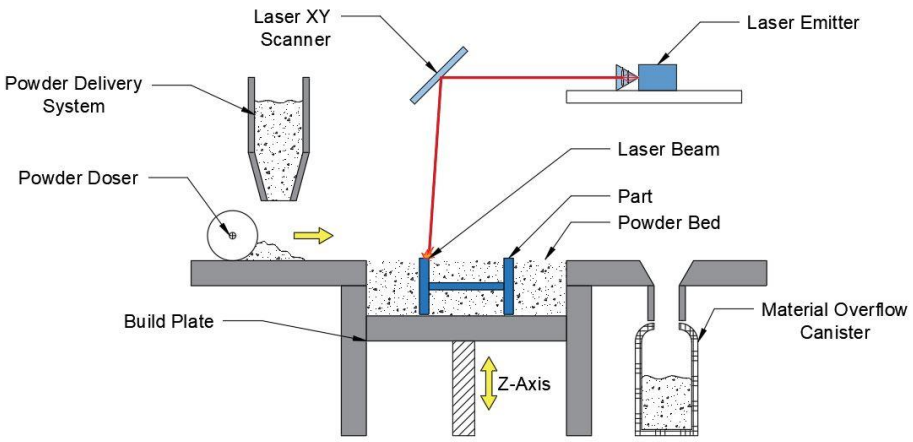

Figure 3: Functional Overview of PBF-L

The characteristics of a PBF-L part greatly depends on a number of factors including part orientation, part location on the build plate, laser scan speed, laser scan strategy, and laser power [6, 7]. Another influencer of part quality is the powder used during the printing process. The characteristics of the powder used, such as uniformity of shape and size, porosity, and foreign contaminants/inclusions, can affect the mechanical properties and surface characteristics [8]. Surface quality is of particular interest when designing parts for fluid experiments, where both thermal and hydraulic performance are greatly influenced by surface roughness.

The ability to rapidly prototype and produce optimized designs that were previously impossible to manufacture has become a tremendous asset within the design process. The ability of AM to combine multiple components into a single part helps to reduce the complexity of

assemblies, and streamlines the manufacturing process by reducing numbers of subassemblies or manufacturing steps required. Perhaps one of the most successful utilizations of Metal Additive is the fuel injection nozzle in GE Aviation's LEAP engine. Engineers were able to combine a total of 20 individual pieces into a single part which weighs 25% less and is 5 times more durable [9].

1.3 Literature Review

Significant research has been performed on the thermal and hydraulic performance of compact heat exchangers with varied fin types and arrangements. Most notable is "*Compact Heat Exchangers*" by Kays and London, which compiles performance data on a multitude of different heat exchanger types and arrangements [3]. The performance of lanced offset strip fin arrays, shown in ***Figure 4***, have been extensively investigated due to their ability to increase heat transfer performance through two mechanisms [3, 4, 10, 11]. First, by offsetting subsequent columns of fins, thermal boundary layers are forced to repeatedly redevelop. This maintains the high rates of heat transfer seen in developing flow throughout the heat exchanger [12]. Secondly, at higher flow rates vortices can be shed off the trailing edges of the fins, promoting flow mixing and increasing heat transfer rates [10].

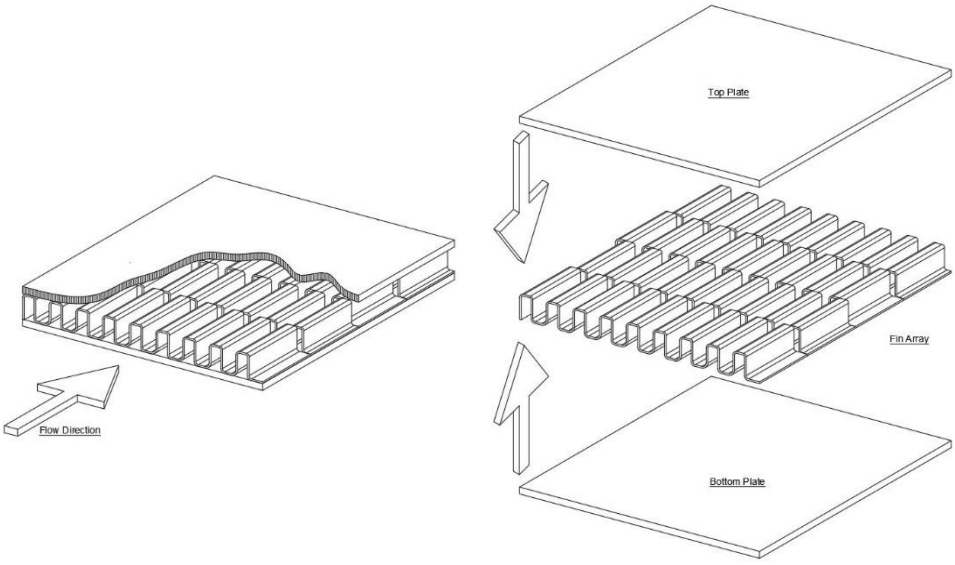

Figure 4: Lanced Offset Fin Array

Several experimental and numerical studies have developed correlations for the friction and thermal performance of lanced offset strip fins for laminar, turbulent, and transitioning flow [4, 11]. In the experimental study performed by Manglik and Bergles, correlations were developed based on the geometric characteristics of air flow through 18 different arrays of offset strip fins. Correlations for Fanning Friction factor and Colburn-j factor were developed for $120 < Re < 10^4$, and were found to be accurate within ±20% of experimental data [4].

Researchers aiming to take advantage of recent advances in additive manufacturing have investigated using AM to produce novel heat exchanger designs. Experiments performed by Wong et al [13], investigated the thermal hydraulic performance of rectangular, rounded rectangular, and elliptical strip fins produced via PBF-L. Researchers found the elliptical strip fin array provided the best balance between pressure loss and thermal performance. Notably, pressure losses were significantly reduced compared to rectangular fins by rounding off the leading and trailing edges.

In another experiment performed by Kuehndel et al [14], the effects of wavelength and amplitude of wavy fins, between 7.5-12 mm and 1-2mm respectively, were investigated in additively manufactured 316L Stainless Steel Heat Exchangers. Although the authors did not compare their results to the performance of traditionally manufactured wavy fins, good correlation was found between experimental pressure loss results and correlations developed by Aliabadi et al and Awad et al [15, 16]. However, significant deviation was seen between the correlations for Nusselt number and the experimental results, which the authors attributed to the high surface roughness in the AM fin array [15].

In a study performed by Saltzman et al [17], an aircraft heat exchanger using both air and water as working fluids was Additively Manufactured in AlSi10Mg from X-ray Computed Tomography (CT) data taken from a baseline traditionally manufactured heat exchangers. During experimentation, the AM Heat Exchanger saw a 10% increase in heat rejection over its traditionally manufactured counterpart; however, air side pressure loss was doubled. Again, the increases in thermal performances and pressure losses were attributed to the surface roughness characteristics of the additively manufactured Heat Exchanger.

Throughout the literature, the effects of surface roughness on thermal and hydraulic performance of AM heat exchangers was mentioned, but rarely was it thoroughly investigated [13, 14, 17]. In the experiment performed by Stimpson et al [18], the effects of surface roughness on thermal and hydraulic performance of additively manufactured mini-channels was investigated. The researchers found that as-built PBF-L test coupons had increased friction factors and Nusselt numbers when compared to the traditionally manufactured control groups. The increased heat transfer performance caused by the surface roughness did not scale linearly with increased friction

factors, and a decrease in heat transfer augmentation was seen with increasing Reynolds number. This suggests that the inherit roughness of additively manufactured parts may be a feature and not a bug, but any benefits seen will diminish with high higher flow rates.

The geometry of several additively manufactured Heat Exchangers found in literature is summarized below in ***Table 1***. From the table, fins usually have thicknesses above 300µm with a wide range of fin heights and lengths.

Table 1: Geometry of AM Heat Exchangers in Literature

Author	Fin Geometry	Material	Process	Machine	Fin Thickness/Diameter [µm]	Fin Height [mm]	Fin Length [mm]
Kuehndel et al.	Wavy channel	316L	PBF-L	M1 Concept	300.0	12.000	150
Wong et al.	Pin Fin	AL 6160	SLM	MCP Realizer II	2210.0	10.000	-
	Rectangular Strip				870.0	10.000	3.24
	Rnd. Rectangular Strip				870.0	10.000	3.72
	Ellitptical Strip				960.0	10.000	3.19
Stimpson et al.	Rectangular Channel	CoCr	DMLS	N/A	627.5	1.016	25.4
					718.4	2.032	
					786.1	0.660	
					1042.7	1.321	
					1042.7	0.610	
		Inconel 718			627.5	1.016	
					718.4	2.032	
					786.1	0.660	
					1042.7	1.321	
					1042.7	0.610	
Saltzman et al.	Lanced Offset & Louvered	Al10SiMg	PBL-L	EOSINT M280	330	N/A	N/A

1.4 Objective of Current Study

The objective of this study is to investigate the ability of PBF-L Metal AM to produce Compact Cold Plates for use in the cooling of electronics packages. A single-phase heat transfer experiment will be performed, and the experimental results will be compared against thermal-fluid simulations. Using this comparison, each of the novel Cold Plates designed will be ranked according to their respective thermal and hydraulic performance.

The Cold Plates were designed to fit specific criteria, as specified by the industry customer. The specimens are 2" in width and length with 0.100" high fluid channels. The fin array is bounded by 0.050" thick walls. The Cold Plates have a surface area per volume ratio greater than 48 in^2/in^3 (1890 m^2/m^3). Fluid is to enter the cold plate at 15°C and exit at 30°C with no more than 0.3 psid pressure drop per linear inch. The working fluid for the cold plate was originally intended to be Polyalphaolefin (PAO); however, this was later changed to a Water Ethylene Glycol (WEG) mixture for ease of procurement. ***Figure 5*** shows an initial concept for the finned array test coupon with Inlet and Outlet fittings.

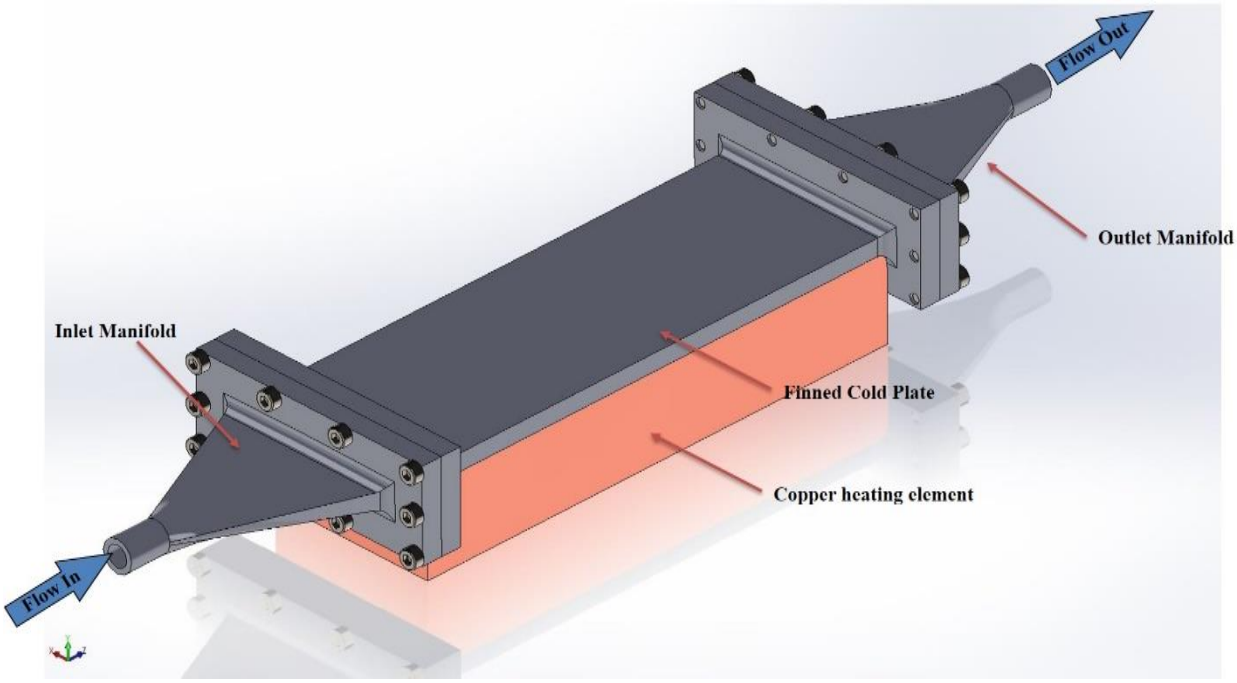

Figure 5: Initial Concept of Finned Test Coupon with Inlet/Outlet Fittings

Chapter 2: Design of Experiment

2.1 Initial Specimen Design

In order to determine the effects of the unique challenges associated with metal additive manufacturing on the fabrication of micro fin arrays, an initial exploratory print utilizing simple rectangular offset strip fin arrays was performed first. A total of 25 1”x1” test coupons were designed to test the effects of fin thickness and spacing on the quality of micro fin arrays. Test coupons were designed with 8 to 16 columns of fins in the streamwise direction and 24 rows of fins perpendicular to the flow direction, shown in **Figure 6**.

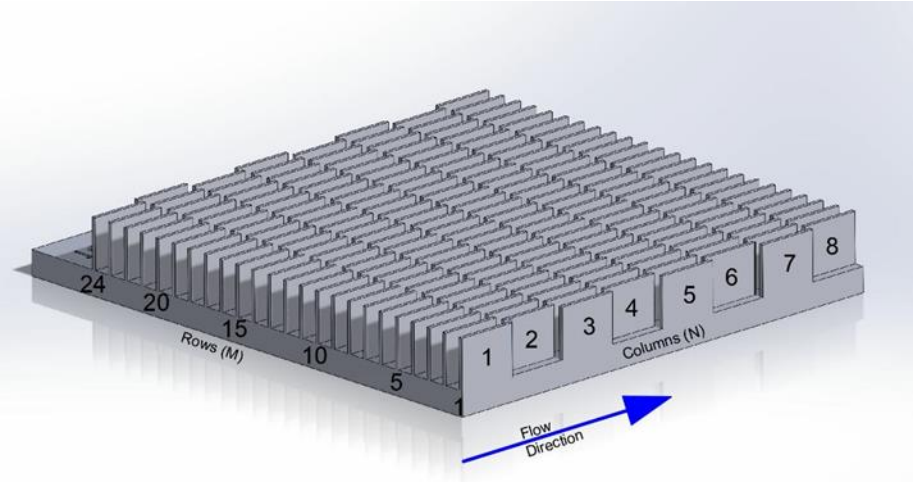

Figure 6: Test Coupon Layout and Nomenclature

Figure 7 defines the fin thickness, fin offset spacing, and fin length variables tested during the initial exploratory print.

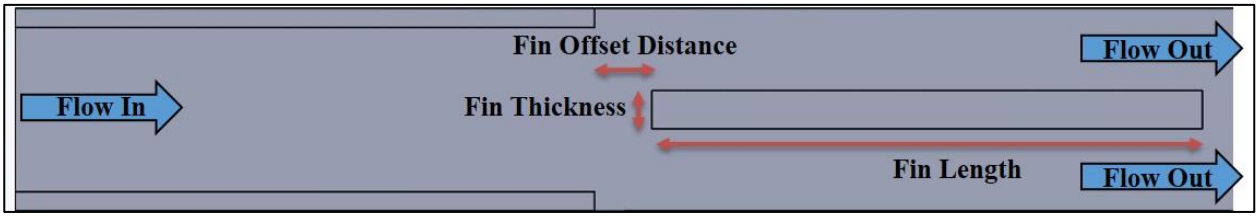

Figure 7: Definition of Major Fin Geometries

For Samples #1 – 12 in **Table 2**, fin thickness was held constant at either 200µm, 300µm, or 400µm and the streamwise offset was varied from 0µm to 300µm. Samples #13-23 had the same fin arrays as the previous 12 samples; however, a 0.050" thick enclosure was added around the fin array to mimic a sealed cold plate. This allowed for ease of powder removal from the fin arrays to be investigated. Specimen #24 and #25 had fin thicknesses of 200µm and 300µm, no streamwise offset, and doubled the number of fin columns from 8 to 16.

Table 2: Specimen Design Data

Sample Number	Fin thickness [µm]	Streamwise Offset [µm]	Number of Columns	Covered [Y/N]
1	200	0	8	N
2	300	0	8	N
3	400	0	8	N
4	200	100	8	N
5	300	100	8	N
6	400	100	8	N
7	200	200	8	N
8	300	200	8	N
9	400	200	8	N
10	200	300	8	N
11	300	300	8	N
12	400	300	8	N
13	200	0	8	Y
14	300	0	8	Y
15	200	100	8	Y
16	300	100	8	Y
17	400	100	8	Y
18	200	200	8	Y
19	300	200	8	Y
20	400	200	8	Y
21	200	300	8	Y
22	300	300	8	Y
23	400	300	8	Y
24	200	0	16	N
25	300	0	16	N

Figure 8 compares the effect of fin thickness on surface quality, comparing fins arrays with 200µm, 300µm, and 400µm thick fins. Visual inspection of all 25 specimens listed in **Table 2** showed a clear correlation between fin thickness and an observed decrease in surface quality, mainly due to an increased amount semi welded surface particles. The larger amount of semi welded particles sometimes resulted in the total blockage of the fluid channel between fins, as shown in **Figure 9**.

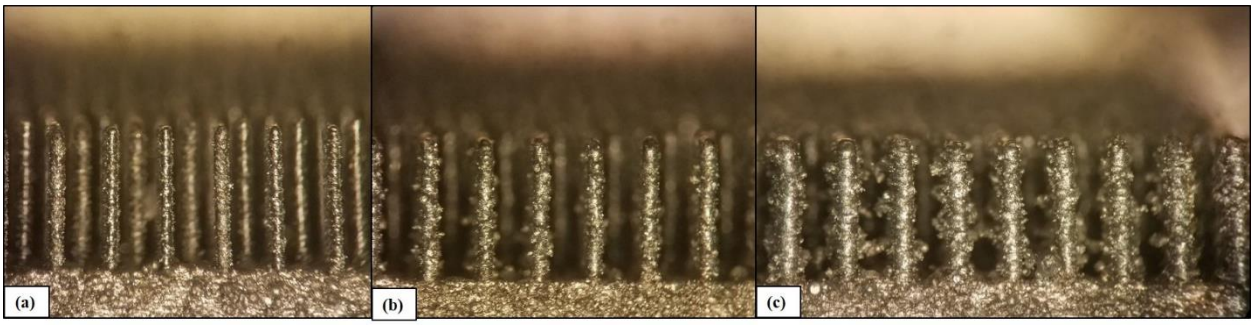

Figure 8: Comparison of Fin Thickness Effects on Surface Quality Front View (a) 200µm Thick Fins (b) 300µm Thick Fins (c) 400µm Thick Fins

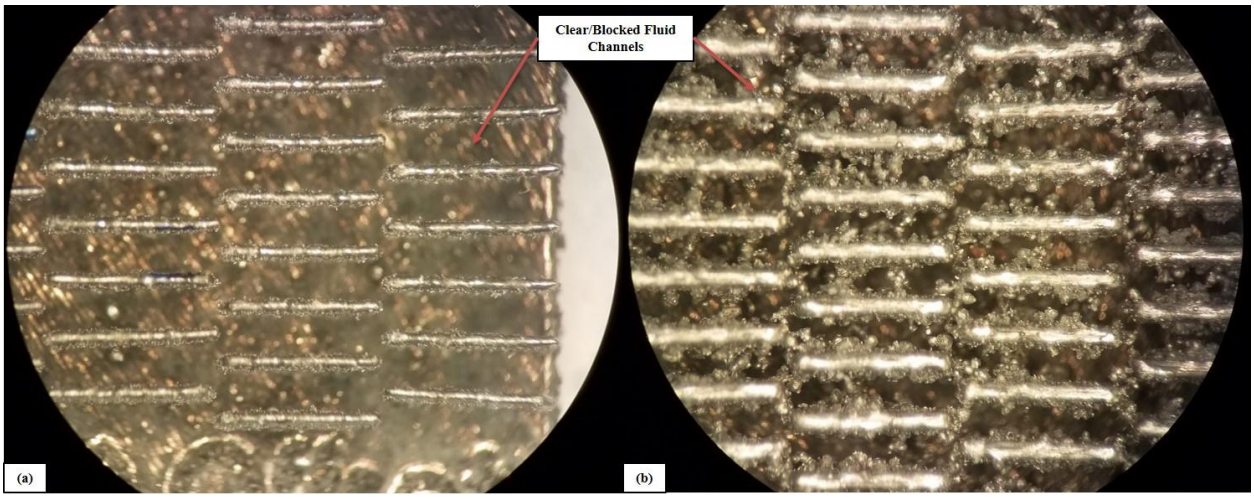

Figure 9: Comparison of 200µm and 400µm Fin Test Coupons Top View (a) 200µm Thick Fins (b) 400µm Thick

Figure 10 shows a top-down view comparing Sample #1 and Sample #11, with 0µm and 300µm spacing between fin columns, respectively. This increased spacing is intended to decrease pressure loss through a fin array by allowing a larger area for fluid flow between offset fin columns.

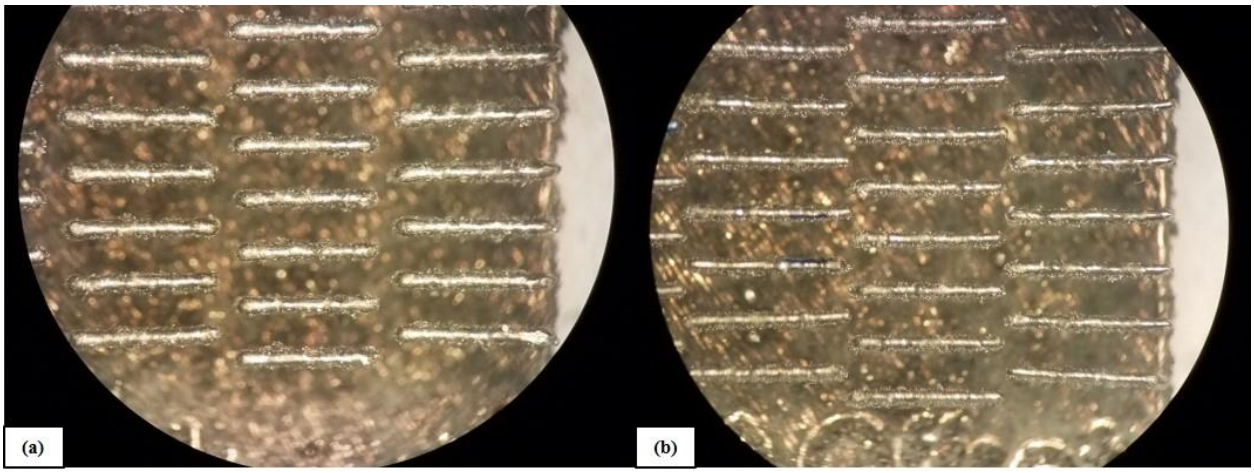

Figure 10: Comparison of Offset Spacing Top View (a) 300µm Spacing (b) 0µm Spacing

From this exploratory print, the decision was made to utilize fin arrays with the smallest fin thickness tested, 200µm, since these samples had the fewest number of semi-welded particles. An additional benefit of utilizing thinner fins is the lower pressure loss across the cold plate caused by form drag on the staggered columns of fins. The fin offset distance for novel fin arrays designs was varied from 0µm to 300µm. This resulted in a total of 4 novel fin array designs of rectangular offset strip fins.

2.2 Selection of Working Fluid

Within the initial Statement of Work (SOW), PAO was specified as the required working fluid; however, due to procurement issues, the working fluid was changed to a more readily

available WEG mixture. DOW Therm SR1 is a 95.5 weight percent concentrated solution of Ethylene Glycol, and was selected as the new working fluid [19]. The DOW Therm concentrate was diluted by 50% volume of deionized water, the properties of which are provided in **Table 3**.

Table 3: Saturation Properties of DOW Therm SR1 at 50% Ethylene Glycol Concentration by Volume [18]

Temperature		Specific Heat		Density		Thermal Conductivity		Viscosity	
°C	°F	kJ/(kgK)	Btu/(lb°F)	kg/m^3	lb/ft^3	W/(mK)	$Btu/(hrft^2)$	mPas	cPs
-30	-22	3.09	0.739	1090.3	68.07	0.333	0.1926	43.997	44.00
-20	-4	3.129	0.748	1088.15	67.93	0.3442	0.1989	22.0816	22.08
10	50	3.245	0.776	1078.72	67.34	0.3724	0.2152	5.5071	5.51
40	104	3.361	0.803	1064.91	66.48	0.3937	0.2275	2.2567	2.26
65	149	3.457	0.826	1050.05	65.55	0.4062	0.2347	1.2936	1.29
90	194	3.554	0.849	1032.15	64.44	0.4139	0.2391	0.8227	0.82
120	248	3.67	0.877	1006.66	62.84	0.4168	0.2408	0.5252	0.53

To convert from the required PAO flow rates given in the SOW to an equivalent flow rate of DOW Therm, the Reynolds number for flow through a pipe was matched for both fluids. A brief overview of these calculations is shown in equations (1)-(4), and detailed sample calculations are provided in **Appendix A**. This allowed for the calculation of mean velocity and, by extension, the volumetric flow rates needed when using DOW Therm. In the equations, ρ and μ represent the density and dynamic viscosity of the working fluid, u_m represents the mean fluid velocity, and D_h is the hydraulic diameter of the tubing.

$$\mathrm{Re} = \frac{\rho u_m D_h}{\mu} \tag{1}$$

$$Re_{PAO} = Re_{DOW} \tag{2}$$

$$Re_{PAO} = \frac{\rho u_m D_h}{\mu}\Big|_{DOW} \tag{3}$$

$$u_m = Re_{PAO} \frac{\mu}{\rho D_h}\Big|_{DOW} \tag{4}$$

2.4 Single –Phase Laminar Pressure Loss Analysis

The calculated channel Reynolds number for flow in the fin array was found to be between 15.3 and 51.1, which is well below the threshold of Re < 2300 for laminar flow conditions [1]. These calculations can be found in **Appendix A**. As was discussed in **Chapter 1.3**, numerous researchers have experimented with different types of heat exchanger cores to generate friction factor correlations using the hydraulic diameter of the flow channel as defined in equation (8). Once the Fanning friction factor is known for a set geometry, pressure loss across that core can be predicted from mean fluid properties and mean channel velocity via equation (5) [1].

$$\Delta P = 4 f_f \frac{L}{D_{h-channel}} \frac{\rho (u_{m-channel})^2}{2} \tag{5}$$

For fully developed internal laminar flow, the local Fanning friction factor is defined in equation (6) based on the local surface shear stress [12].

$$f_f = \frac{\tau_s}{\frac{\rho (u_{m-channel})^2}{2}} \tag{6}$$

However, the total pressure losses associated with a heat exchanger cannot be estimated based solely on the skin friction in the flow channels; several additional factors contribute to total pressure loss. Flow and pressure loss across a single channel of a heat exchanger core is visually represented in ***Figure 11*** [2].

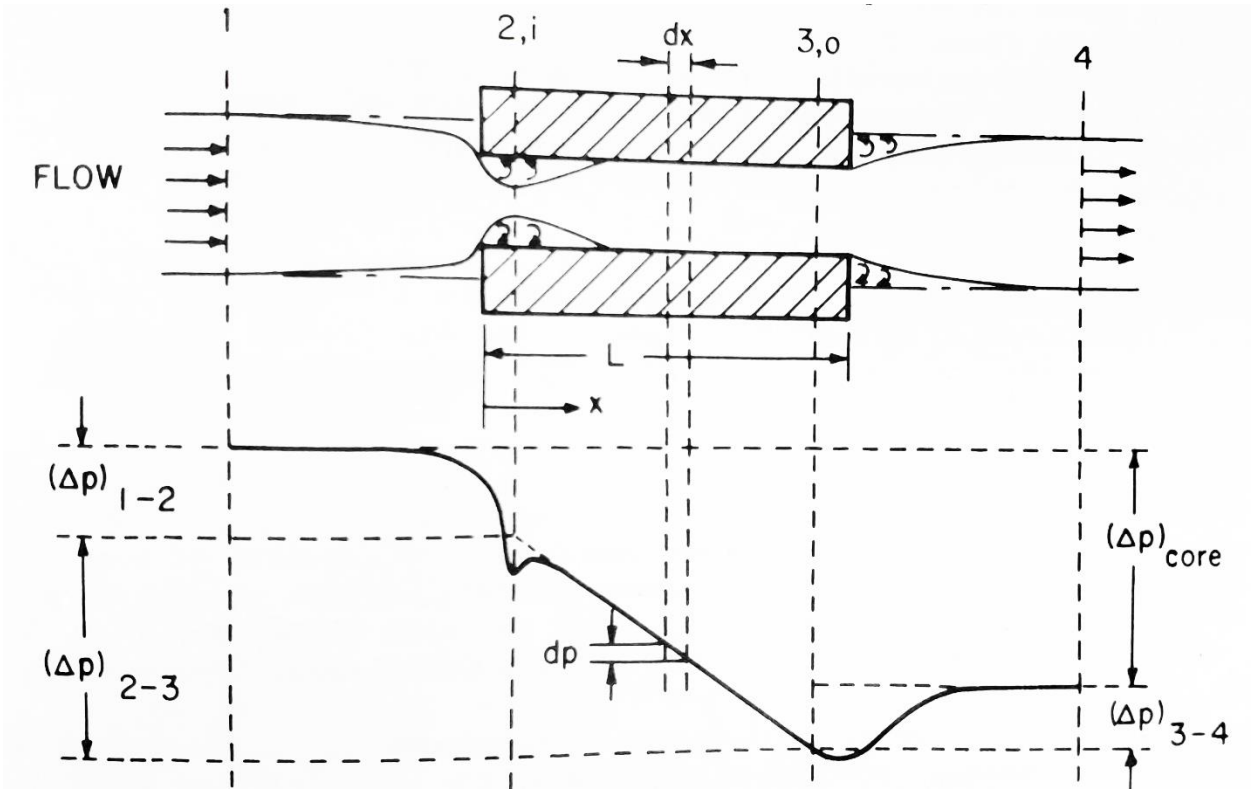

Figure 11: Pressure Drop Components Associated with One Passage of a Heat Exchanger [2]

Apparent Fanning friction factor can be used to account for the pressure losses caused by skin friction and the change in momentum rates caused by the changing velocity profiles and entrance/exit effects [2, 3, 5]. This is done by utilizing the total pressure loss between two points. If a heat exchanger core possess multiple channels in parallel, each channel will experience the same pressure loss across its length. As such the pressure loss across the heat exchanger core can be well represented by examining flow though a singles channel.

In ***Figure 11***, total pressure loss across the heat exchanger core was measured between points 1 and 4. In both Fluent simulations and experimental analysis, pressure loss was measured

between the inlet and outlet of the fin array to generate apparent Fanning friction factor curves for each studied cold plate geometry utilizing equation (7) below.

$$f_{app} = \frac{1}{4}\Delta P_{total}\left(\frac{D_{h-channel}}{L}\right)\left(\frac{2}{\rho(u_{m-channel})^2}\right) \tag{7}$$

In a 1995 journal paper published by Manglik and Bergles, correlations for Fanning friction and Colburn-j factors were developed based on the channel Reynolds number and dimensionless geometric properties of lanced offset strip fins for Laminar, Transitioning, and Turbulent flow [4]. ***Figure 12*** demonstrates the geometric and dimensionless parameters Manglik and Bergles considered to develop their correlations. In addition, Manglik and Bergles utilized a definition for hydraulic diameter based on fin thickness, height, and length shown in equation (8) below.

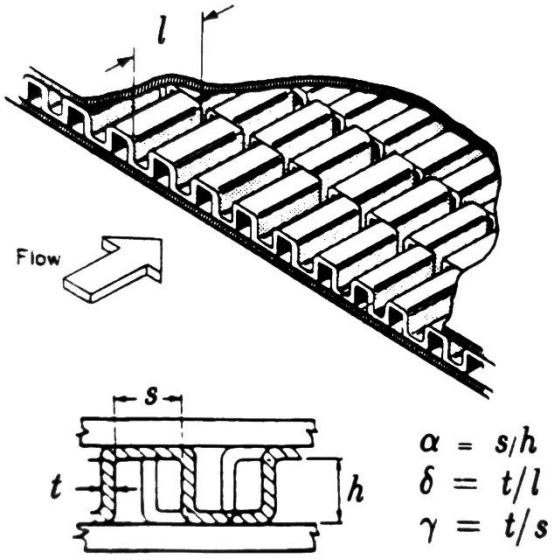

Figure 12: Geometrical Description of typical offset strip fin core [4]

$$D_{h-channel} = \frac{4shl}{2(sl + hl + th) + ts} \tag{8}$$

Using non-dimensional parameters α, β, and γ to describe the important geometric properties of each heat exchanger core, a multivariable regression analysis was performed to develop power-law expressions for Fanning friction factor and Colburn-j factor based on the channel Reynolds number, equation (9).

$$Re_{channel} = \frac{\rho u_{m-channel} D_{h-channel}}{\mu} \tag{9}$$

The correlation developed for Fanning friction factor, shown in equation (10), is valid for channel Reynolds numbers between $120 < Re < 10^4$ and is accurate with ±20% [4].

$$f_f = 9.6243(Re_{channel})^{-0.7422}\alpha^{-0.1856}\delta^{0.3053}\gamma^{-0.2659} * (1 + 7.669 \times 10^{-8}(Re_{channel})^{4.429}\alpha^{0.920}\delta^{3.767}\gamma^{0.236})^{0.1} \tag{10}$$

The correlations developed by Manglik and Bergles are accurate for channel Reynolds number ranges between 120 and 10^4; however, the channel Reynolds numbers for this experiment, calculated in **Appendix A**, are between 12.4 and 41.3, far outside of the accuracy range of the provided correlation. While this will result in higher relative difference between the numerical/experimental results and equation (10), it will be useful in validating the numerical simulation.

The proprietary correlations provided in the SOW for both Fanning friction factor and Colburn-j factor were used to provide a more accurate comparison against the numerical/experimental results. These correlations are accurate for a much lower Reynolds number range than equation (10) and were used to rate the hydraulic performance of each cold plate design against the provided geometry.

2.5 Heat Transfer Analysis

Classically, Colburn–j factor has been widely used to characterize the heat transfer performance of a heat exchanger by relating forced convective heat transfer to the Reynolds number [2-4, 10, 11]. In the definition of Colburn-j factor, provided in equation (11), Prandtl number raised to the 1/3 power was found acceptable for a moderate range of Prandtl numbers between 0.5 and 15 [3]. For fluids with higher Prandtl numbers, an exponent of 0.4 is more appropriate [4], where the average Nusselt number is the ratio of the convective to conductive heat transfer. This is shown equation (12).

$$j = \frac{\overline{Nu}}{Re_{channel} Pr^{0.4}} \tag{11}$$

$$\overline{Nu} = \frac{\bar{h}}{k_f D_{h-channel}} \tag{12}$$

The correlation developed by Manglik and Bergles for Colburn-j factor, shown in equation (13), is again valid for $120 < Re < 10^4$ and is accurate with ±20% [4]. However, air (Pr = 0.7) was used as the working fluid by Manglik and Bergles for the development of both equations (10) and (12). For the experiment performed herein, a Water Ethylene Glycol mixture ($Pr \approx 40$) was selected as the working fluid. With this experiment being outside the intended ranges of both the Reynolds and Prandtl number, equations (10) and (12) will yield significant disagreement between numerical and experimental results. As was discussed in the previous section, proprietary correlations provided a more accurate correlation to compare both Fanning friction factor and Colburn-j factor. Both equations (10) and (12) do however prove very useful in validating numerical model created in ANSYS Fluent as will be seen in **Chapter 3**.

$$j = 0.6522(Re_{channel})^{-0.5403}\alpha^{-0.1541}\delta^{0.1499}\gamma^{-0.0678}(1 + 5.269 \times 10^{-5}(Re_{channel})^{1.340}\alpha^{0.504}\delta^{0.456}\gamma^{1.055})^{0.1} \quad (13)$$

Another method for comparing fin arrays is to utilize the thermal resistance (Θ). The thermal resistance can be represented as the sum of the conductive, convective, and capacitive resistances between the cold plate and the fluid [20], where ΔT_{max} is the maximum difference in temperature between the fluid and the cold plate.

$$\Theta = \frac{\Delta T_{max}}{\dot{q_{in}}} = \frac{1}{k_{CP}L} + \frac{1}{\bar{h}A_s} + \frac{1}{\dot{m}c_p} \quad (14)$$

However, the conductive resistance can be minimized by minimizing the distance between the cold plate and the heat source [20]. This allows for the convective and capacitive resistances to dominate, and conductive resistance can be neglected [20]. Knight et al proposed multiplying equation (14) by the conductivity of the fluid and the width of the cold plate, k_f and W, respectively [21]. This generates a non-dimensional equation capable of scaling to any size cold plate [21], the result of which can be seen in equation (15), and is shown visually in ***Figure 13***.

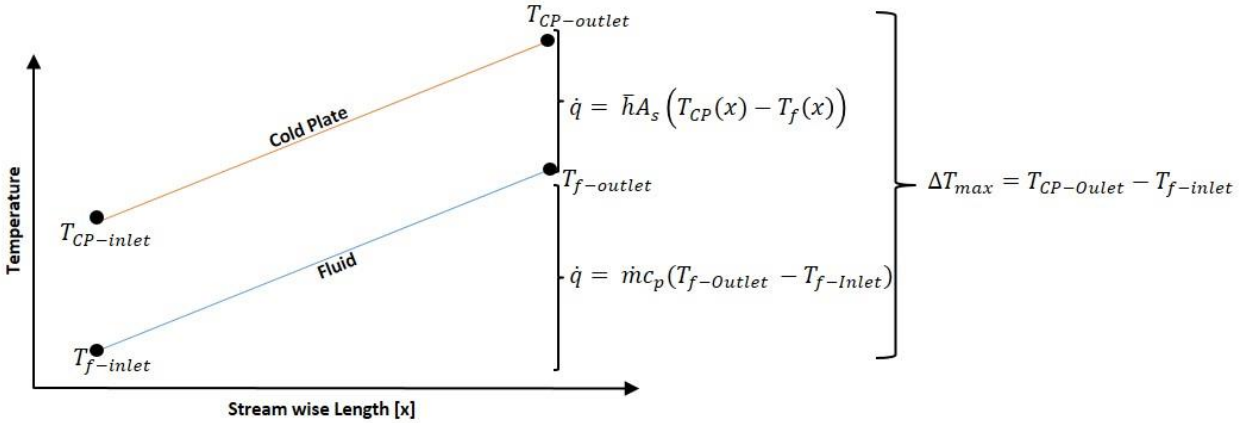

Figure 13: Streamwise Cold Plate Temperature Distribution with Constant Surface Heat Flux

$$\Theta = \frac{\Delta T_{max}}{\frac{\dot{q}_{in}}{k_f W}} = \frac{k_f W}{\bar{h} A_s} + \frac{k_f W}{\dot{m} c_p} \tag{15}$$

An advantage of utilizing dimensionless thermal resistance is its ability to directly account for the change in area available for heat transfer between fin array designs, something which Colburn-j factor does not do. Any increase or decrease in the mass flow rate a cold plate is capable of supporting at a specific pressure differential can be directly represented within the capacitive resistance term.

An additional benefit of utilizing dimensionless thermal resistance is the inclusion of the maximum temperature differential ΔT_{max} seen in the cold plate. When designing solutions for the cooling of electronics, it is often a requirement that the maximum temperature of the electronics package must not exceed a value specific by the manufacturer of the electronics package. The benefits and drawbacks of utilizing either Colburn-j factor or dimensionless thermal resistance to rank novel fin designs will be further discussed in **Chapter 5**.

2.6 Experimental Setup

The experimental setup was designed to collect pressure loss and temperature data for each printed cold plate. The setup was broken down into 3 subassemblies. The Test Coupon Assembly involves all of the components that directly interface with the cold plate, including the Inlet/Outlet Manifolds, heater block, and thermal insulation. The Flow Loop Assembly includes all of the components interacting with the working fluid: pumps, valves, reservoirs, and connectors. Finally,

the Instrumentation and Electrical Assembly consists of the instruments used to collected experimental data.

2.6.1 Conceptual Design of Test Coupon Assembly:

The Test coupon assembly went through several design iterations before the final configuration was selected. Three Principle Solution Variants (PSV) were developed with modifications made to address weak spots in the other designs [22]. Each of these variants, shown in ***Figure 14***, features detachable Inlet/Outlet manifolds to allow for multiple cold plate designs to be tested without the need to print multiple set of manifolds, saving both time and material.

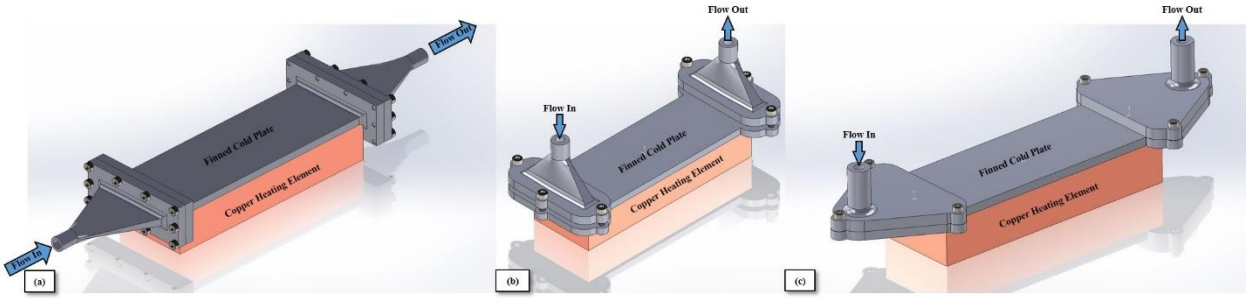

Figure 14: Principle Solution Variants of Cold Plate Assembly (a) PSV #1 (b) PSV#2 (c) PSV#3

The final conceptual design was selected by utilizing both absolute and relative criteria relating to the cost, manufacturability, and performance of each solution variant, with the greatest importance given to the verification of powder removal and uniformity of flow entering the cold plate. ***Table 4*** shows this decision matrix. PSV #1 rated the best in the selection criteria utilized and was selected for further development.

Table 4: Principle Solution Variant Decision Matrix

	Evaluation Criteria	Weight	PSV #1	PSV #2	PSV #3
Cost	Manifold volume of Powder [in^3]	5%	2.08	2.76	2.54
	Additional length added to cold plate [in]	10%	0.5	4.493	1.875
	Additional height added to cold plate [in]	5%	1	0	0
Manufacturability	Number of Machining post processes required (Cold Plate)	5%	3	3	3
	Number of part vice resettling (Cold Plate)	10%	6	3	3
	Number of special tools required	3%	0	0	0
Performance	Installation time [min]	2%	2	1	1
	Ease of powder removal	15%	1	2	2
	Verification of powder removal	20%	1	2	3
	Uniformity of Flow	25%	1	3	1
			1.59	2.51	1.93

PSV #1 rated the best in the selection criteria by its reduction in required powder volume and the ease of and verification of powder removal. This design was selected for further development.

2.6.2 Design of Inlet/Outlet Manifold

Both the Inlet and Outlet manifolds were designed to specifically account for all the benefits and design considerations of Metal Additive Manufacturing. As such, the need for post fabrication machining influenced the manifold design.

Both manifolds attach to the rest of the flow loop utilizing 0.250” compression fittings on a protruding stem. With the tolerances needed for compression fitting to work properly unachievable due to the inherent surface roughness of AM, the manifolds were designed with large

flat mounting surfaces. These mounting surfaces allow for the use of a machine vice for milling or 4-jaw lathe chuck for turning.

The port for the pressure transducer was slightly undersized for the letter X drill bit used to pre drill for ¼-18 NPT threads in order to account for the stair stepping effect seen in all AM processes, in accordance with the practical AM design considerations in Kranz et al [7]. Additionally, chamfers were added to the rear surface to reduce weight and material used. The final design of the manifolds can be seen in **Figure 15**.

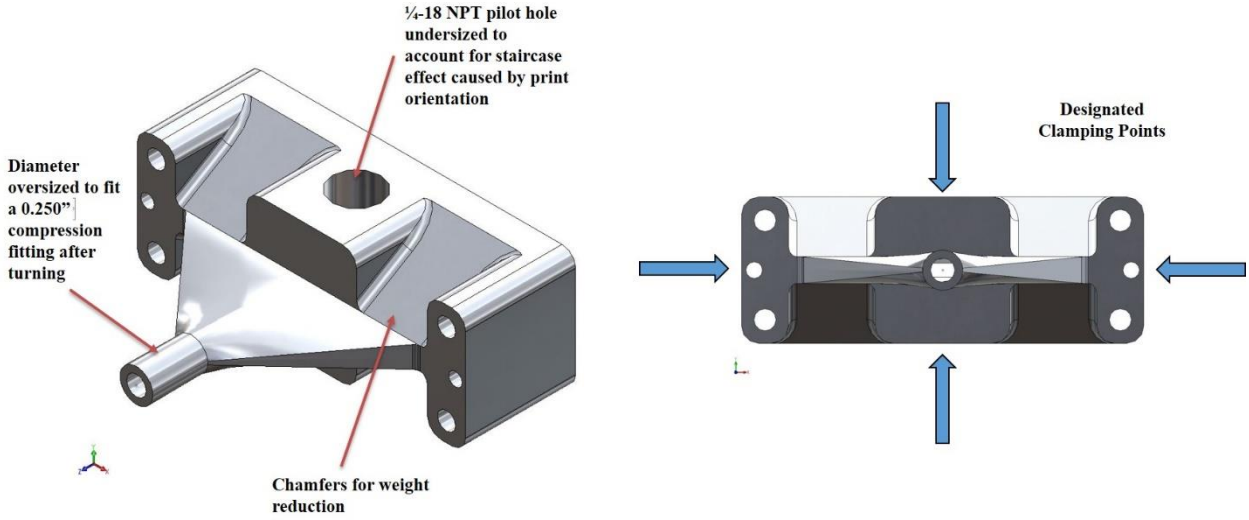

Figure 15: Design of Inlet/Outlet Manifold

To create a watertight seal between the manifolds and the cold plate, a No.31 square O-ring was selected; however, the as-built surface roughness in the printed O-ring grove did not allow for a good seal, causing a leak. From the Parker O-Ring Handbook, the minimum surface finish needed to achieve a seal for liquids is 32 µin [23]. White light interferometry was used to measure the actual surface roughness of the as printed and post machined manifolds at 4 equidistant

locations around the O-ring groove. ***Figure 16*** shows the specific measurement locations labeled as the I-IV Measurement locations, analogous to the hand positions on a clock.

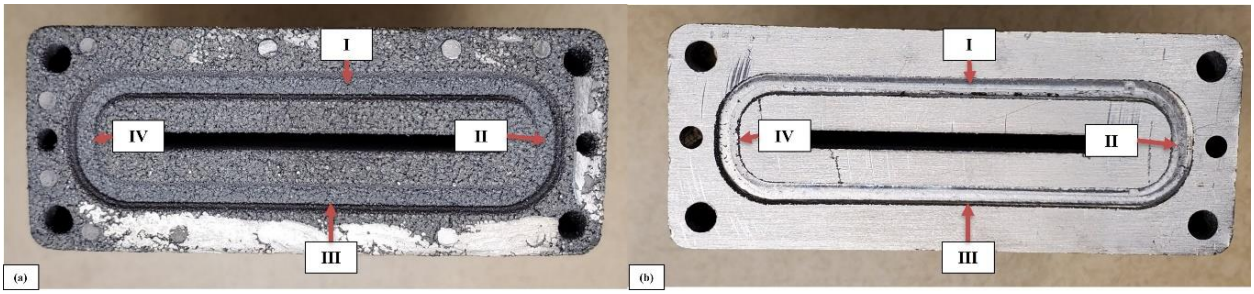

Figure 16: White Light Interferometry Measurement Locations

The results of these surface roughness measurements are shown in ***Figure 17*** where the surface roughness is shown as a colored plot with valleys shaded in blue and peaks shaded in red. From the measurements taken on the bottom surface of the O-ring groove for both manifolds, the as-built surface roughness averaged 2532 µin while the machined surface was only 30.2 µin. To meet surface roughness criteria for O-ring sealing post-processing of as-build surfaces will need to be considered for practical applications.

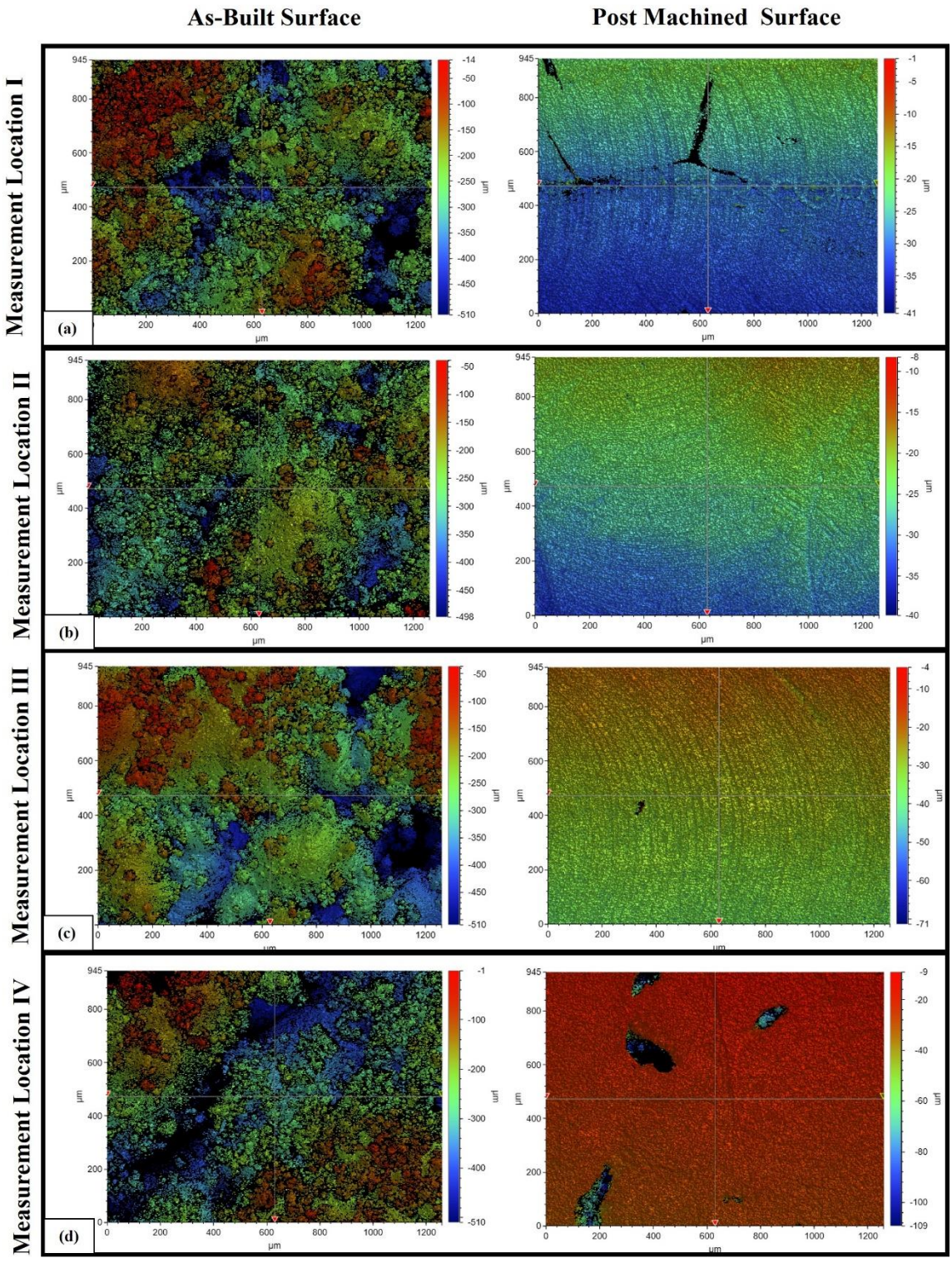

Figure 17: Surface Roughness's of As-Built vs. Machined AM Manifolds (a) Measurement Location I (b) Measurement Location II (c) Measurement Location III (d) Measurement Location IV

A characteristic of compact heat exchangers is the large frontal flow area presented to the flow manifold [3]. In a simple manifold design this results in uneven flow distribution, causing a decrease in pressure loss and heat transfer performance. Within the design of this experiment, iterative improvements were performed on the Inlet Manifold specifically to produce a uniform flow distribution at the exit of the manifold.

Each manifold design, as well as the first column of fins, was modeled in Solidworks and imported into ANSYS Fluent. Using Design Modeler, the internal volume of the manifold was isolated. All other geometry was suppressed, and the Computation Domain was halved to reduce the total number of elements needed. Flow into the manifold was set using a constant Inlet Velocity Boundary Condition (BC), and outlets were set at the end of each channel, as shown in **Figure 18**. The mean fluid velocity within the first column of fins was found via CFD Post and was used to calculate the amount of flow through each channel.

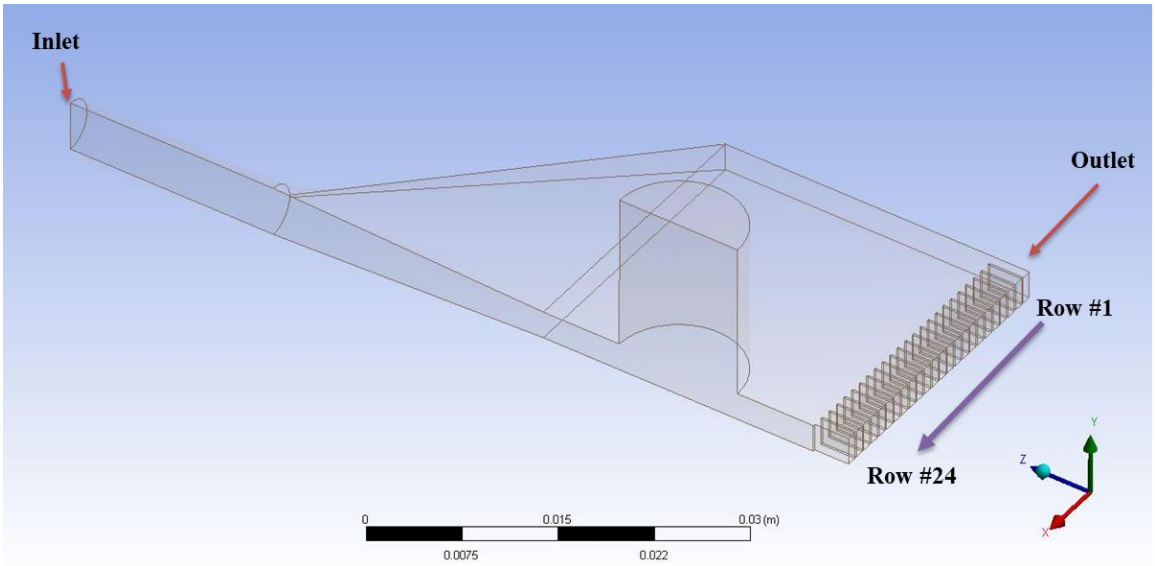

Figure 18: Model of Fluid within Inlet Manifold V1

The current distribution of flow is best visualized by a velocity vector plot produced by ANSYS in **Figure 19**, where the jet of higher velocity fluid entering the center of the fin array can be clearly seen.

To disrupt the flow entering from the tubing, a single large cylinder was added immediately following the inlet, and a line of smaller diameter cylinders was added further downstream. Labeled as Inlet Manifold V2, the velocity field and distribution of flow is shown in ***Figure 20***. Each Manifold design was simulated at the minimum and maximum flow rates to be used in the experiment, referred to as "High Flow" and "Low Flow" respectively.

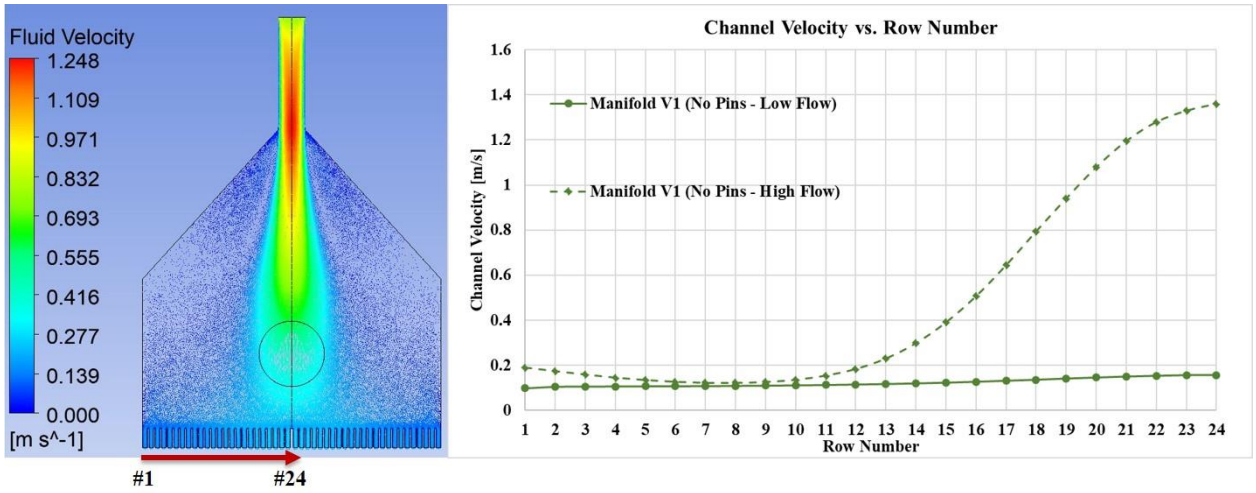

Figure 19: Distribution of Flow in Inlet Manifold V1

From the figure, it can be seen that although there is no longer a very intense fluid jet entering the middle of the fin array, two less intense jets of fluid separated from the 1st column and continued through the 2nd line of columns and into the fin array. This produced slightly higher fluid velocities in Rows 7 through 18; however, these velocity spikes are much lower than when no columns were present.

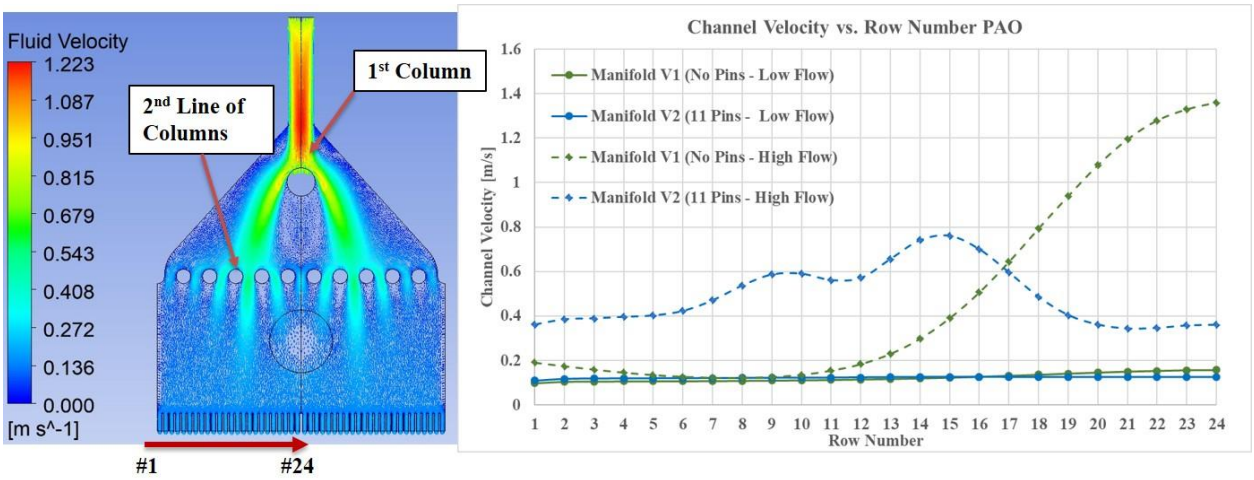

Figure 20: Distribution of Flow in Inlet Manifold V2

To further uniformly distribute the flow, two additional columns were added between the primary column and secondary line of columns. These columns were placed to interrupt the higher velocity wake separated off the first column and direct flow outwards toward the boundaries of the manifold. A comparison of Manifold designs V1, V2, and V3 is shown ***Figure 21***.

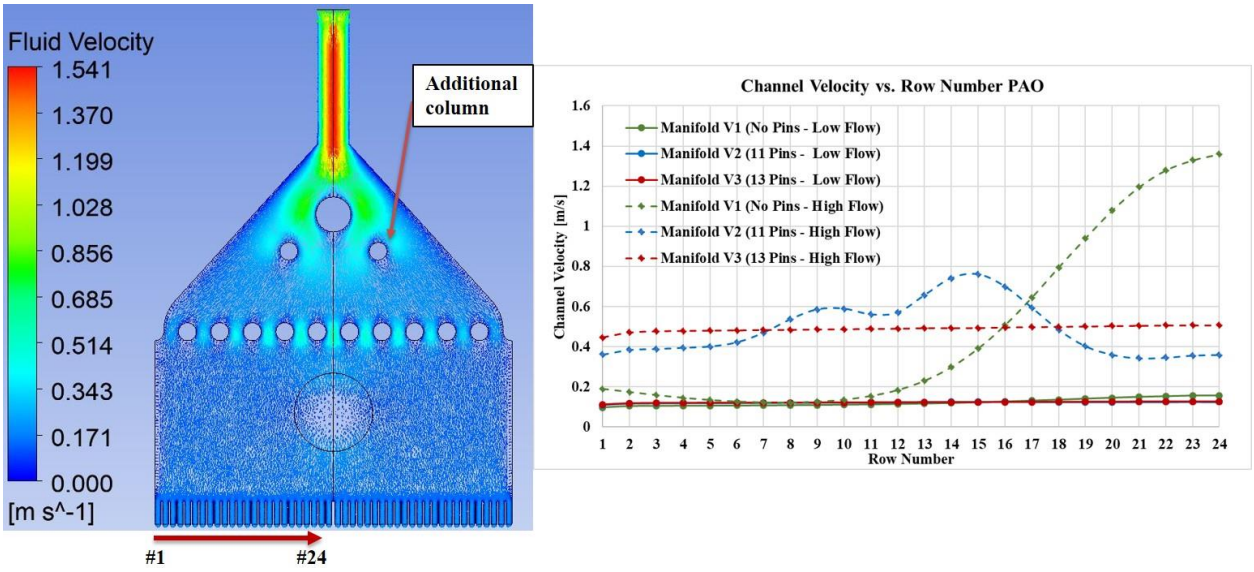

Figure 21: Distribution of Flow in Inlet Manifold V3

These additional columns were successful in creating a more uniform velocity distribution in each row. This improvement is quantified by calculating the Range, Mean, and Standard Deviation of fluid velocity in each fin channel; this data is displayed in **Table 5**.

Table 5: Results from Manifold Simulations

	Low Flow			High Flow [m/s]		
Manifold Version	Range [m/s]	Mean [m/s]	Standard Deviation [m/s]	Range [m/s]	Mean [m/s]	Standard Deviation [m/s]
V1	0.0590	0.123	0.0183	1.238	0.492	0.4459
V2	0.0171	0.123	0.0038	0.418	0.491	0.1313
V3	0.0152	0.123	0.0034	0.061	0.490	0.0135

As a result the changes made to the manifold design, Manifold V3 demonstrated the ability to produce a uniform velocity distribution at the manifold exit for a range of flow rates. This manifold version had the lowest deviation in the amount of flow through each channel, +/- 0.0135 m/s at the High flow rate.

2.6. 3 Final Design of Test Coupon Assembly:

Figure 22 shows an exploded view of the final layout of the test coupon assembly. In this assembly, the working fluid passes through the Inlet manifold, where it is redistributed before entering the cold plate. Next, the copper heating element supplies a heat flux on the bottom surface, increasing the fluid temperature before the fluid leaves the cold plate. The fluid then returns to the Flow Loop Assembly.

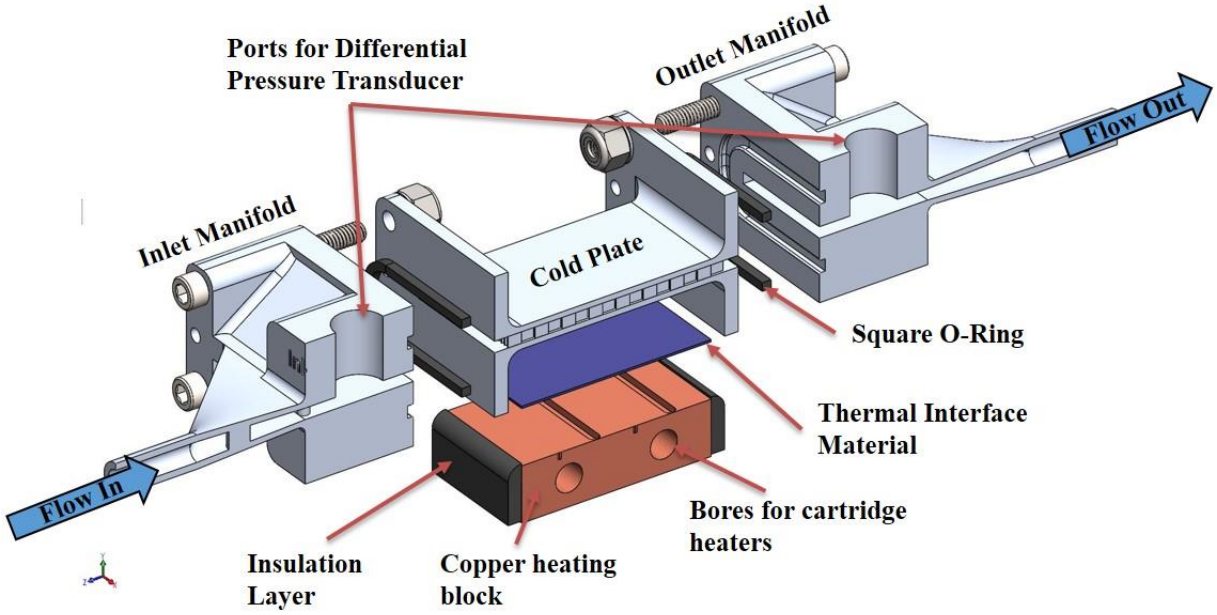

Figure 22: Final Cold Plate Assembly

To provide a constant heat flux into the cold plate, a copper block was machined to allow for the insertion of two 250W cartridge heaters, whose power was controlled by a variable autotransformer. Delrin strips, 1/8" thick, were used to insulate the interface between each manifold and the copper heater. A thermal pad was used at the interface between the cold plate and the copper heater to reduce contact resistance. Thermal pads were selected as the Thermal Interface Material (TIM) as they can be applied more consistently than thermal grease between experiments. The temperature of the copper block was recorded using four K-Type thermocouples evenly spaced on its surface.

2.6.4 Flow Loop Assembly:

The path the working fluid takes in the experimental setup is shown in **Figure 24** utilizing common P&ID symbols shown in [24]. The flow loop was designed to operate with either a Levitronix BPS-iF100 Magnetic centrifugal pump or and RC022 Chiller system with positive displacement pump from Boyd Corp [25, 26].

Symbols					
5, 19, 20		Needle Metering Valve	14		Working Line exiting above fluid level
4		Union Cross			
7,9,11,13		Union Tee	16, 18, 0		Drain exiting below fluid level
12, 15, 0		Plug Valve			
2		3-Way T-Port Valve	13		Vented Reservoir
22		Straight Adaptor			
		Reducing Adaptor	8	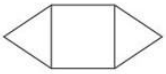	Cold Plate & Manifolds
10		Pressure Gage			
6	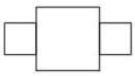	Flomec Flow Sensor	21		Vacuum Pump
10	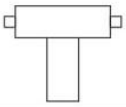	Differential Pressure Transducer			
	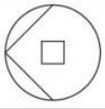	Positive Displacement Pump/Chiller	1	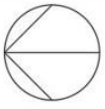	Centrifugal Pump

Figure 23: Common P&ID Symbols Used in Experimental Set-Up

A bypass loop was added before the first metering valve to allow for some portion of the working fluid to be siphoned off before entering the main flow loop. This allows for the volumetric flow rate of fluid entering the main loop to be precisely controlled. The volumetric flow rate through the main loop was recorded utilizing a Flomec OM008 oval gear flow meter. A photo of the as-built flow loop assembly is shown in ***Figure 25***.

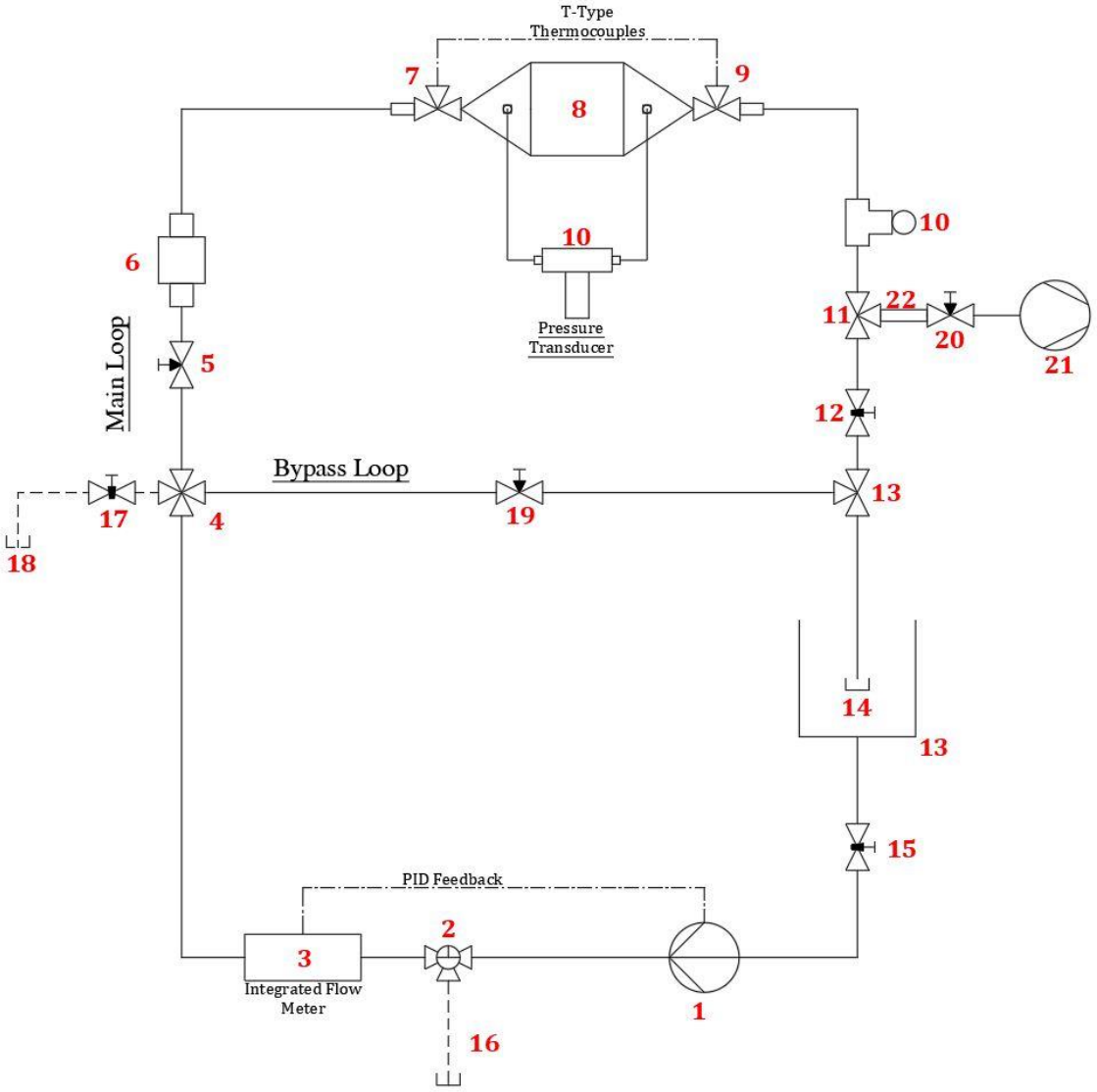

Figure 24: Experimental Setup Flow Loop

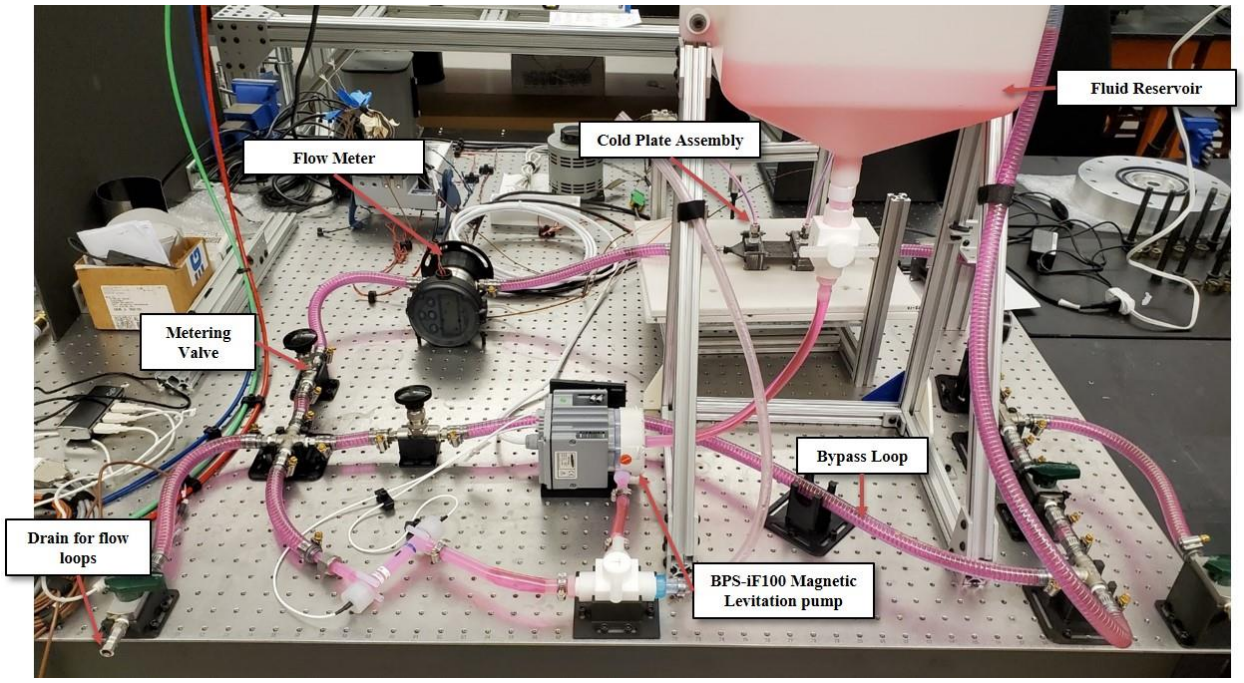

Figure 25: As-Built Experimental Setup

This flow loop assembly was designed to work a wide variety of both working fluids and pump with minimal changes to the layout. Additionally, custom mounting brackets were printed from Polyethylene Terephthalate Glycol (PETG) for easier routing of the tubing used.

2.6.5 Instrumentation and Electrical Assembly:

A PX409 0-10 inH_20 Differential pressure transducer from Omega was selected to measure the pressure loss across the cold plate at the locations shown in ***Figure 22*** and **Figure 24**. The temperature of the fluid was recorded utilizing two T-Type thermocouples located at the Inlet and Outlet manifolds. The data from all sensors was collected utilizing a National Instruments Data

Acquisition System (DAQ) and LabVIEW. **Figure 26** shows the electrical schematic of the experimental setup.

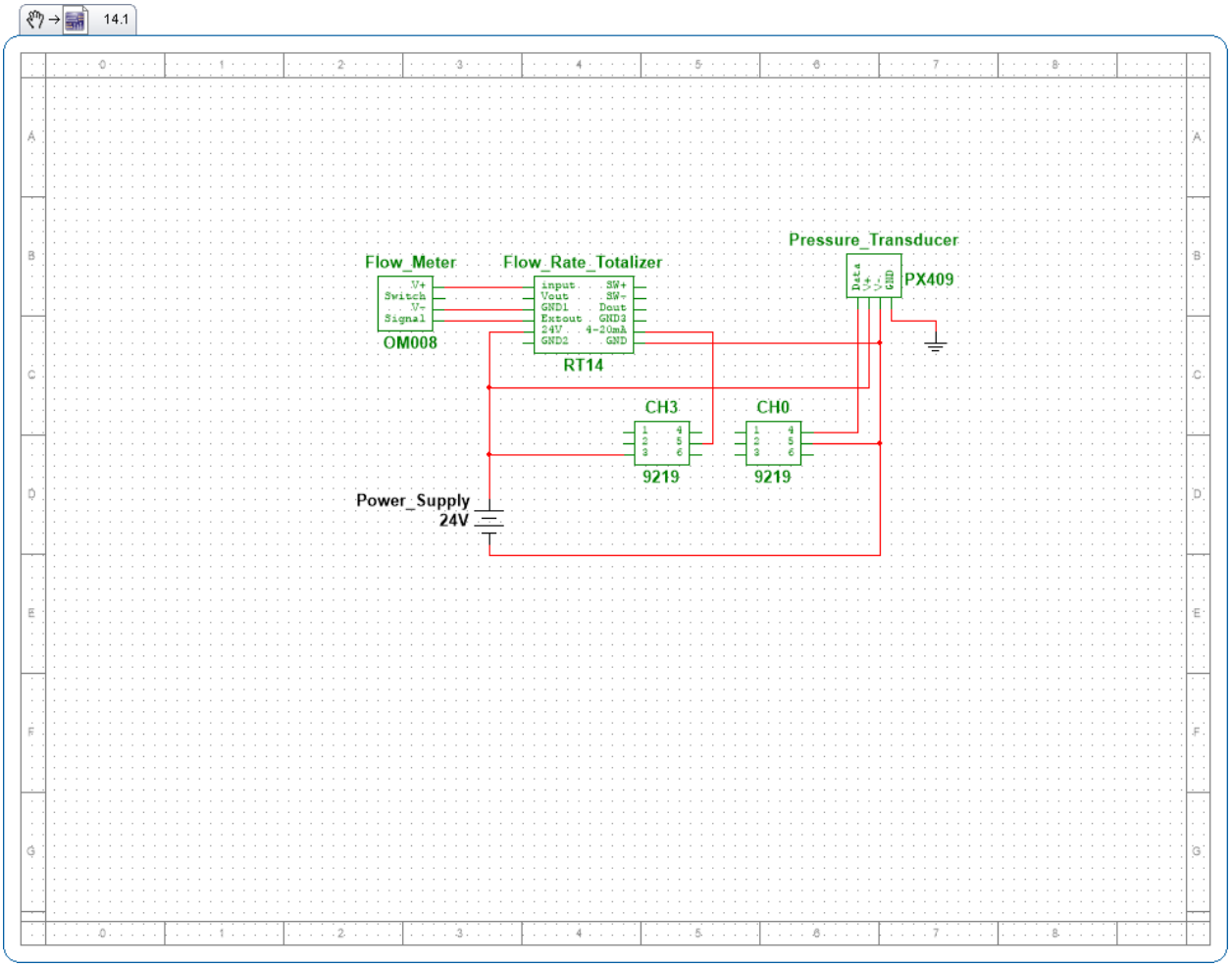

Figure 26: Electrical Wire Diagram of Experimental Set-Up Created in NI Multisim

Chapter 3: CFD Simulations

3.1 Geometries

The numerical thermal and pressure loss analysis for flow through each for each of the novel cold plates designed was performed utilizing two versions of ANSYS Fluent, Version 18.1 and 2020 R1. Using the repeating pattern of fins present in each novel cold plate design, lines of symmetry were utilized when possible to reduce the size of the computation domain needed for simulation. A model of this symmetric section of the fin array was created using SolidWorks, and was imported into ANSYS Design Modeler, where an enclosure volume was used to create the fluid in the array. **Figure 27** shows the CAD models generated in (a) SolidWorks and (b) ANSYS Design Modeler with the enclosure volume.

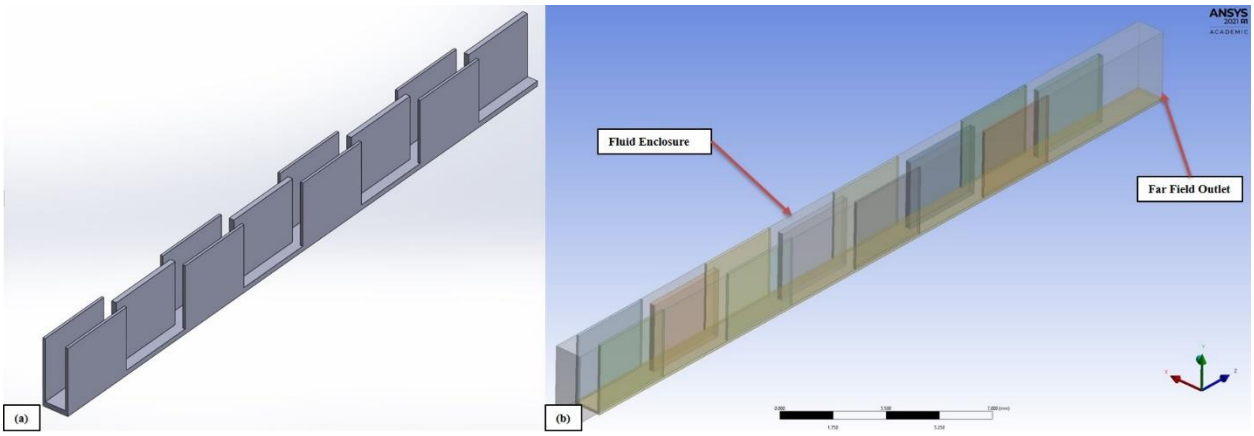

Figure 27: Model of computation Domain (a) SolidWorks Model of Symmetric Fin Array (b) Fluent Model with Enclosure

3.2 Meshing

Tetrahedral elements were utilized to represent the working fluid as they provided higher mesh quality for the sudden expansions and contractions seen between subsequent columns of fins as can be seen in **Figure 28**. Inflation layers were added to the wall boundary conditions, allowing the use of a very fine mesh to capture the effects of developing thermal and hydraulic boundary layers while maintaining a relatively coarse mesh in the free stream. The thickness and refinement of these inflation layers was considered when determining mesh independence. The leading and trailing edges of each fin were further refined to capture the important effects seen in developing thermal and hydraulic boundary layers, such as an increased convective heat transfer coefficient.

The rectangular geometry of both the fins and the fin base allowed for the use of a regular quad dominant meshing scheme. Since refinement of this mesh had little effect on simulation results, this mesh was kept coarse to reduce total number of elements in the computational domain.

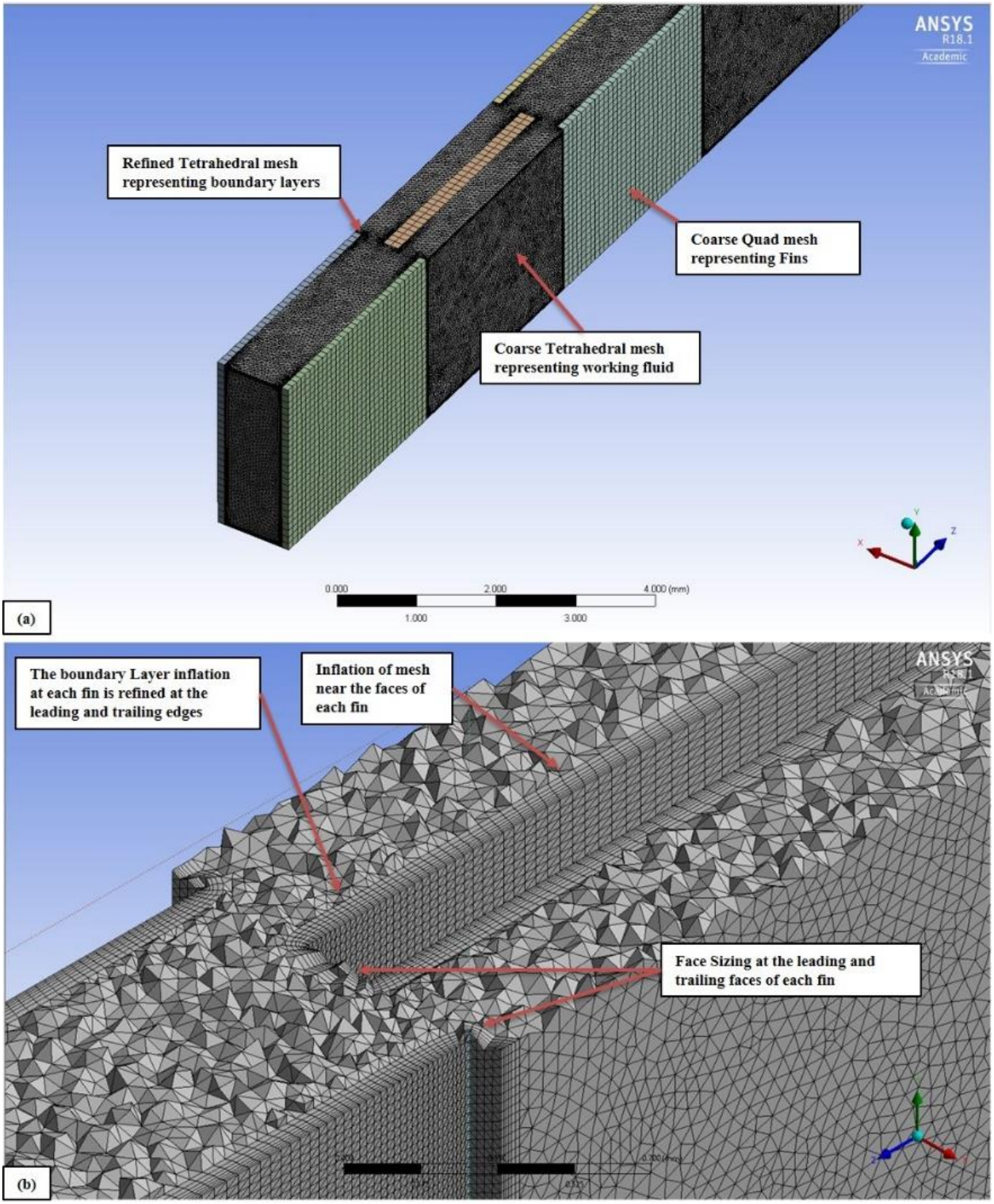

Figure 28: Meshing of Computation Domain. (a) Meshing of Fluid and Fins (b) Mesh Refinements of Boundary Layers and Developing Areas

3.3 Simulation Setup

Within the Fluent Solver, a constant inlet velocity was set at the Inlet to the fin array. No-slip boundary conditions were applied to the fluid-solid interfaces and to the top and bottom surfaces of the fluid. Due to the repeating design of the fin array, symmetric boundary conditions could be used on the left and right sides of the computational domain. Heat was provided to the array by a constant heat flux boundary condition on the bottom of the fin array. As is shown by the calculations in **Appendix A**, the channel Reynolds number is well within the laminar flow regimes. Therefore, a viscous laminar model was used. **Figure 29** shows the boundary conditions used for the simulation.

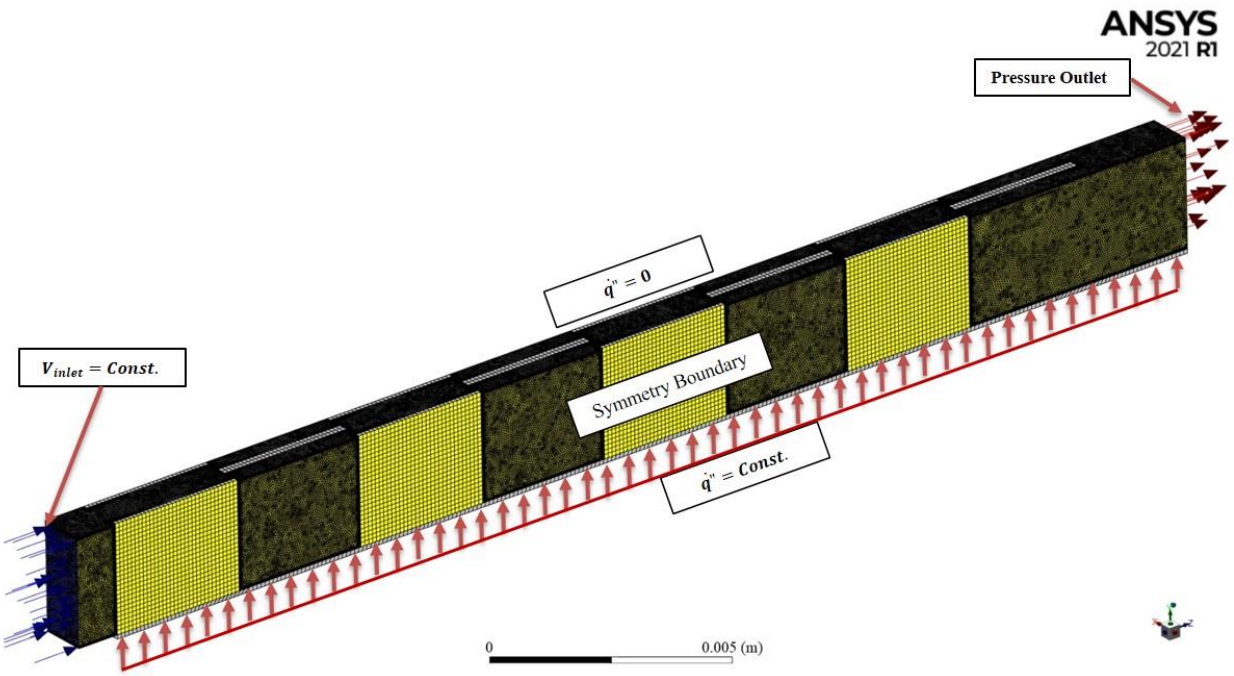

Figure 29: Computational Domain Boundary Conditions

Originally, the Power Law scheme was used as the discretization method for the Momentum and Energy solvers. However, when Fluent was upgraded from ANYS 18.1 to 2020R1, the Power Law scheme was removed as an option. As such, the 3rd Order Monotone Upstream-Centered Scheme for Conservation Laws (MUSCL scheme), which is a hybrid of the 2nd Central Differencing Scheme (Φ_{f-CD}) and 2nd Order Upwind Scheme (Φ_{f-SOU}), was used. This scheme was noted to work well with tetrahedral based meshes and provides at least 2nd Order accuracy [27]. The 3rd Order MUSCL scheme is provided below in equation (16), where θ is a weighting factor selected by ANSYS. The magnitude of θ determines whether the Central Differencing Scheme or Upwind Differencing Scheme is more dominant.

$$\Phi_f = \theta\Phi_{f-CD} + (1-\theta)\Phi_{f-SOU} \tag{16}$$

Piecewise linear interpolation of the saturated properties of DOW Therm SR1 was utilized in ANSYS to set the temperature dependence of ρ, μ, k, and c_p. Linear fits were deemed acceptable; the relative difference between linear and more complicated non-linear interpolation methods was found to be <1% for the temperature region over which the simulation takes place.

3.4 Simulation Post Processing

CFD Post was utilized to process the results of each simulation. Pressure loss across the fin array was calculated by taking the difference in the area averaged pressure at the inlet and outlet of the fin array. The pressure loss was saved as an output parameter in Fluent and was used to calculate the Apparent Fanning Friction factor for each fin design using equation (7).

With the constant heat flux applied to the array base, the mean temperature of the fluid will increase linearly in the flow direction [12] . Additionally, when the flow becomes fully developed, the temperature of the fins will increase at the same rate as the fluid, and the average convective heat transfer coefficient is invariant in the flow direction. When the mixed mean temperature of the working fluid, maximum, and average fin temperatures were plotted as a function of the streamwise distance, the temperatures in the simulated fin array were found to vary linearly as seen in **Figure 30**.

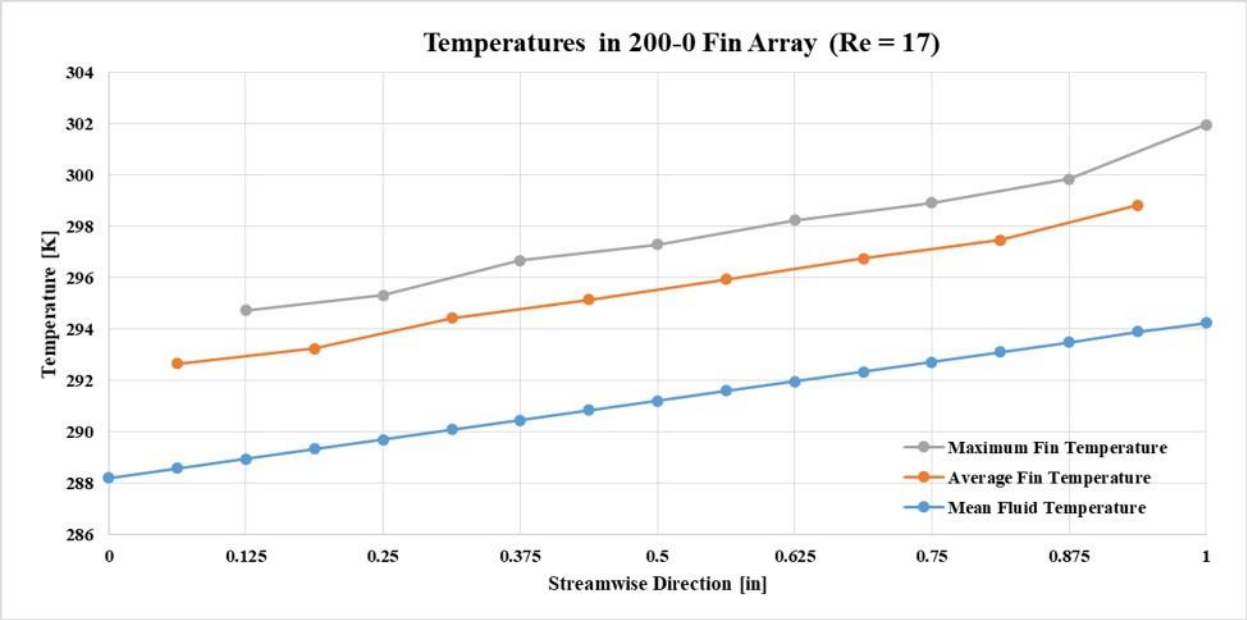

Figure 30: Temperature Distribution in 200µm-0µm fin array at Re = 17

To find a local heat transfer coefficient, the heat into the fluid must first be known by calculating the change in enthalpy of the fluid, with fluid properties being taken at the mean fluid temperature, equation (17).

$$\dot{q} = \dot{m}_f c_p (\mathrm{T}_{\mathrm{fluid-Outlet}} - T_{fluid-Inlet}) \quad (17)$$

The heat into the fluid was then divided by product of the total surface area available for heat transfer and the difference between the mixed-mean fluid temperature and the maximum fin temperatures, where the mixed mean fluid temperature represents the average thermal energy state of the working fluid at a particular cross section of the streamwise direction [12]. To determine the total surface area available for heat transfer, the sum of all fin surfaces and the wetted base of the channel was taken, which is consistent with the convention set forth by [2, 4, 11]. This created a local heat transfer coefficient value using equation (18). Mixed-mean fluid temperature was calculated in CFD Post using the mass flow averaged temperature at individual work planes placed perpendicular to the fluid flow direction, following equation (19). ***Figure 31*** shows an example of these work planes and the points used to collected pressure and temperature data.

$$h = \frac{\dot{q}}{A_s(T_{mixed-mean} - T_{max-fin})} \quad (18)$$

$$T_{mixed-mean} = \frac{1}{\rho U_{mean} A_c} \int \rho u T dA_c \quad (19)$$

The average convective heat transfer coefficient was calculated as the arithmetic average of the local values of some number N. Using this value, the Nusselt Number and subsequent Colburn-j factor can be easily calculated using equations (11) and (12).

$$\bar{h} = \frac{\sum_{i=1}^{N} h_i}{N} \quad (20)$$

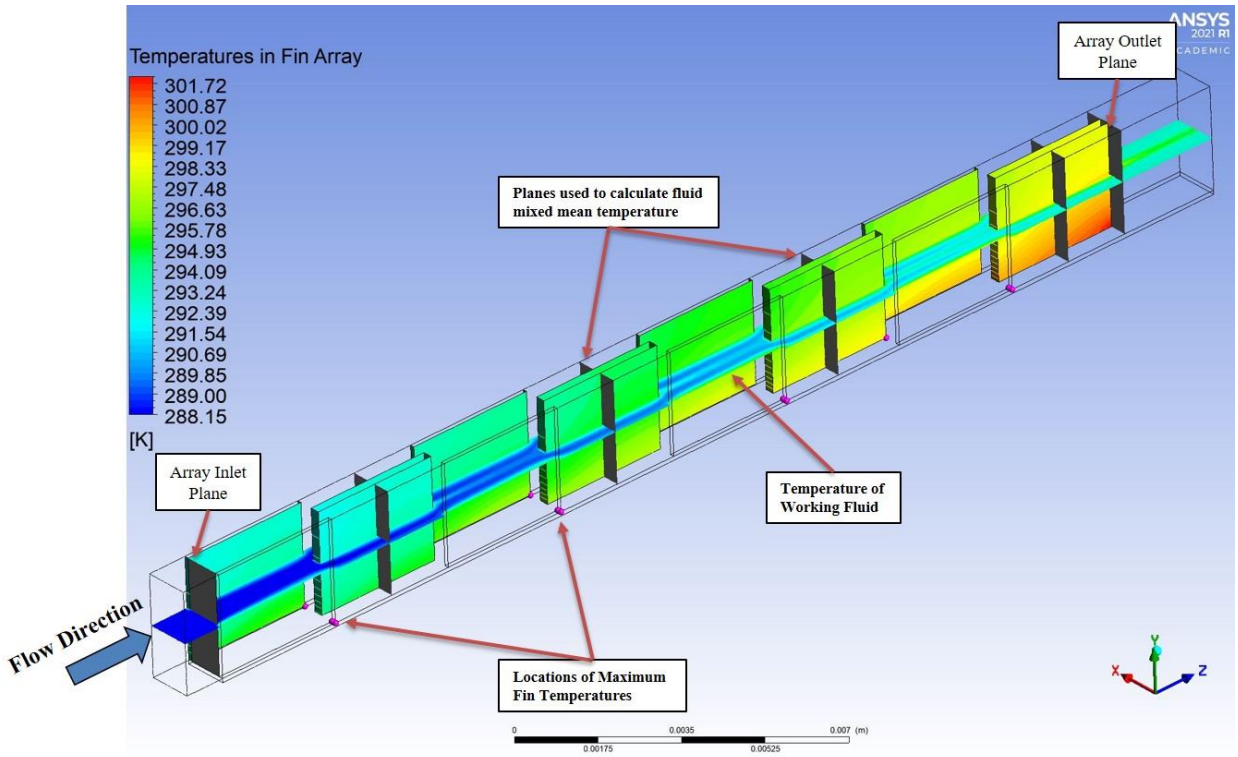

Figure 31: Temperature Fields in CFD Post

3.5 Validation of Numerical Simulation

3.5.1: Mesh Independence

The first step in validating the numerical simulation was to refine the mesh until mesh independence was achieved. Mesh independence was performed by decreasing the element size of the tetrahedral elements used in the fluid, increasing the number of boundary layers, and increasing the refinement around the leading and trailing edges of each fin. Mesh independence was achieved when both the pressure loss and maximum temperature differential in the computation domain were essentially the same between refined meshes. ***Table 6*** lists the design parameters changed to test for mesh independence. The pressure loss and maximum temperature differential in the computation domain were plotted against total number of elements in ***Figure***

32. From the results of the study, neither pressure loss nor temperature gain varied greatly for meshes greater than 6 million elements. As such, Mesh Scheme #11 was selected.

Table 6: Mesh Parameters Used for Mesh Independence Study

Mesh Number	Fluid Element Size [mm]	Number of Inflation Layers	Fin Length Sizing Number of Divisions	Fluid-Fin Impingement Face Element Size [mm]	Fin Element Size [mm]	Total Number of Elements
1	0.2	0	25	0.1	0.2	1.7E+05
2	0.15	3	25	0.1	0.2	3.1E+05
3	0.12	3	35	0.1	0.2	5.2E+05
4	0.1	3	50	0.1	0.2	8.7E+05
5	0.075	3	50	0.05	0.1	1.7E+06
6	0.075	5	50	0.05	0.1	1.9E+06
7	0.075	5	75	0.05	0.1	2.3E+06
8	0.06	5	75	0.05	0.1	3.3E+06
9	0.05	5	100	0.05	0.1	5.4E+06
10	0.05	7	100	0.05	0.1	5.6E+06
11	**0.05**	**7**	**100**	**0.025**	**0.1**	**6.9E+06**
12	0.05	7	125	0.025	0.1	7.7E+06
13	0.045	7	125	0.025	0.1	9.0E+06
14	0.045	7	150	0.025	0.1	9.7E+06

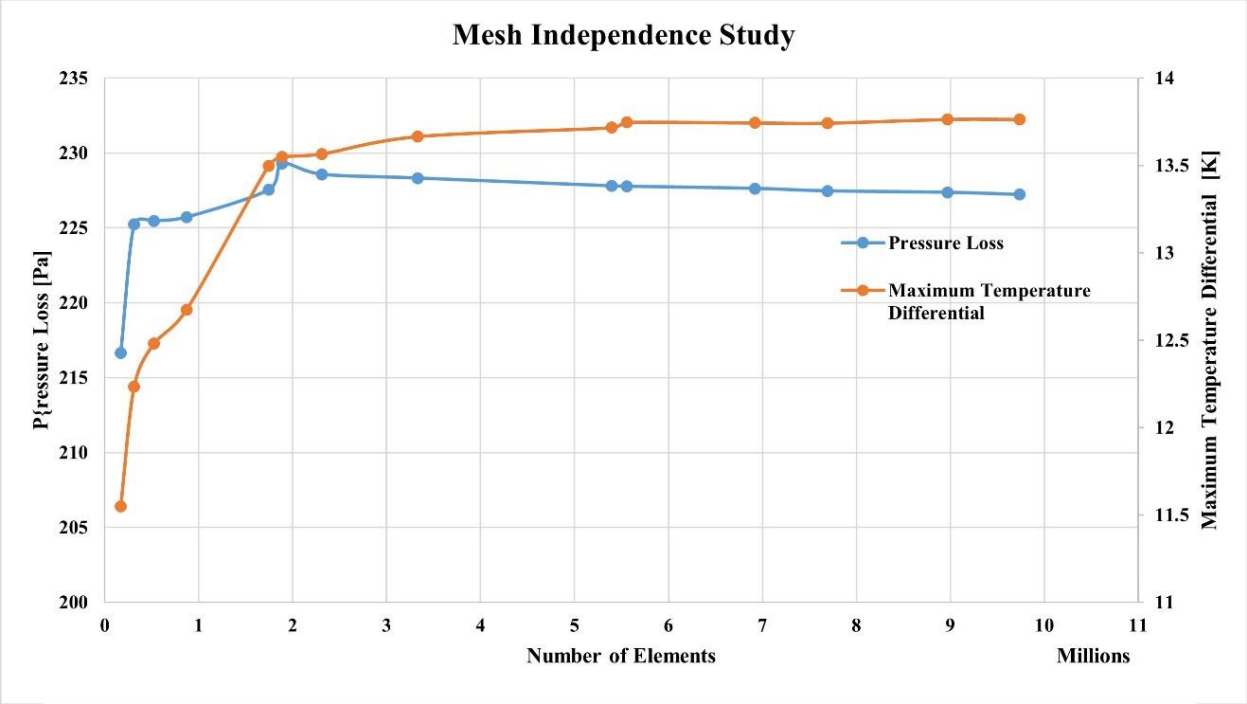

Figure 32: Results of Mesh Independence Study

3.5.2: Comparison against Pre-Existing Correlations

After mesh independence was established for the novel fin array designs, flow through the provided proprietary geometry was simulated under the same conditions as the novel fin array designs. Simulation of the proprietary array geometry allowed for comparison against the proprietary correlations, developed from experimentation, provided in the SOW. Additionally, these simulation results were compared to the correlations proposed by Manglik & Bergles.

As can be seen from the data presented in

Table 7: Validation of Numerical Simulation against Known Correlations and plotted in ***Figure 33***, relative difference between simulation results and the known correlations decreases with higher Reynolds number. As was discussed in Chapter 2, the correlations developed by Manglik and

Bergles were valid for a Reynolds number greater than 120. This was well above the current range, as such the large relative difference, which decreased as the Reynolds number decreased, was expected.

Table 7: Validation of Numerical Simulation against Known Correlations

Validation of Numerical Simulation									
	Re	16.67	21.85	27.03	32.22	37.41	42.60	47.80	52.99
Fanning Friction Facor Comparision									
M&D Correlation	f	0.89	0.73	0.62	0.55	0.49	0.45	0.41	0.38
Proprietary Correlation	f	1.06	0.86	0.72	0.63	0.56	0.51	0.46	0.43
Simulation Results	f	1.35	1.05	0.86	0.73	0.64	0.57	0.51	0.47
Error vs Proprietary Simulation	f	28%	22%	19%	16%	14%	12%	11%	10%
Error vs M&B	f	51%	43%	38%	33%	30%	28%	26%	24%
Colburn-J Factor Comparision									
M&D Correlation	j	0.11	0.10	0.09	0.08	0.07	0.07	0.06	0.06
Proprietary	j	0.115	0.101	0.091	0.083	0.078	0.073	0.069	0.066
Simulation Results	j	0.175	0.143	0.122	0.108	0.098	0.089	0.083	0.078
Error vs Proprietary Simulation	j	34%	29%	26%	23%	20%	18%	17%	16%
Error vs M&B	j	55%	46%	40%	36%	33%	31%	30%	28%

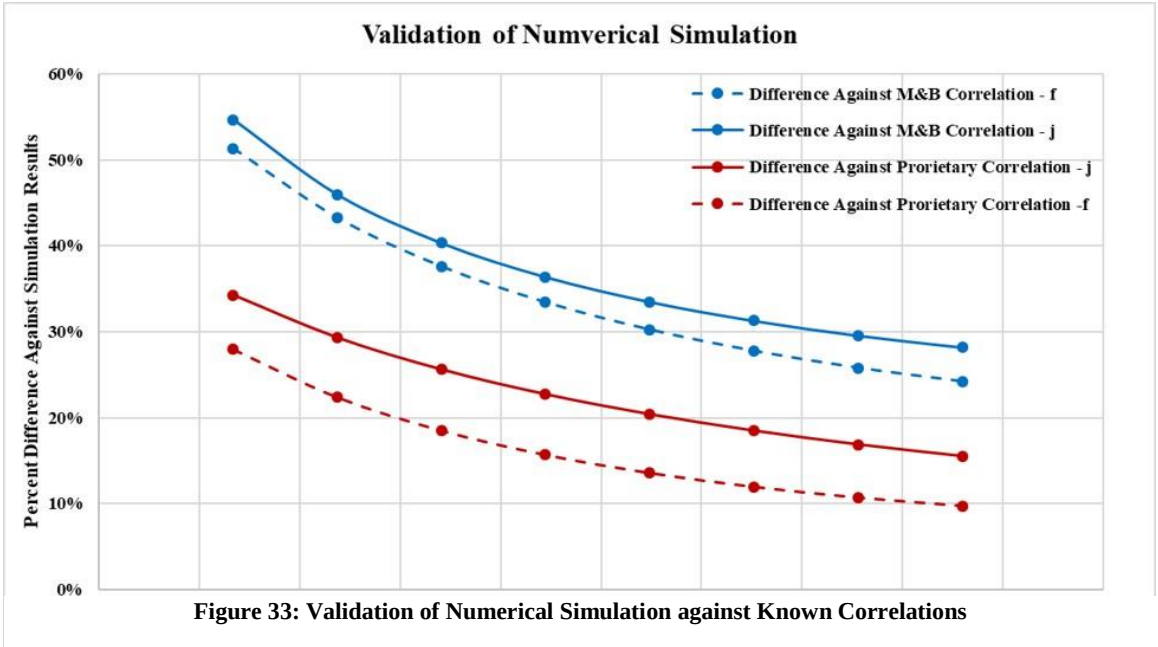

Figure 33: Validation of Numerical Simulation against Known Correlations

The relative difference between the simulated proprietary geometry's Fanning Friction and Colburn-J factors and the proprietary correlation was less than 20% at Re > 40. Owing the fact that the proprietary correlation is only accurate for Re > 50, this level of difference was deemed acceptable, and the numerical results and methods were considered to be validated.

Within this chapter the development of the numerical simulations used to predict the thermal and hydraulic performance of each of the novel fin arrays was discussed. Mesh independence was shown to occur around 6.8 million elements. The simulation methodology for collecting and processing data was shown to be sufficiently accurate by comparing simulation of the proprietary geometry to empirical correlations developed for the same geometry.

Chapter 4: Manufacturing of Cold Plates

4.1 Printing Methodologies of Considerations Influencing Design

When designing a part for an AM process, special attention must be paid to ensure a printed part is successful. Process Parameters, the set of instruction used to print an AM part, must be generated for each specific build plate. Settings such as the scan strategy, hatching speed, laser power, and powder dosing volume will all have a significant impact on the outcome of a print [28].

Over the course of this project, several iterations of cold plates were designed and printed. With each Build Plate (BP) iteration, process parameters and support geometry were subtly changed to stimulate print success. Of particular interest is the influence of part orientation on print success, this became the primary variable altered between build plate iterations.

To rate the successfulness of a printed part, a simple Failure Modes and Effects Analysis (FMEA) scale was used to qualify extreme print failures, moderate print failures, and successful prints. Extreme print failures resulted in cold plates that were unable to be tested in any capacity. Examples of such failures include cracked cold plates, designs that cause damage to the recoater blade, and extreme warping of cold plate flanges. Moderate print failures resulted in cold plates that were still testable but had strong room for improvement by reducing entrapped powder, number of interstitial foreign bodies, or removal of striations caused by uneven distribution of powder. Finally, successful prints created cold plates where removal of powder was verifiable and little to no extra post processing was required. **Figure 34** presents this scale with examples.

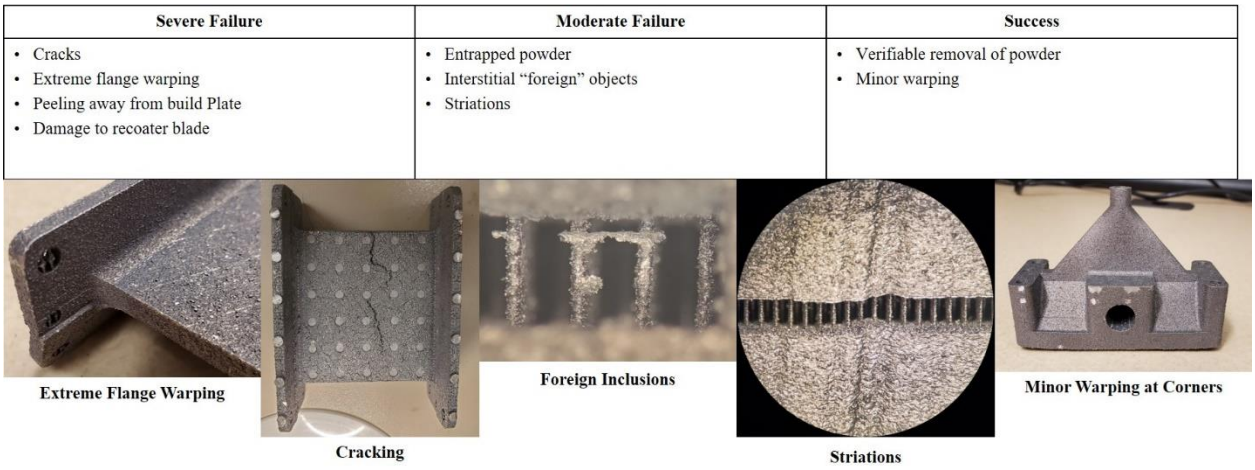

Figure 34: Guide for Rating Successfulness of Printed Part

X-ray CT was extensively used to verify removal of powder from fin arrays and to examine the internal fin structures. With the significant impact print orientation had on the development of the internal fin structures, Non-Destructive Evaluation (NDE) of the fin arrays within each cold plate was invaluable for making informed decisions regarding changes to print orientation.

4.2 Investigation of Proper Print Orientation

After the success of printing the small test coupons discussed in **Chapter 2**, larger 2" x 2" cold plates were designed for printing. Many of the initial build plate iterations were dedicated to determining what part orientation resulted in successful prints. Printing was performed in the Vertical, Angled, and Horizontal part orientations, shown in **Figure 35**.

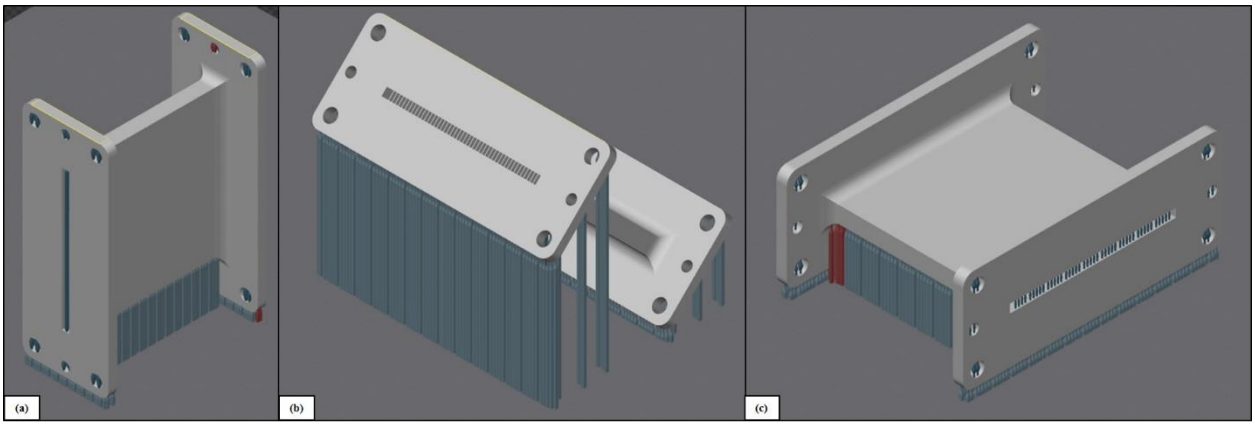

Figure 35: Cold Plate Print Orientations (a) Vertical (b) 45° (c) Horizontal

Of the three orientation tested, the Vertical print orientation proved to be the least successful. In this orientation, the fins were printed parallel with the substrate. This resulted in extreme under skin roughness on each individual fin caused by gravitational pull and capillary action on the melt pool [29].Fins were measured to be an average of 707µm thick, much thicker than the intended 200µm thickness. **Figure 36** shows the as-built cold plate as well as a close up view of the fins within the cold plate.

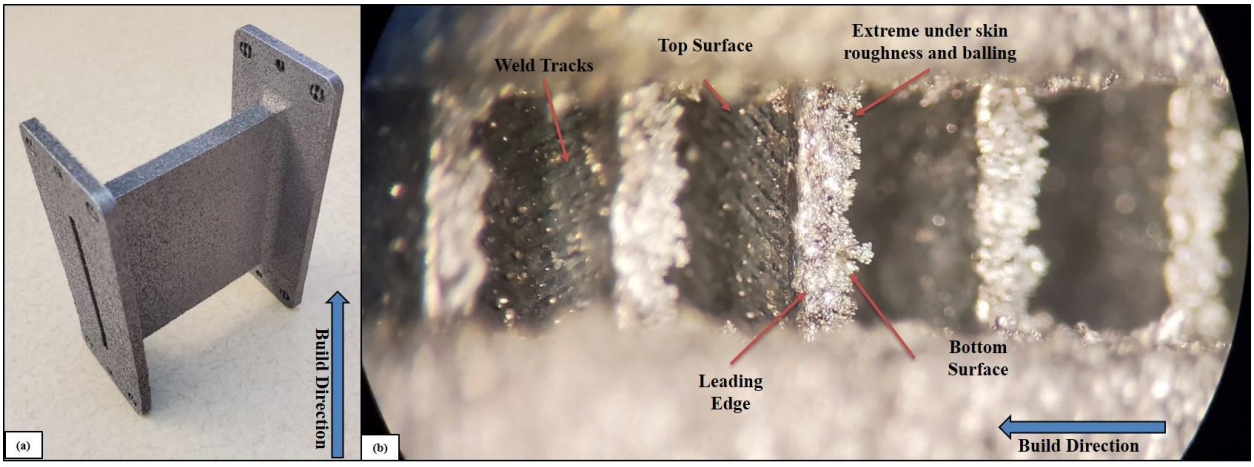

Figure 36: Vertical Print Orientation (a) As Build Cold Plate (b) Close-Up of Fin Array

When compared to test coupons printed in the Horizontal orientation, the increased fin thickness is clearly evident. This can be seen in **Figure 37**.

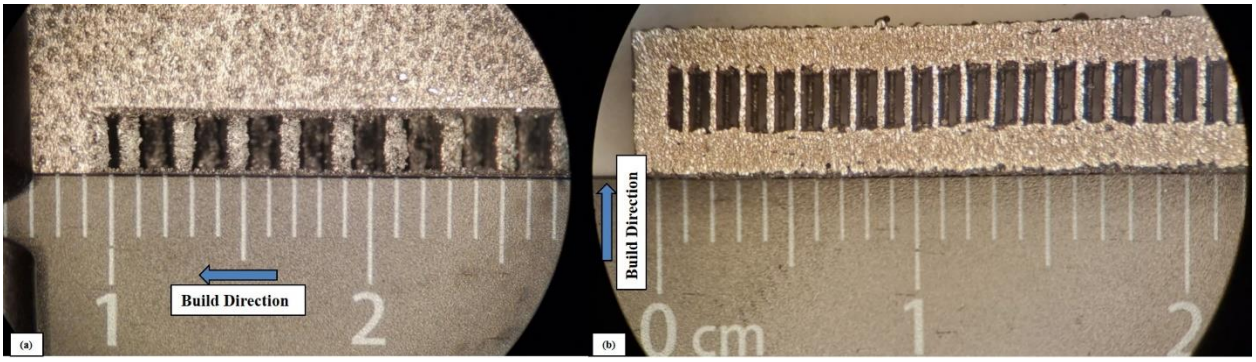

Figure 37: Comparison of Vertical Print Orientation and Horizontal Test Coupon (a) Vertical Cold Plate (b) 200µm-0µm Test Coupon Section

Greater success was found printing the cold plates angled 45° from the substrate's surface, as shown in **Figure 38**. This orientation reduced the foot print of the cold plate projecting onto the substrate's surface at each individual layer and is below the minimum self-supporting angle of 50° proposed by Kranz et al [7].

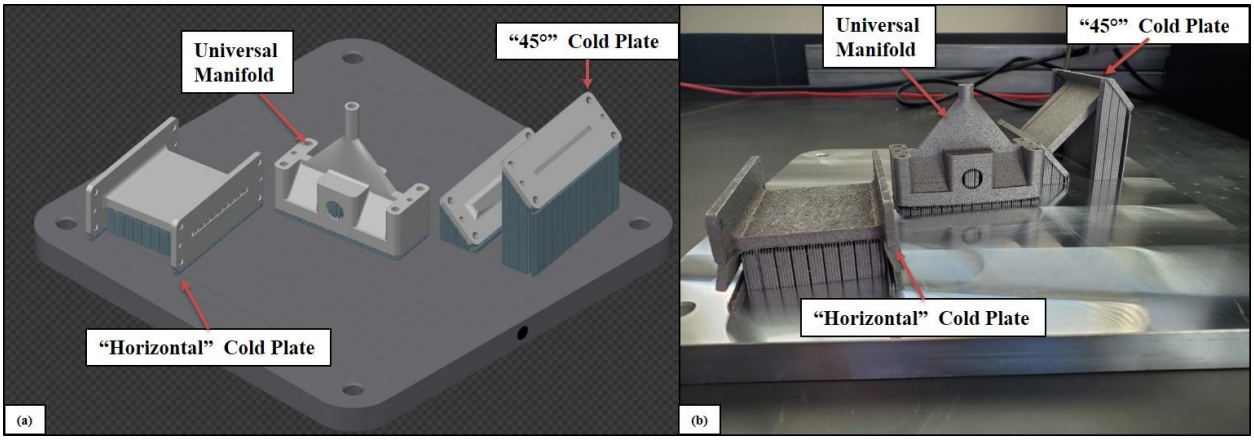

Figure 38: Layout of BPV5 (a) As Seen in Print Slicing Software (b) As-Built Build Plate

When examining the internal fin array using x-ray CT, the fins were found to be well developed and no entrapped powder or damage from the printing process was evident. Shown in **Figure 39**, the fins appear regularly uniform in shape, length, and thickness.

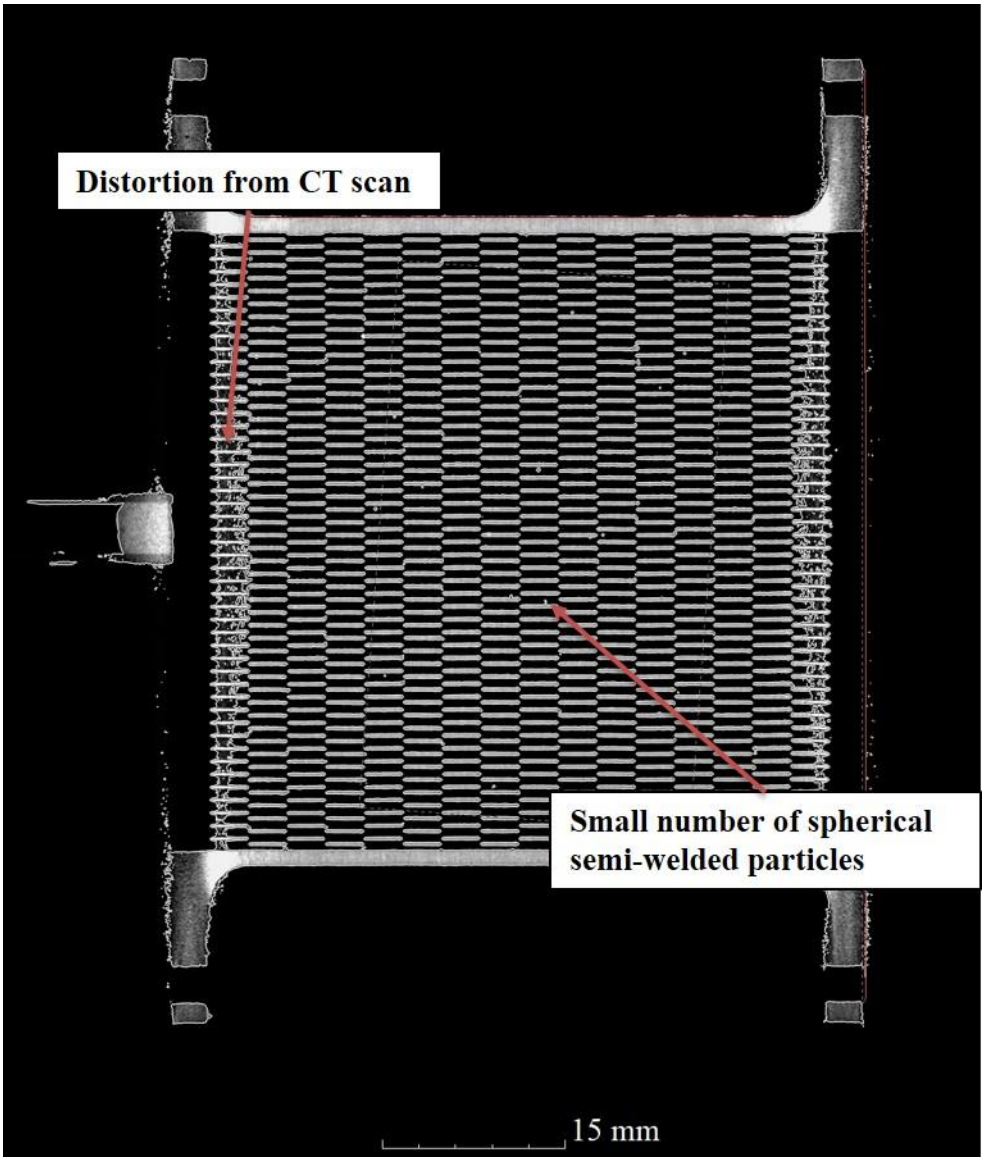

Figure 39: Top View of 45° Cold Plate Printed on BPV6

The images from the CT scan were post-processed using the software package MyVGL V3.5 to determine the thickness of the fins. The thickness ranged from 210 to 280 μm. A small

number of semi welded particles of varying diameters can be seen attached to fin surfaces; however, these particles appear less frequently than what was observed for the Vertical print orientation. **Figure 40** provides a Front view taken at the middle and trailing edge of a column of fins. It is evident from this figure, that the trailing edge fins experienced a higher number of semi-welded particle obstructions in comparison to fins in the middle of the of the cold plate. It is believed that this is due to the greater likelihood of contact with the un-sintered powder when printing trailing edge fins. During the printing process, local melt pool dynamics can cause the melt pool to expand into the un-sintered powder beyond the desired hatched region. As printing layers increase, sintered material in previous layers minimize this effect and effectively reduce the probably of unwanted powder sintering. From this figure, more semi-welded particles were evidenced to appear on the trailing edge of the fins, caused by the contact between the trailing edges and the un-sintered powder.

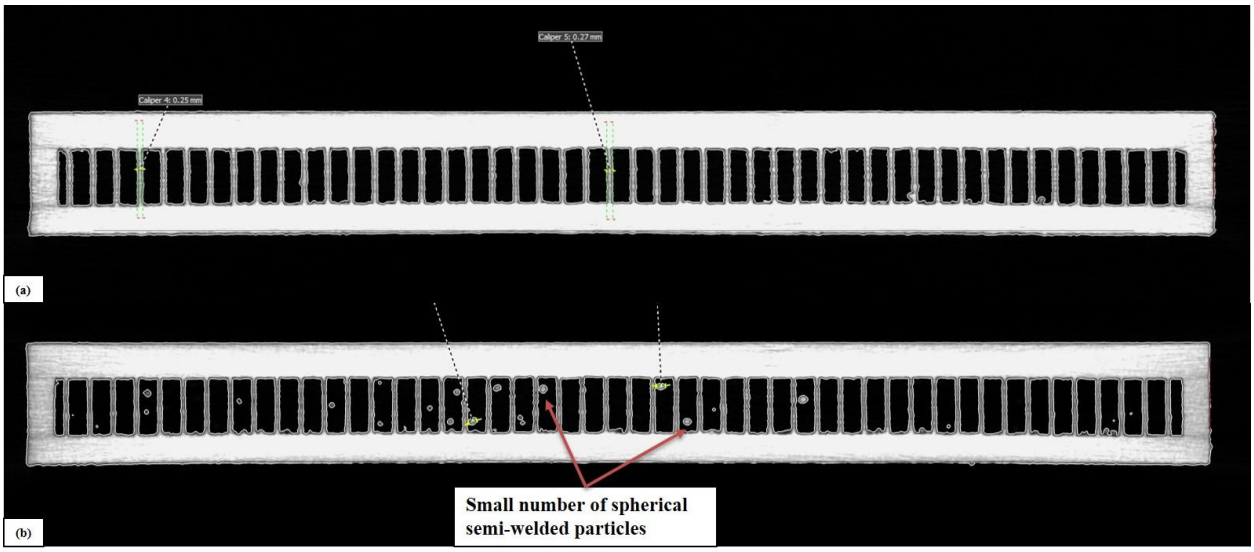

Figure 40: Front View of 45° Cold Plate Printed on BPV6 (a) Middle of Fin Column (b) Trailing Edge of Fin Column

By printing at an angle from the surface of the substrate, the overall height of the build plate is increased, consequently increasing volume of powder needed for printing. When printing small test coupons this extra volume of powder utilized may be trivial; however, if the size of the printed part increases, the volume of powder required can increase dramatically. Thus, it became beneficial to explore printing the cold plate horizontal with the substrate's surface.

Printing in the horizontal orientation proved to be more susceptible to severe print failure, and several Build Plate iterations were needed to create successful prints. **Figure 41** shows several examples of severe print failure that occurred while using this orientation.

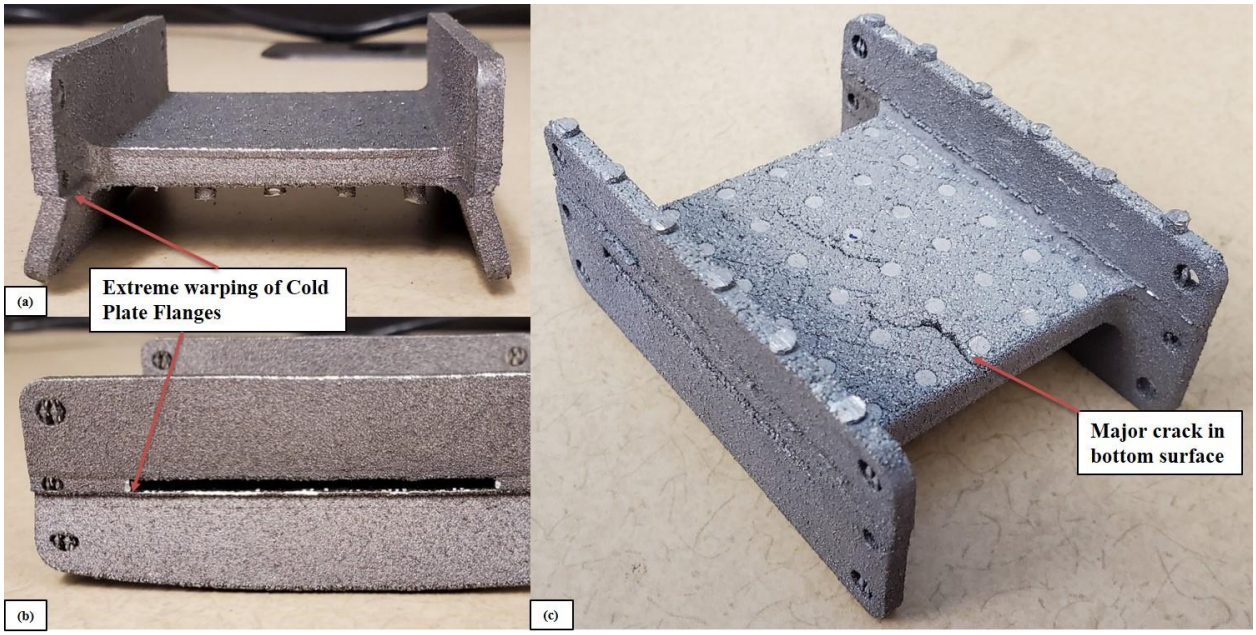

Figure 41: Example of External Failure Modes Seen in Horizontal Print Orientation (a) Side View of Extreme Flange Warping Seen in BPV5 (b) Front View of Extreme Flange Warping Seen in BPV5 (c) Crack In Underside of BPV6 Cold Plate

These extreme failures often resulted in severe damage to the internal fin geometries as shown in **Figure 42**. Issues with entrapped powder, sub-surface voids, and distortions of the fin

array were common in the initial build plate versions. Additionally, the as-built thickness of the fins varied extensively, measuring between 230µm to 270µm thick, with some of the more severely malformed fins measuring 410µm.

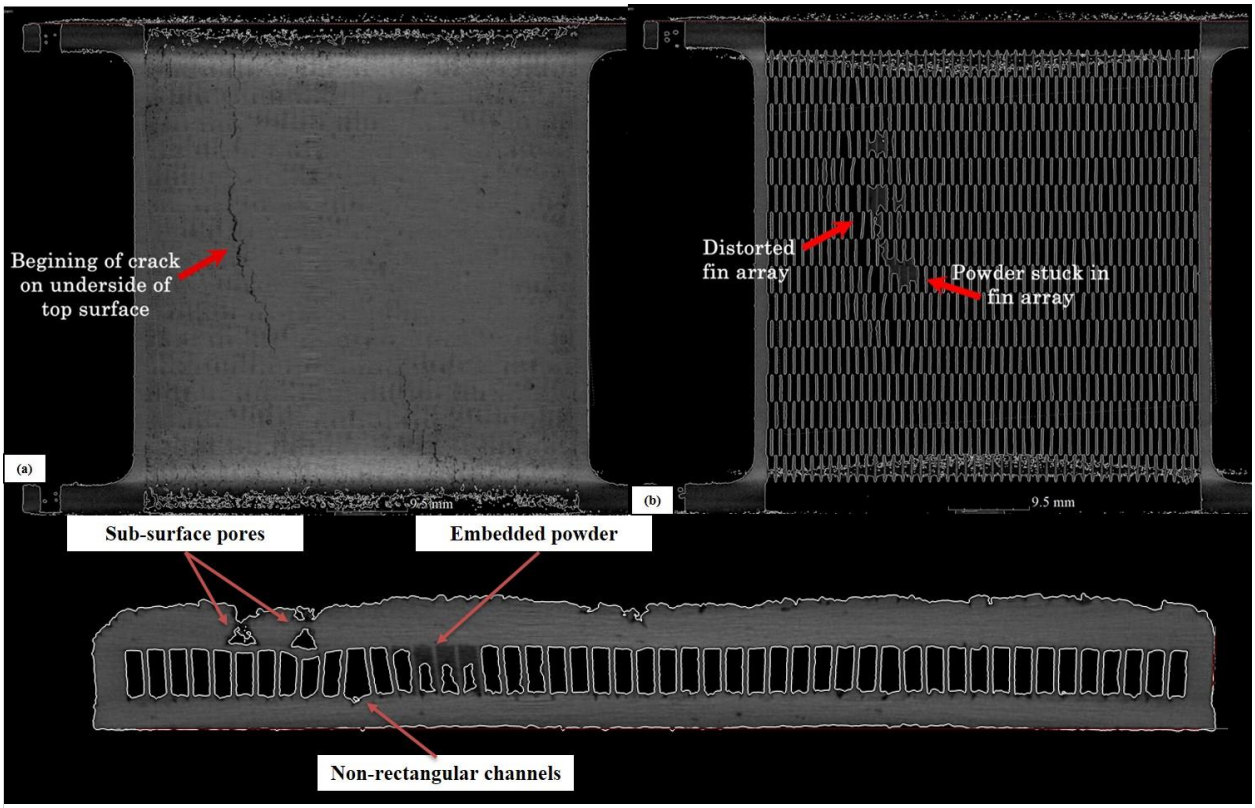

Figure 42: Internal Failures of Horizontal Print orientation (a) Top View of Crack Forming on Underside of Cold Plate (b) Damage to Fin Array From Thermal Warping (c) Front View of Sub-Surface Defects and Damage to Fin Array

To remedy this issue, the density and diameter of the support structures used to prevent the cold plate from peeling off the substrate was varied until the proper balance was reached. This resulted in the successful printing of a cold plate in the Horizontal orientation, free of any embedded powder, sub-surface pores, voids, cracks, or damaged fins in the array as can be seen in **Figure 43**. The fins within this array had an average thickness of 224µm, only slightly above the desired 200µm thickness.

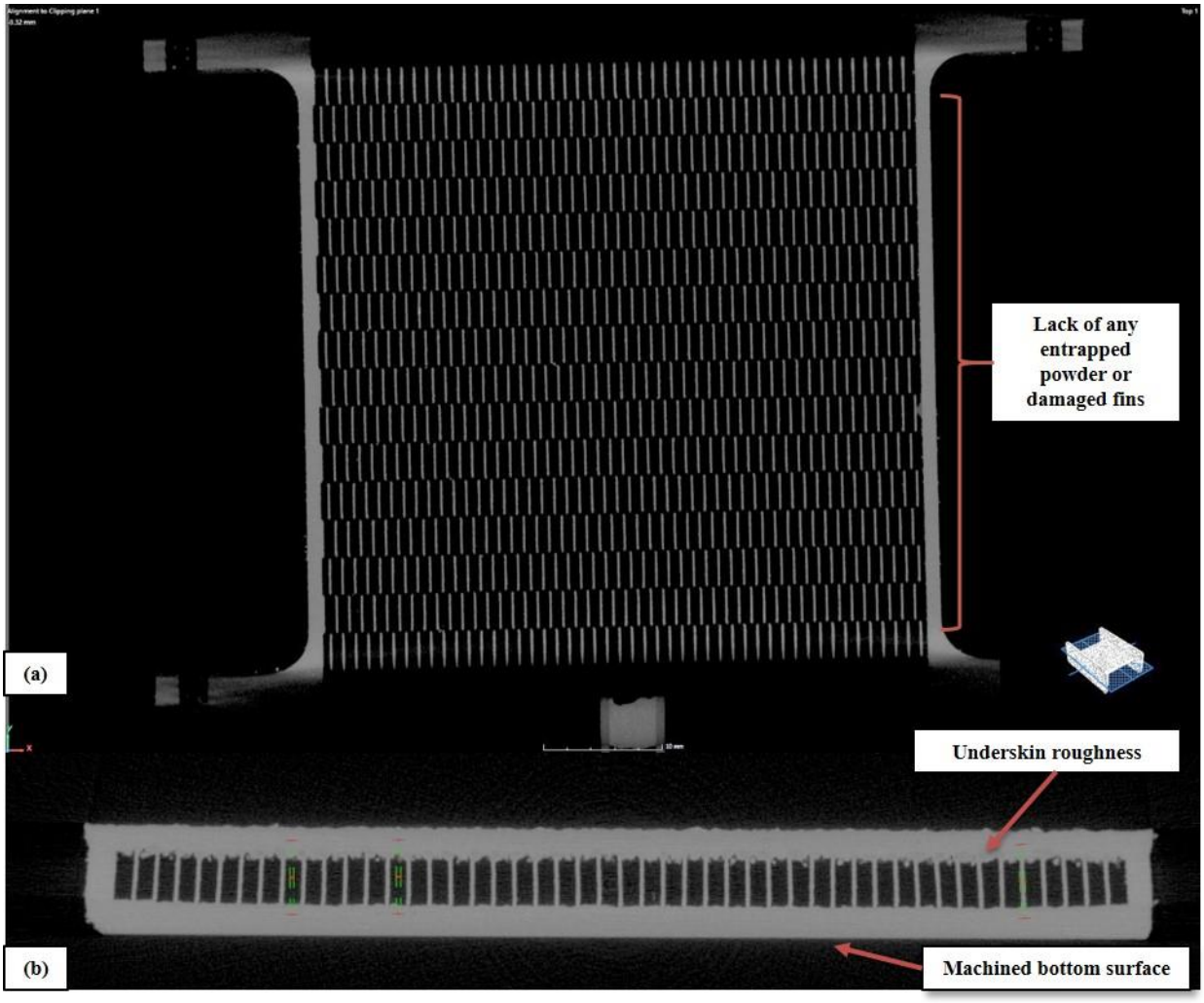

Figure 43: Successful Horizontal Print Orientation (a) Top View of Fin Array (b) bottom View of Fin Array

4.2 Rectangular Strip Fin Arrays

A total of four cold plates with rectangular offset strip fin arrays were successfully printed using both the Horizontal and 45° print orientations. Within these arrays, fin thickness was held constant at 200µm and the offset spacing was varied from 0µm to 200µm. All fin arrays were clear of any entrapped powder or large interstitial foreign bodies. **Figure 44** compares the offset distance in the printed fin arrays.

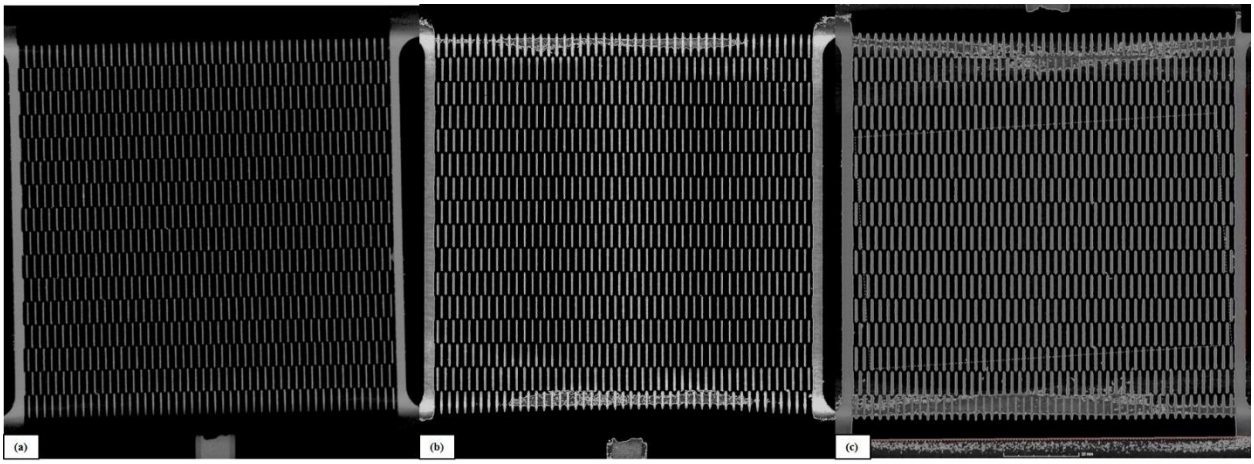

Figure 44: Comparison of Fin Offset Distance in Printed Rectangular Fin Arrays (a) 0µm Offset (b) 100µm Offset (c) 200µm Offset

The fin array shown in **Figure 44**(b) had a designed offset distance of 100µm; however, the as-built offset was much larger, measuring between 100µm and 260µm with an average of 184µm. Contrarily, the cold plate with the designed offset distance of 200µm, **Figure 44**(c), had an average measured offset of 187µm, varying between 110µm and 250µm. The dimension of this offset distance in the CAD files used for printing these parts was confirmed to be correct, and the print settings were consistent with previous successful prints. The specific cause for the increased offset distance in the 200µm-100µm cold plate is currently unknown.

4.3 Alternative Array Geometries

To take advantage of the design freedom offered by AM processes, several fin arrays were designed to deviate from the conventional rectangle offset strip fin array. The goal of these new fin designs was to minimize the pressure loss through the fin array while preserving surface area for convective heat transfer to take place.

4.3.1 “Elliptical” Fin Arrays

This first alternative design sought to meet the goals outlined above by tapering the leading and trailing edges of each fin to a diameter of 150µm, and the fin slowly increases in thickness to 200µm at the middle, similar to the shape of an ellipse. By tapering the leading and trailing edges of the fin, more flow area becomes available to the fluid, reducing pressure loss. ***Figure 45*** compares the dimensions of the elliptical fin to that of a normal rectangular fin.

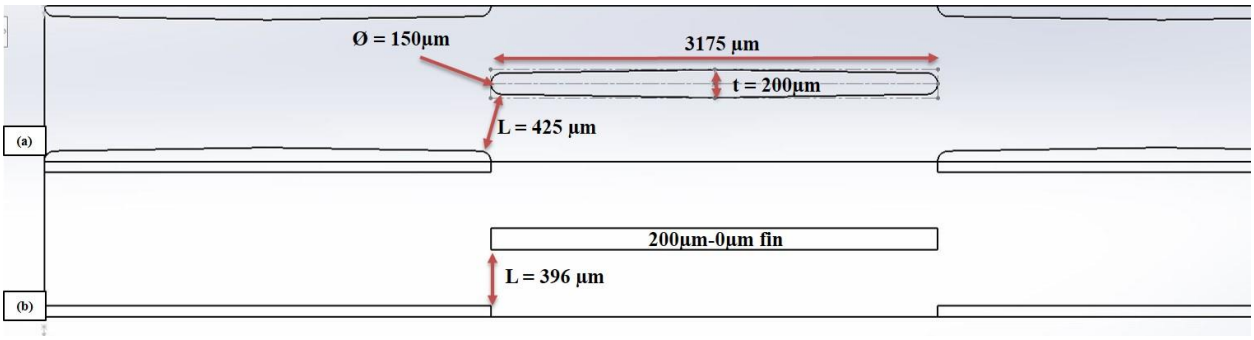

Figure 45: Geometry of "Elliptical" Fin Compared to Rectangular Fin (a) Elliptical Fin (b) Rectangular Fin

Several 1” x 1” test coupons of the elliptical fin array were designed and printed. However, upon inspection of the fin array, the fins were all of a uniform thickness and possessed a rectangular cross section, ***Figure 46***. Average fin thickness was measured to 254µm. It appears that the subtle changes to the fin features were below the minimum XY resolution the machine could execute. This issue has the potential to be circumvented by clever manipulation of machine process parameters, and provides an excellent continuation for future studies. Simulations of this geometry were performed and were compared to the other novel fin array designs

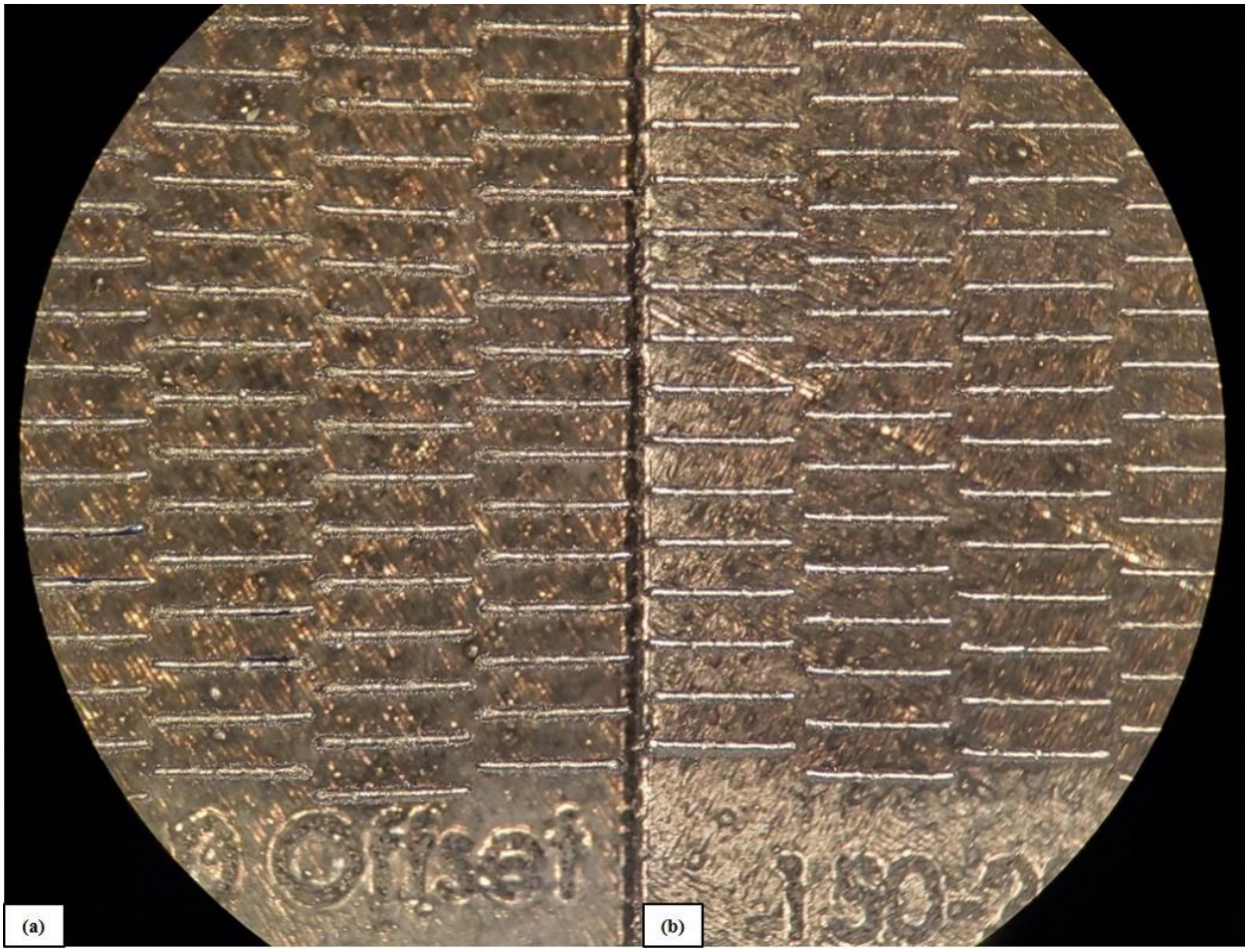

Figure 46: Comparison of Elliptical Fin Array to 200µm-0mµm Fin Array (a) 200µm-0mµm Fin Array (b) Elliptical Fin Array

4.3.2 Wavy Fin Arrays

The final alternative fin design utilized an array of interrupted wavy fins. By curving each fin, the length of the flow path the fluid was required to traverse was increased, motivating heat transfer into the fluid. A total of three 1"x1" test coupons of wave amplitudes (A) 100µm, 150µm, and 200µm were printed, shown in ***Figure 47***. Fin thickness was held at a constant 200µm.

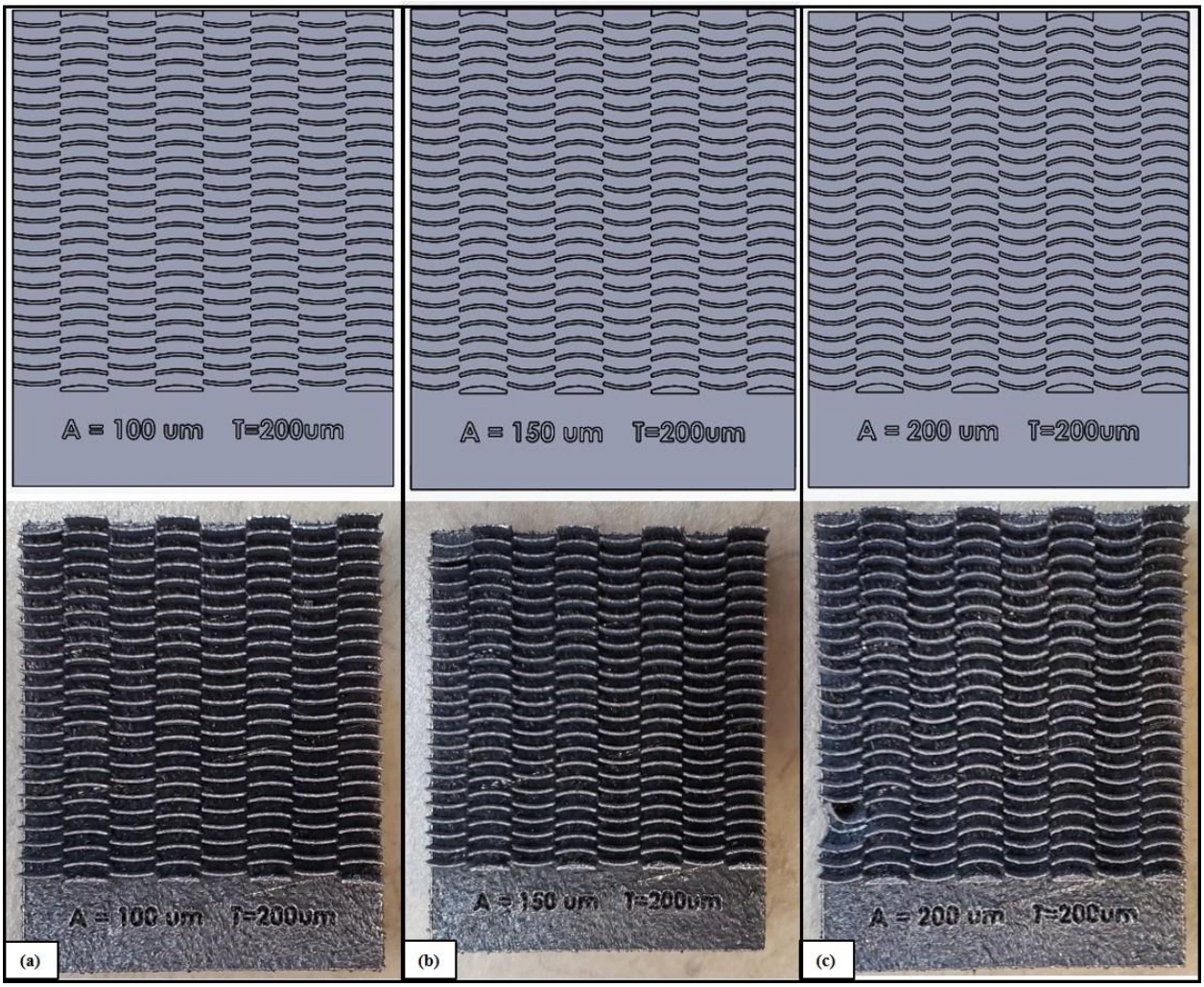

Figure 47: Comparison of Designed vs. As-Build Wavy Fin Arrays (a) A = 100µm (b) A = 150µm (c) A = 200µm

Each of the wavy fin test coupons designed were able to be successfully printed, with only minor damage to the A = 200 array. Due to the repeating, non-symmetric nature of the wavy fin geometry, simulation of flow through the A = 100µm wavy fin geometry was performed utilizing translational periodic boundary conditions. These boundary conditions required Mesh Matching Controls to be utilized to create identical meshes on the periodic boundaries. These requirements greatly limited the ability to simulate flow through these fin structures in ANSYS. As such, only

flow through the A = 100µm, **Figure 47**(b), was completed. Future work will include printing and testing 2"x 2" wavy fin test coupons as this geometry holds great promise.

4.4 Overview of Final Cold Plate and Fin Designs

Of the novel fin arrays designed for printing, only the four cold plates with rectangular strip fin arrays were considered sufficiently defect free to be tested. These cold plates were named utilizing a simple three character number scheme where the first number is the designed fin thickness, the second is the designed fin offset, and the final number refers to the Build Plate (BP) iteration on which the cold plate was printed. ***Figure 48*** shows the breakdown of this naming scheme. The average fin thickness, print angle, and average fin offset spacing for each rectangular fin array was recorded and is presented in **Table 8**.

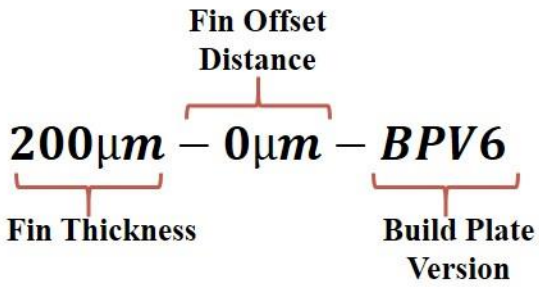

Figure 48: Break Down of Cold Plate Naming Convention

Table 8: Geometries of Print Cold Plates

Fin Array Name	Print Angle [°]	Averge Fin Thickness [µm]	Standard Deviation in Fin Thickness [µm]	Average Fin Offset Distance [µm]	Standard Deviation in Average Offset Distance [µm]
200µm-0µm-BPV6	45	237.0	15.1	N/A	N/A
200µm-0µm-BPV8	0	224.0	15.2	N/A	N/A
200µm-100µm-BPV8	45	183.3	25.3	184.3	43.3
200µm-200µm-BPV8	45	277.0	13.5	187.0	37.3

Chapter 5: Results

5.1 CFD Results

For each of the novel fin arrays designed, pressure loss and temperature gain was simulated to compare against experimental results. All simulations were run using DOW Therm SR1 as the working fluid with temperature dependent fluid properties. Heat was added to the fin array by a constant heat flux boundary condition at the base of the fin array and transferred into the fluid via aluminum fins.

5.1.1 Comparing Novel Fin Arrays

When comparing the Fanning friction and Colburn-j factors, the channel Reynolds number, defined in equation (9), was used as the independent variable to represent the effect of flow rate on thermal/hydraulic performance. However, in order to rank the performance benefits amongst cold plates with differing fin array designs, metrics identifying changes in geometric features were considered. These include: (i) changes in surface area available for heat transfer, and (ii) changes in the surface area-to-volume ratio (i.e. "compactness") of the design.

The total surface area available for heat transfer (A_s), the sum of all fin surfaces and the wetted base of the channel, can be compared against the total surface area available for heat transfer in the proprietary array (A_{s-BL}), against the volume of the cold plate (V_{cp}), or against the footprint of the cold plate (A_{fp}) to produce a nondimensional comparison factor that is consistent across every design. The ratio of total surface area available for heat transfer to a baseline surface area (SA_R) is useful for showing the gain or loss in available heat transfer area between designs.

Designs with ratios above one represent a design with more area available compared to a baseline array.

$$SA_R = \frac{A_s}{A_{s-BL}} \tag{21}$$

The ratio of total surface area available for heat transfer can be compared to the volume of the cold plate (V_{cp}), and can be used to determine the compactness of the cold plate. The cold plate will be classified as "compact" if its surface area available for heat transfer to volume ratio exceeds 700 m^2/m^3 (213 ft^2/ft^3) [5].

$$AV_R = \frac{A_s}{V_{cp}} \tag{22}$$

The ratio of surface area available for heat transfer and foot print the cold plate occupies FA_R) can also be useful for classifying the compactness of the cold plate design.

$$FA_R = \frac{A_s}{A_{fp}} \tag{23}$$

Table 9 provides the calculated values for the non-dimension geometric comparisons described above. From surface area available for heat transfer ratio, all novel array designs are classified as "compact" using Shah's definition for compact heat exchangers [2].

Table 9: Calculated Non-Dimension Geometric Properties of Novel Array Designs

Novel Fin Array	200µm-0µm	200µm-100µm	200µm-200µm	200µm-300µm	Elliptical	Wavy Fin
$A_s\ [m]$	1.59E-04	1.55E-04	1.52E-04	1.49E-04	1.55E-04	1.59E-04
SA_R	1.012	0.987	0.969	0.947	0.986	1.014
$AV_R\ [m^{-1}]$	2328.67	2271.68	2228.75	2178.70	2285.54	2334.34
FA_R	5.91	5.77	5.66	5.53	5.81	5.93

5.1.2 Hydraulic Performance of Novel Fin Arrays

The hydraulic performance of each novel fin array was characterized using the apparent Fanning friction factor as shown in equation (7). These simulation results were compared to a separate numerical simulation of the proprietary geometry, the proprietary correlation, and the analytical solution to fully developed flow through a rectangular duct of equal aspect ratio (f_{f-FD}) shown in equation (24) and **Figure 49** [1]. Simulation of flow through the proprietary geometry was performed to allow a consistent comparison of f_{app} using only simulation results and not mixing simulation and experimental results.

$$f_{f-FD} = \frac{1}{4} * \frac{69}{Re_{D_h}} \tag{24}$$

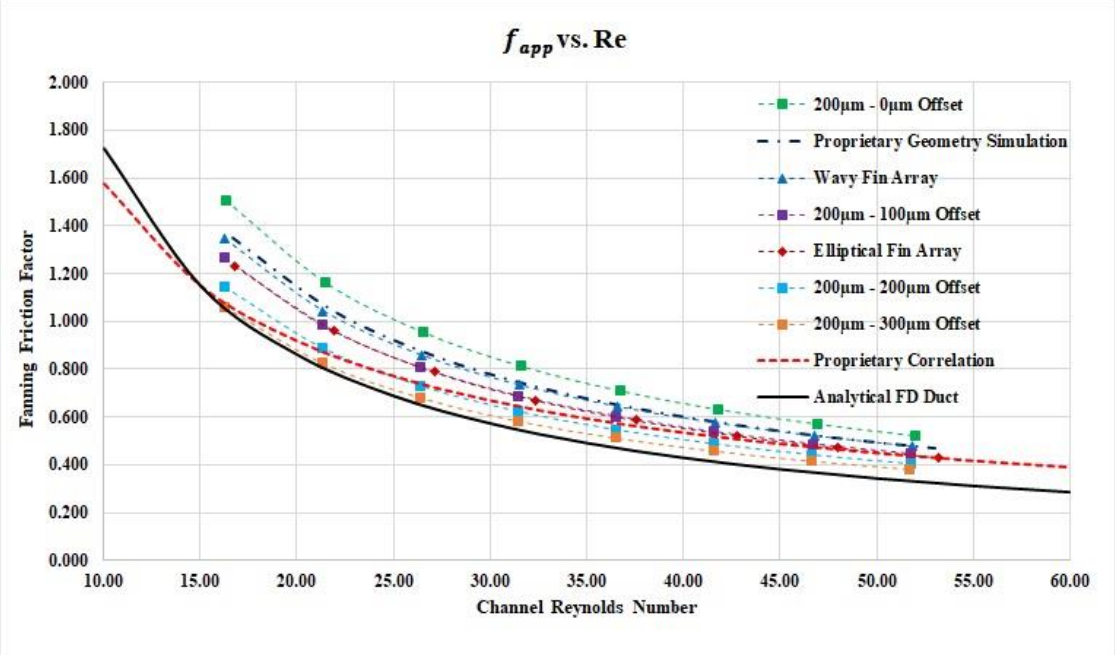

Figure 49: Fanning Friction Simulation Results

From the figure, f_{app} substantially decreases as additional fin offset distance is added. Consequently, the 200µm-0µm array yielded the highest pressure loss. Of particular interest is the performance of the wavy fin geometry which had values of f_{app} very near those of the obtained from the simulated proprietary geometry despite possessing slightly increased surface area.

The effect of fin offset distance in the rectangular strip fin arrays was characterized by calculating the relative difference in f_{app} between each fin array. Equation (25) provides the equation used to calculate the relative difference in f_{app} between the novel rectangular strip fin arrays, marked as 200µm-"***X***"µm where "***X***" is the offset distance.

$$\Delta f_{\%Diff-Novel} = \frac{f_{200\mu m-0\mu m} - f_{200\mu m-"X"\mu m}}{f_{200\mu m-0\mu m}} \tag{25}$$

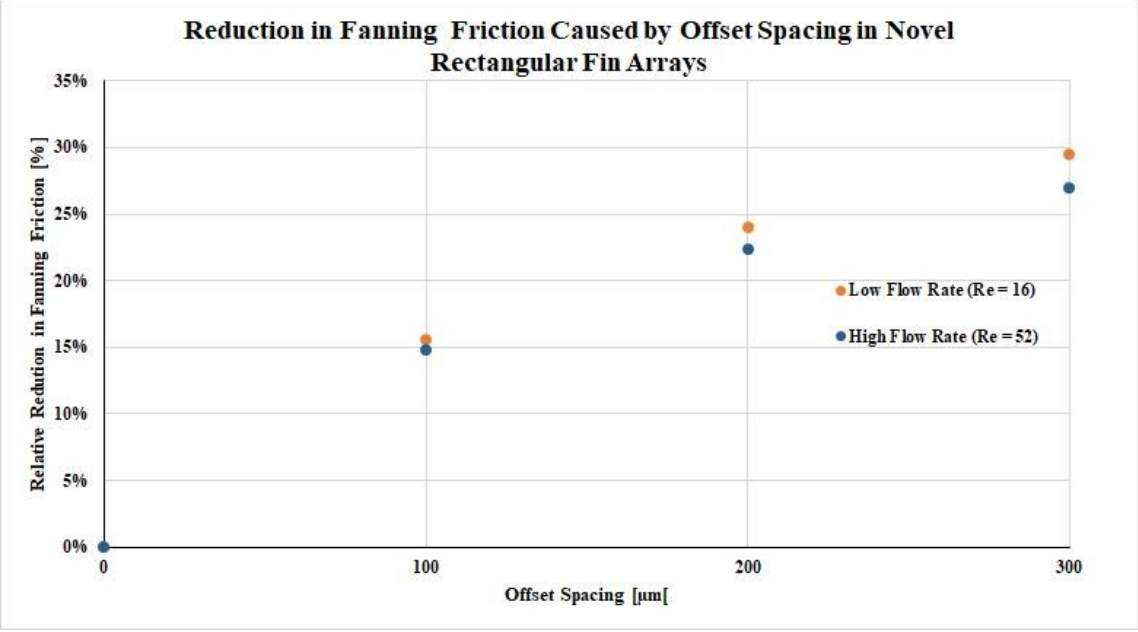

Figure 50: Reduction in f_{app} Caused by Offset Spacing vs Other Novel Rectangular Fin Arrays

From the figure above, the addition of a gap between subsequent columns of fins greatly improves the value of $\Delta f_{\%Diff-Novel}$. By increasing offset distance from 0µm to 100µm, $\Delta f_{\%Diff-Novel}$ decreases by ~15%. However, this benefit diminishes as the distance increases further, and the measured improvement is only 5% when increased from 200µm to 300µm.

The same process described above was used to compare the effects of offset distance in the novel rectangular strip fin arrays to the f_{app} value calculated from simulation of the proprietary geometry. Equation (25) was slightly reworked into equation (26).

$$\Delta f_{\%Diff-Propietary} = \frac{f_{Proprietary} - f_{200\mu m-"X"\mu m}}{f_{Proprietary}} \quad (26)$$

Again, a positive value represents an improvement in the hydraulic performance, a reduction in pressure loss across the array, while a negative value represents a worse performance where pressure loss across the array has increased. ***Figure 51*** plots the relative difference in pressure loss versus the offset spacing at the lowest and highest experimental volumetric flow rates.

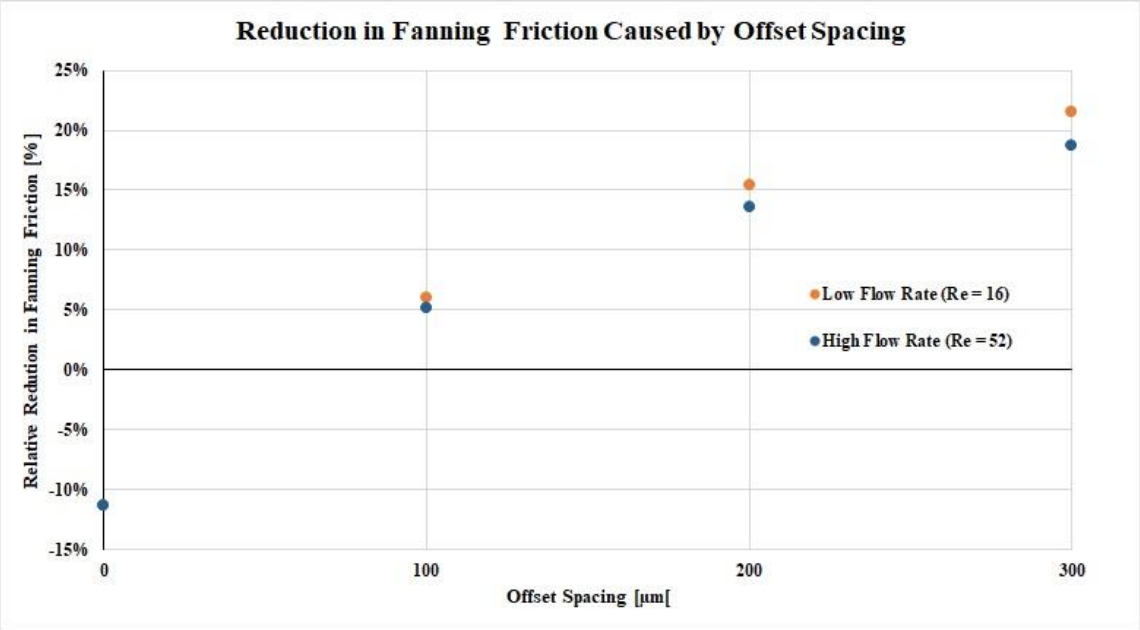

Figure 51: Reduction in f_{app} Caused by Offset Spacing vs Proprietary Geometry

From this figure, the addition of the fin offset distance reduced calculated pressure loss to a value lower than what was calculated from simulation of the proprietary geometry. The 200µm-300µm fin array produced a 20% decrease in f_{app}. However, improvements offered by increasing the fin offset distance diminished as the offset distance increased. When increasing the offset from 0µm to 100µm, the reduction in f_{app} was calculated to be ~17%; whereas, when the offset is increased from 200µm to 300µm the reduction was only ~ 6%.

5.1.3 Colburn-j Factor Performance

The thermal performance of each simulated fin array was first examined by calculating the Colburn-j factor based on the average Nusselt number as outlined in **Chapter 3**. These simulation results were again compared to a separate numerical simulation of the proprietary geometry, the

proprietary correlation, and the analytical solution to fully developed flow through a rectangular duct of similar aspect ratio, shown in equation (27) [1].

$$Nu_{FD} = 4.79 \tag{27}$$

Figure 52 plots Colburn–j factor against channel Reynolds number. From this figure, the addition of the fin offset distance has a less noticeable effect on Colburn-j factor than on Fanning Friction factor. All simulated geometries differed only slightly from the simulation results of the proprietary geometry, but were well above the *j* value for fully developed flow in a rectangular duct.

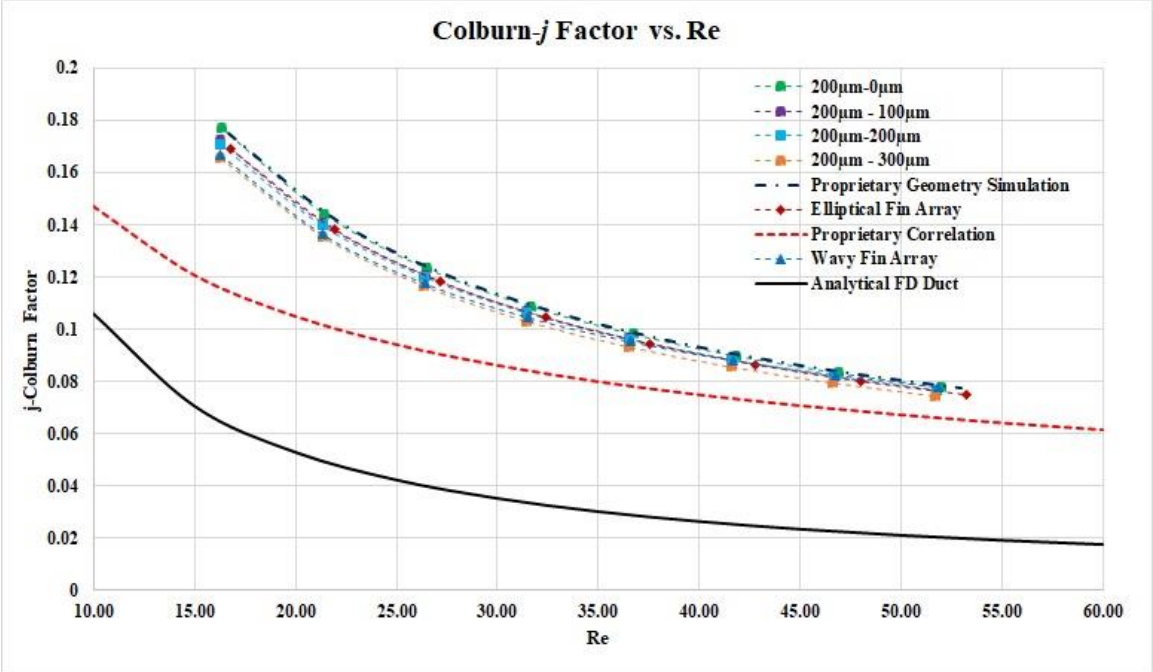

Figure 52: Colburn j Factor Simulation Results

Similar to the plots created to show the effects of fin offset distance on f_{app} , the relative difference in Colburn-j factor between the novel rectangular fin arrays and the proprietary geometry was calculated using equations (28) and (29).

$$\Delta j_{\%Diff-Novel} = \frac{j_{200\mu m-0\mu m} - j_{200\mu m-"X"\mu m}}{j_{200\mu m-0\mu m}} \tag{28}$$

$$\Delta j_{\%Diff-Propietary} = \frac{j_{Proprietary} - j_{200\mu m-"X"\mu m}}{j_{Proprietary}} \tag{29}$$

Figure 53 compares the effects of fin offset distance on relative difference between each novel rectangular fin array using equation (28). From the figure, increasing the offset distance very slightly decreases Colburn-j factor. Between 0µm and 100µm, *j* decreased by 1.93%; whereas, between 200µm and 300µm *j* decreased by 3.05%.

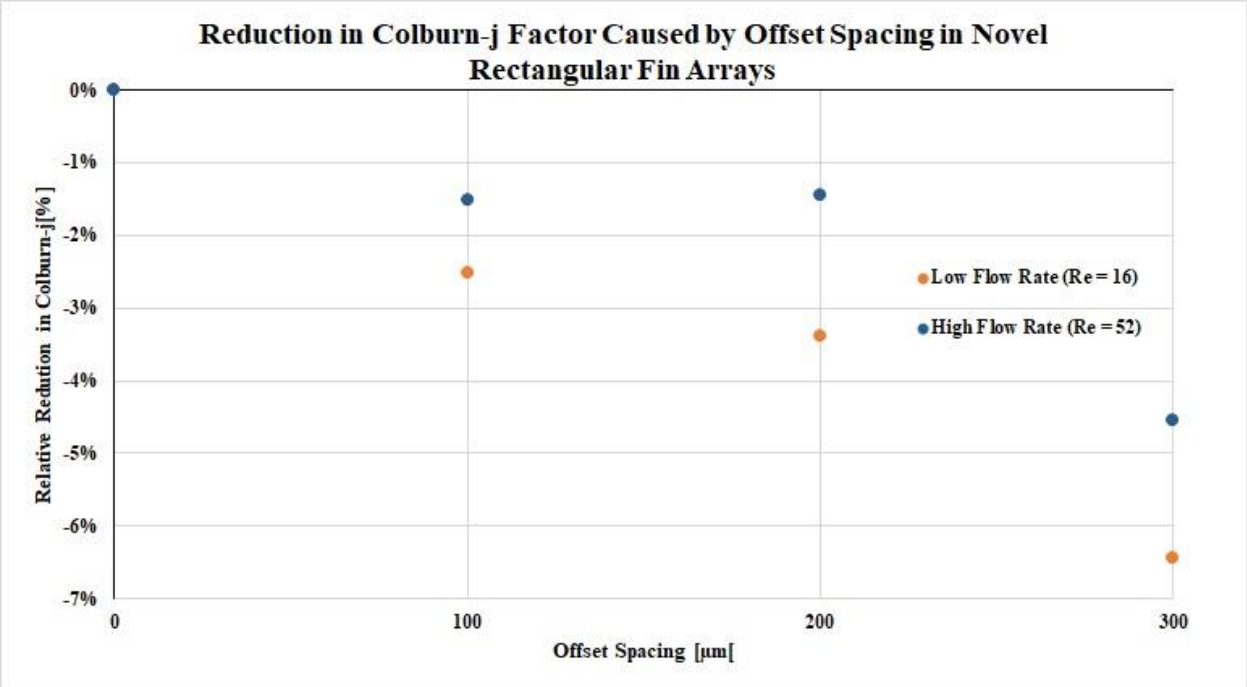

Figure 53: Reduction in *j* Caused by Offset Spacing vs Other Novel Rectangular Fin Arrays

Figure 54 plots the effect of offset distance on the relative difference between *j* of the novel rectangular fin arrays and the *j* value calculated from simulation of the proprietary geometry using equation (29). From this plot, only the array without any offset spacing slightly outperformed the proprietary geometry by ~1%. As was seen in ***Figure 53***, the relative difference increased with increasing offset distance such that the difference between the proprietary geometry and the 200µm-300µm array was ~4.8%.

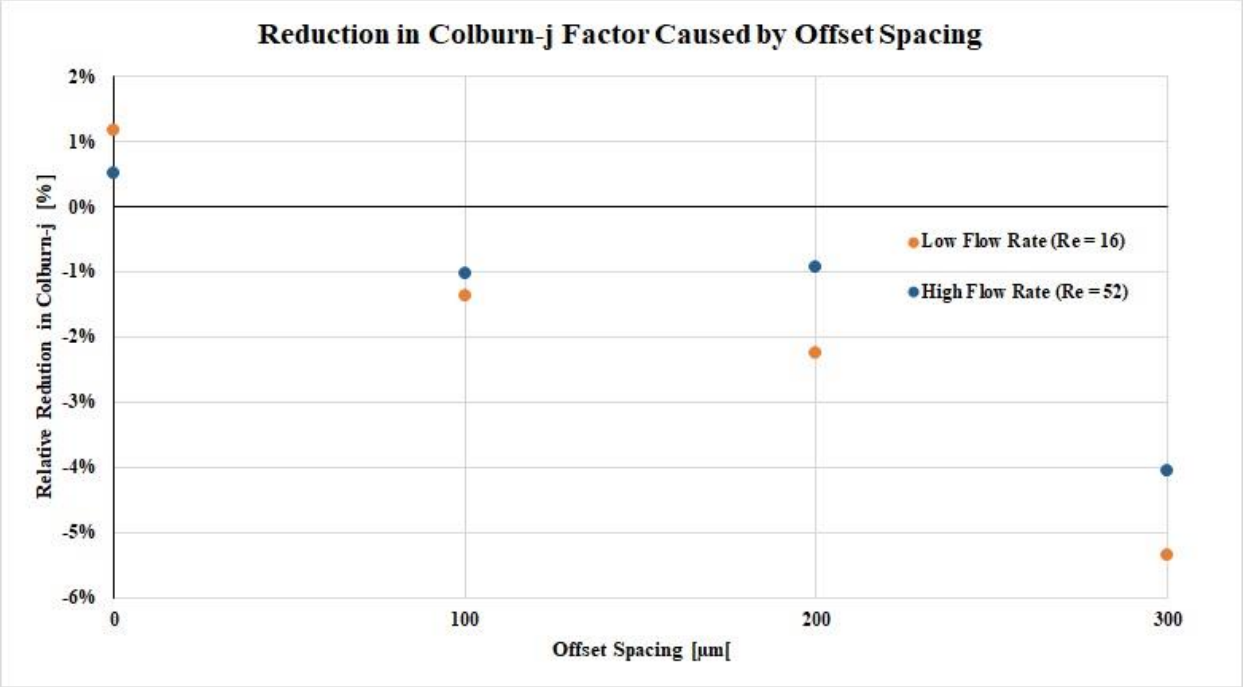

Figure 54: Reduction in *j* Caused by Offset Spacing vs Simulation of Proprietary Geometry

5.1.4 Dimensionless Thermal Resistance Performance

As introduced in Chapter 2, dimensionless thermal resistance was also used to provide an additional metric for evaluating fin arrays. Dimensionless thermal resistance is given as the sum of the convective and capacitive resistances and should be minimized in a "good design."

$$\Theta = \frac{\Delta T_{max}}{\frac{\dot{q_{in}}}{k_f W}} = \frac{k_f W}{\bar{h} A_s} + \frac{k_f W}{\dot{m} c_p} \tag{30}$$

By directly utilizing the surface area available for heat transfer in the convective resistance term, changes in surface area are directly represented in the results seen. Similar to the plots created to show the effects of fin offset spacing on f_{app} and j, the relative difference in dimensionless thermal resistance between the novel rectangular fin arrays and the proprietary geometry was calculated using equation (31). Using this equation, a negative difference suggests a design with a higher thermal resistance compared to the proprietary geometry.

$$\Theta_{\%Diff} = \frac{\Theta_{Proprietary} - \Theta_{Novel}}{\Theta_{Proprietary}} \tag{31}$$

5.1.5 Comparing Fin Arrays

Using the ratio of thermal performance to hydraulic performance proposed by Kays and London to compare the fin arrays it is possible to reconcile decreases in thermal performance with increases in hydraulic performance [3]. Thus the larger the j/f_{app} ratio, indicates greater heat-transfer performance to lower pressure loss expenditure. The ratio of j/f_{app} was compared against the ratio of surface area available for heat transfer (SA_r) in ***Figure 55***.

From this figure, the fin arrays with the largest offset distance between columns of fins performed the best, resulting in a 20% increase in j/f_{app} for the 200µm-300µm fin array. These results are caused by the large reduction in f_{app} and a relatively small change in j.

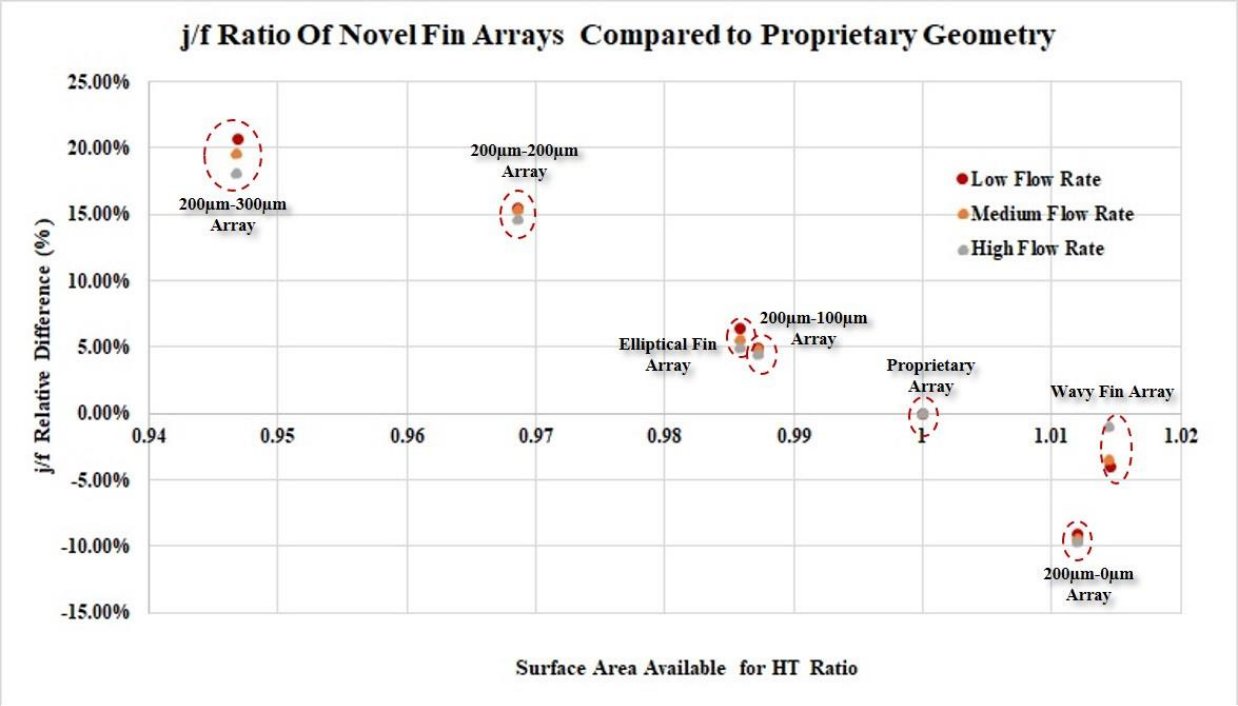

Figure 55: Comparison of Novel Array Designs Using j/f Obtained From Simulation Results

When $\Theta_{\%Diff}$ was utilized to show the relative improvement in Θ over the proprietary geometry in ***Figure 56***, a trend opposite to what was seen in ***Figure 55*** occurs. In this plot, additional offset spacing has a negative effect of thermal resistance by decreasing the surface area available for heat transfer. Utilization of dimensionless thermal resistance suggests that the best design is the wavy fin array. This design reduced thermal resistance by 15%-25% by increasing the surface area available for heat transfer.

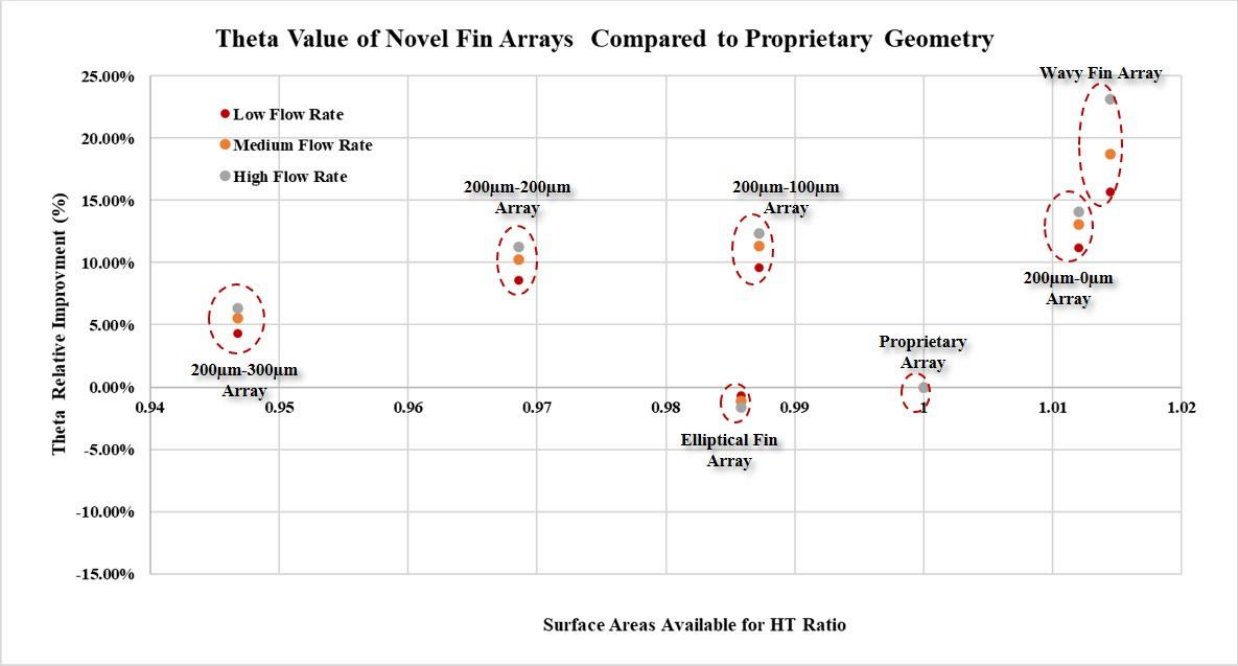

Figure 56: Comparison of Novel Array Designs Using θ Obtained From Simulation Results

However, since all simulations were performed using a constant inlet velocity ($V_{inlet} = constant$), the capacitive resistance for each fin array is the same; and thus, only changes to convective resistance were reflected in the results.

$$\Theta = \frac{\Delta T}{\frac{q_{in}}{k_f * W}} = \frac{k_f W}{\bar{h} A_s} + \frac{k_f W}{\dot{m} c_p}$$

Capacitive Resistance

Convective Resistance

Figure 57: Breakdown of Dimensionless Thermal Resistance

To circumvent this issue, the pressure loss across each array was set to a constant value in Fluent, and the mass flow rate through the array was then solved. Under these conditions, each fin array will experience a unique mass flow rate for the defined pressure difference between the inlet and outlet of the fin array, and the solved mass flow rate can be used in the capacitive resistance term.

However, setting constant pressure boundary condition in Fluent is less stable than utilizing constant velocity conditions. To help with simulation stability, both the Pressure and Momentum Explicit Relaxation Factors were slightly under relaxed, trading simulation time for a more stable convergence. The j/f_{app} ratio and $\Theta_{\%Diff}$ for only the rectangular fin arrays was re-calculated using constant pressure boundary conditions, and the results were compared to those seen in ***Figure 55*** and ***Figure 56***.

In ***Figure 58***, which compares the rectangular fin arrays using j/f_{app}, both simulation methods result in the same trend where increasing the offset distance between fin columns improves the j/f_{app} ratio. The 200µm-300µm array again shows a 15-20% improvement in j/f_{app} over the proprietary array using both constant mass flow rate and constant pressure loss simulations

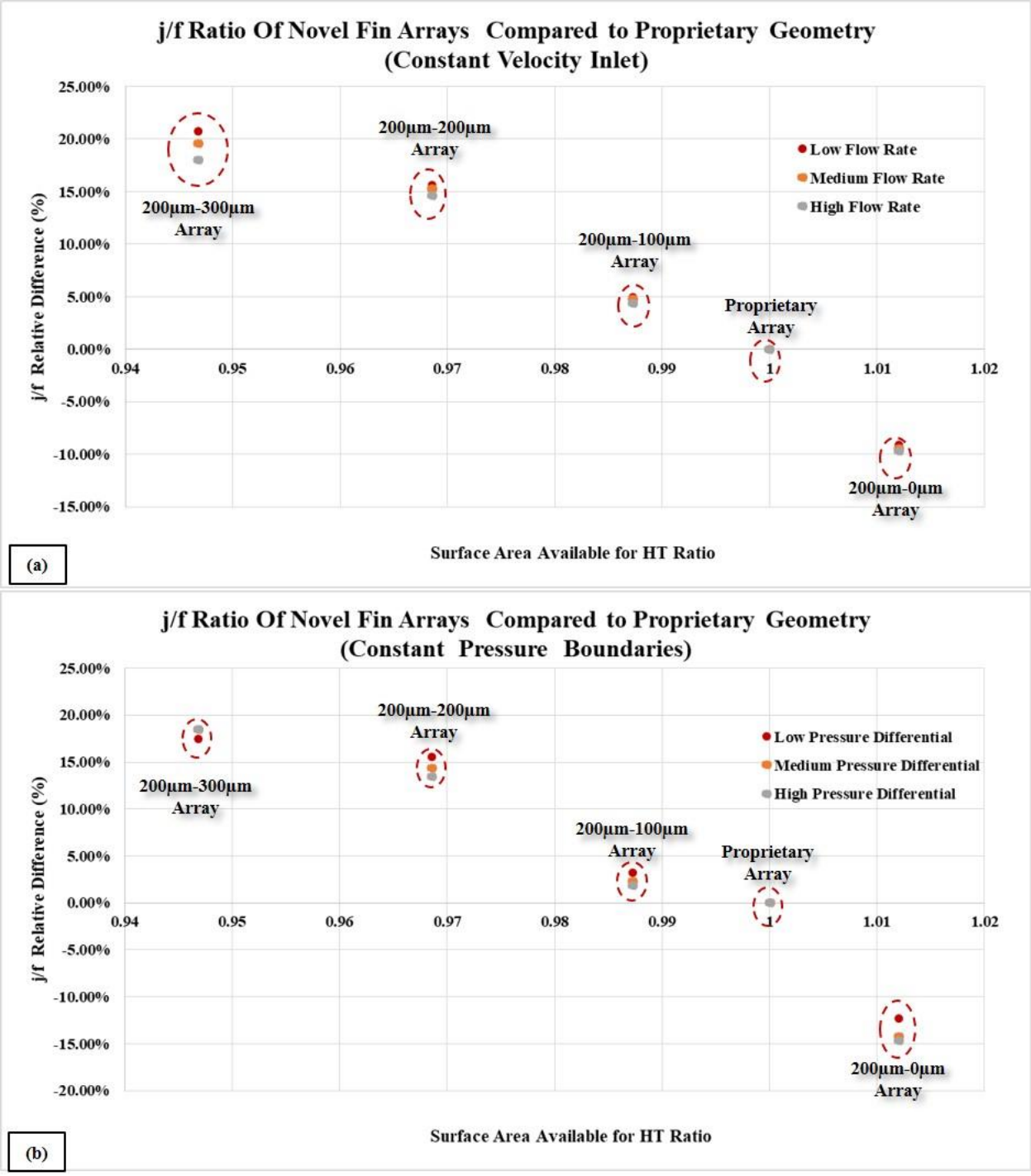

Figure 58: Comparison of j/f_{app} using (a) Constant Velocity Boundary and (b) Constant Pressure Differential Boundary

Figure 59 compares the results of $\Theta_{\%Diff}$ calculated from constant pressure and constant flow rate simulations. Unlike ***Figure 58***, some disagreement between the two graphs occurs. From the plot of ***Figure 59***(b), utilization of constant pressure boundary conditions results in a maximum $\Theta_{\%Diff}$ occurring at the 200µm-200µm array. This suggests that there is some optimal offset distance which minimizes the thermal resistance of the rectangular fin arrays.

Although both rating criteria have their own benefits and shortcomings, owing to the fact that the field application of the actual cold plate will have a fixed flow rate, the use of j/f_{app} ratio as the predominant ranking criteria is suggested. The use of this rating criteria suggests that designs with higher fin offset spacing perform best by their ability to dramatically reduce pressure loss with only a minimal negative effect on thermal performance. Results of the simulations indicate a 20% increase in j/f_{app} for the 200µm-300µm fin array**.**

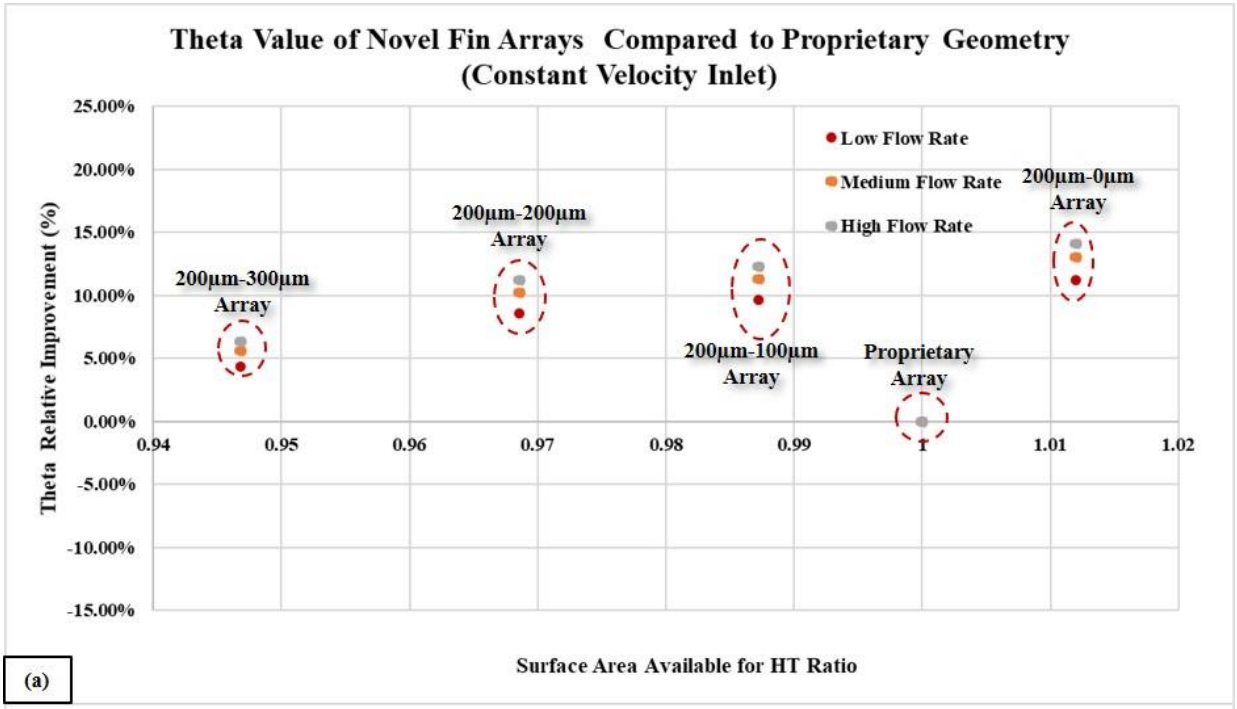

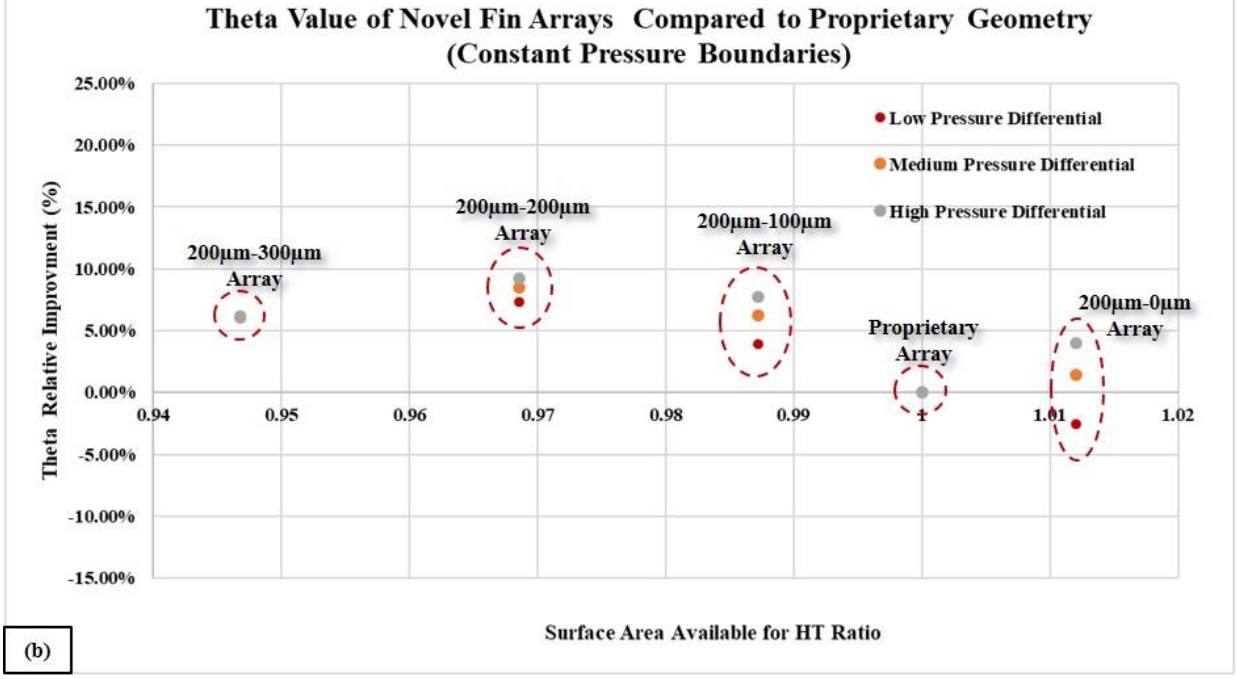

Figure 59: Comparison of $\Theta_{\%Diff}$ using Const. Velocity vs. Const. Pressure Boundary Conditions (a) Constant Velocity Boundary (b) Constant Pressure Differential Boundaries

5.2 Experimental Results

Pressure loss experiments utilizing the four manufactured cold plates listed in **Table 8** were performed using WEG as the working fluid in the experimental set-up described in **Ch. 2**. In the experiments performed, volumetric flow rate through the cold plate was held constant in 1 hour increments to ensure the measured pressure loss reached a steady state value. The average pressure loss over each 1-hour increment was then used in equation (7) to calculate f_{app} for each cold plate. The average fin thickness and fin offset spacing obtained from CT data, provided in ***Table 8***, were used when calculating f_{app} for each cold plate. The values of f_{app} obtained by experimentation were then compared to those values obtained by numerical simulation. The relative difference between numerical and experimental results was then calculated using equation (32).

$$Difference_{f_{app}} = \frac{f_{app-numerical} - f_{app-experiemtnal}}{f_{app-numerical}} \tag{32}$$

Experimental uncertainty analysis was performed utilizing a Taylor Series Method (TSM) of analysis [30]. In this analysis the individual uncertainties associated with flow sensor uncertainty, pressure sensor uncertainty, standard deviation ($\sigma_{\Delta P}$) in pressure readings, standard deviation ($\sigma_{\mathrm{D_h}}$) in hydraulic diameter measurements, standard deviation (σ_L) in the length of the cold plate measurement, and standard deviation (σ_ρ) in fluid density calculations are multiplied by the partial derivative of the apparent Fanning friction factor equation with respect to the relevant variable. The method for determining experimental uncertainty is provided in **Appendix B**.

The uncertainty for both $Re_{channel}$ and f_{app} values was calculated as a percentage of the mean $Re_{channel}$ and f_{app} values. The average of these percent uncertainty values is provided in **Table 10** for each of the printed cold plates.

Table 10: Average Uncertainty for each Manufactured Cold Plate

Cold Plate	Average Percent Uncertainty of $Re_{channel}$	Average Percent Uncertainty of f_{app}
200µm-0µm-BPV6	1.9%	2.2%
200µm-0µm-BPV8	2.1%	2.5%
200µm-100µm-BPV8	3.0%	3.3%
200µm-200µm-BPV8	1.7%	2.0%

From this table, all uncertainly values are below 5% with the greatest uncertainty present in the 200µm-100µm-BPV8 cold plate. From the data presented in **Table 8**, the 200µm-100µm-BPV8 cold plate has the highest variance in fin thickness. This variance is reflected in the calculation of hydraulic diameter, and was the most influential component in uncertainty calculations for both f_{app} and $Re_{channel}$ such that small changes in the hydraulic diameter resulted in large changes to $Re_{channel}$ and f_{app}. This can be seen in the sample calculations provided in **Appendix B**.

Figure 60 plots the experimentally calculated values of f_{app} against the numerical predictions for flow through the 200µm-0µm-BPV6 cold plate, which was printed in the angled orientation. The calculated f_{app} across the cold plate was measured to be 46% above the numerical predictions.

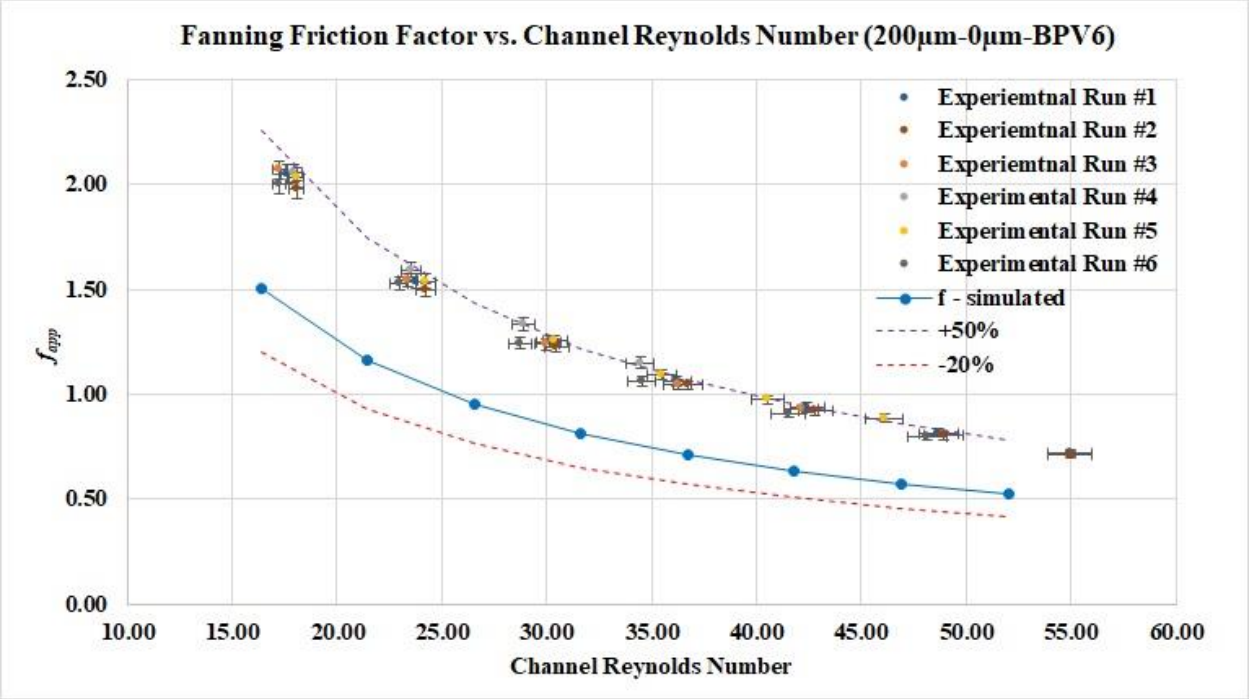

Figure 60: Experimental Pressure Loss in 200µm-0µm-BPV6 Cold Plate (Angled Print Orientation)

Conversely, experiments involving the 200µm-0µm-BPV8 cold plate, which was printed in the horizontal orientation, resulted in only a 34% disagreement in f_{app} with simulation predictions. Shown in **Figure 61**, printing in the horizontal orientation resulted in f_{app} values 12% lower than its counterpart printed in the angled orientation

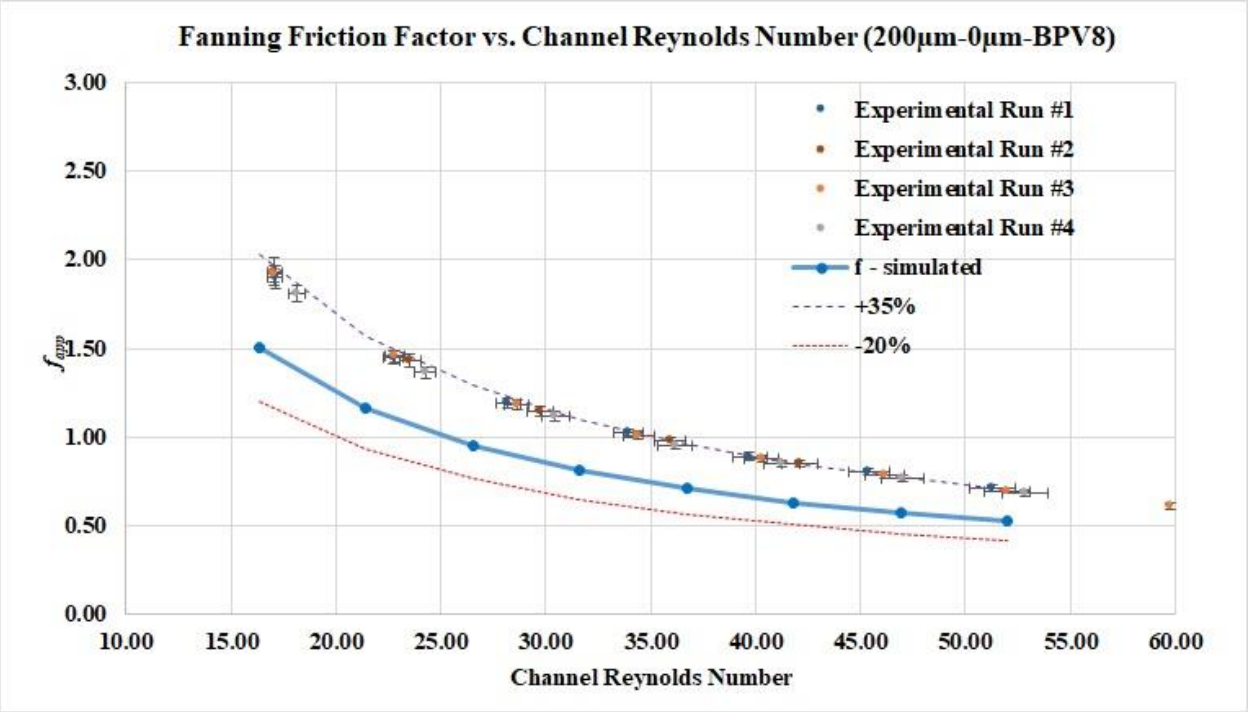

Figure 61: Experimental Pressure Loss in 200µm-0µm-BPV8 Cold Plate (Horizontal Print Orientation)

Figure 62 and **Figure 63** show the results of experimentation involving the 200µm-100µm and 200µm-200µm cold plate respectively. Similar to the performance of the 200µm-0µm-BPV8 cold plate, the 200µm-100µm cold plate performed 44% above numerical predictions.

However, the 200µm-200µm cold plate was found to have f_{app} values very near simulation predictions with only a 3% disagreement despite being printed in the same orientation as the 200µm-100µm cold plate. This sudden drop in f_{app} is caused by the much thicker fins found in the 200µm-200µm cold plate, which greatly reduces hydraulic diameters and increases mean fluid velocity in the channel. Both of these effects combine to greatly reduce the calculated value of f_{app} which can be seen in equation (7).

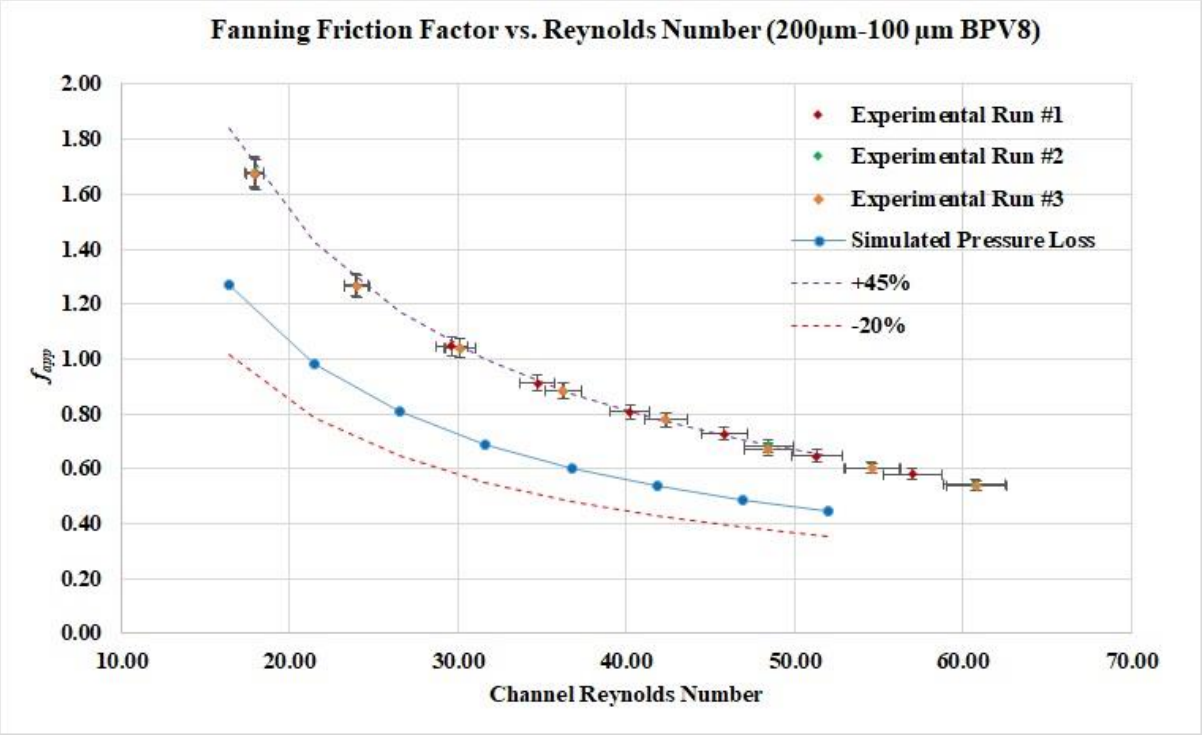

Figure 62: Experimental Pressure Loss in 200µm-100µm-BPV8 Cold Plate (Angled Print Orientation)

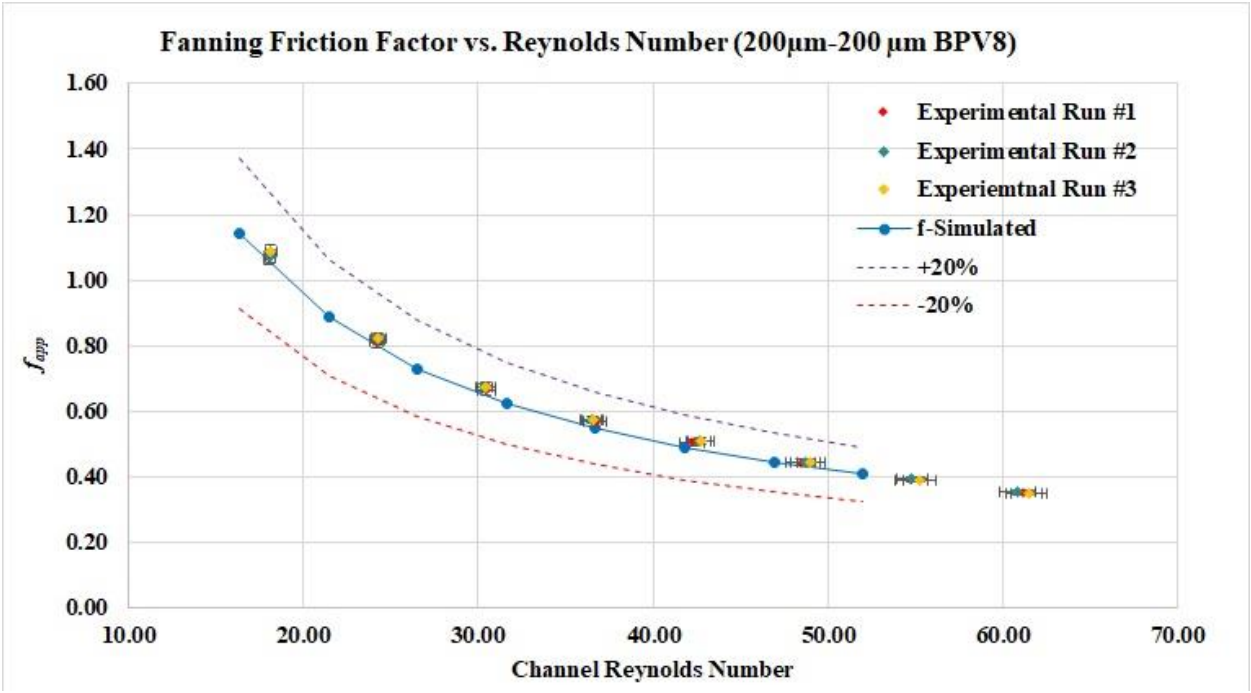

Figure 63: Experimental Pressure Loss in 200µm-200µm-BPV8 Cold Plate (Angled Print Orientation)

When the experimental and simulation results were compared for each cold plate tested in **Figure *64***, print orientation can be seen to have some effect on effect on the value of f_{app}. Printing in the horizontal orientation reduced f_{app} by 12% as compared to the same cold plate geometry printed in the angled orientation. From the information provided in **Table 8**, it can be seen that fins printed in the horizontal orientation, 200µm-0µm-BPV8 cold plate, are slightly thinner than fins printed in the angled orientation, 200µm-0µm-BPV6cold plate. Thinner fins prove beneficial in decreasing pressure loss by reducing form drag on each fin.

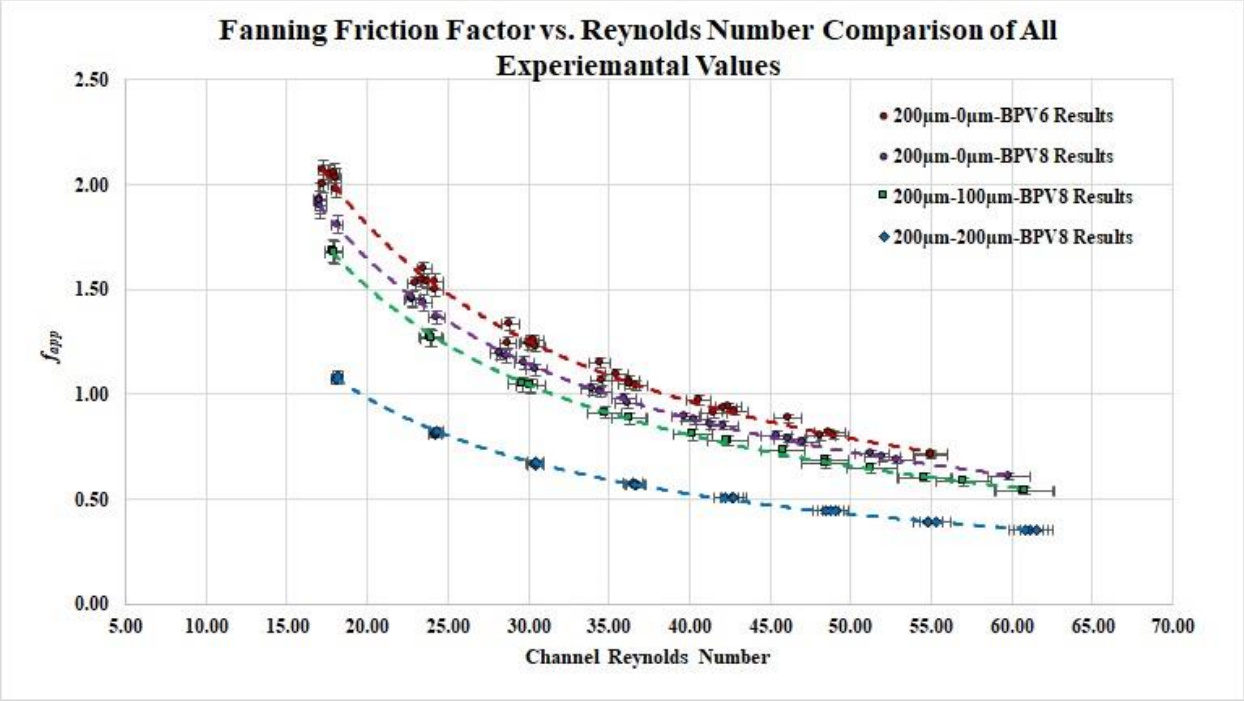

Figure 64: Comparison of Experimental Results from All Cold Plates

Power curve fits of the form shown in equation (33) below were generated for each cold plate shown in **Figure 64**, and can be used to predict the pressure loss at a known channel Reynolds number. The values of the constants used in equation (33) are provided in **Table 11**.

$$f_{app} = A(Re_{channel})^{E} \quad (33)$$

Table 11: Constant Values for Each Cold Plate Geometry

Cold Plate	A	E
200µm-0µm-BPV6	27.1	-0.904
200µm-0µm-BPV8	24.2	-0.898
200µm-100µm-BPV8	23.1	-0.909
200µm-200µm-BPV8	14.8	-0.907

The relative difference between simulation predictions and experimental results is summarized in ***Table 12***. For all experiments performed, higher than anticipated pressure loss was recorded across the AM cold plates. This result was not unexpected. The increased surface roughness of AM parts has been shown to have a negative impact on hydraulic performance [13, 14, 17, 18]. Print orientation was found to have an effect on pressure loss across the cold plates. Both the 200µm-0µm-BPV6 and 200µm-0µm-BPV8 cold plates possessed the same designed fin structure but were manufactured in different print orientations. Printing in the horizontal orientation, 200µm-0µm-BPV8, produced slightly thinner fins which were closer to the designed fin thickness. These thinner fins prove beneficial in decreasing pressure loss across the cold plate.

Table 12: Constant Values for Each Cold Plate Geometry

Cold Plate	Relative Difference
200µm-0µm-BPV6	46%
200µm-0µm-BPV8	34%
200µm-100µm-BPV8	44%
200µm-200µm-BPV8	3%

Chapter 6: Discussion & Conclusions

Over the course of this study the thermal and hydraulic performance of compact AM cold plates with novel fin array designs was investigated utilizing both numerical and experimental procedures. An experimental test apparatus was designed to collected thermal and pressure loss data across the manufactured cold plates utilizing either WEG or PAO as the working fluid.

From the simulations performed in ANSYS Fluent, both the apparent Fanning Friction and Colburn-j factors were calculated and compared to a proprietary geometry provided. The addition of a small distance between subsequent columns of rectangular fins had a significant impact on reducing the simulated pressure loss across the fin array. A 15% reduction in f_{app} was seen when offset distance was increased from 0µm to 100µm. However, this benefit to the hydraulic performance diminished with increasing offset distance such that the improvement seen when increasing offset distance from 200µm to 300µm was only 5%.

To compare and rank the thermal and hydraulic performance of each novel fin array design using a standardized rating criteria, both j/f_{app} and Θ were utilized and conflicting conclusions were reached. From the results of j/f_{app}, the arrays with the largest offset distances performed the best by their ability to greatly reduce pressure loss across the array, whereas arrays that did not sacrifice area available for heat transfer yielded better Θ values. It was decided that that under the constant mass flow rate conditions specified in the Statement of Work, j/f_{app} provided the most

relevant rating criteria. As such, the 200µm-300µm fin array had the best performance, increasing j/f_{app} by ~20% over the proprietary array.

Although, the measured pressure loss across each of the cold plates was much larger than anticipated by numerical simulations, with a 48% increase in the case of the 200µm-0µm-BPV6 cold plate. The higher than anticipated pressure loss across each of the AM cold plates was not unexpected.

The main finding of the study discussed above was summarized below:

- Several compact cold plates were printed from AlSi10Mg metal powder using an L-PBF Additive Manufacturing process. Of the print orientations tested, the most successful printing results were obtained when cold plate were printed at a 45° angle from the substrate.
- Using ANSYS fluent, the effect of adding a small gap between subsequent columns of fins in a rectangular strip fin array was examined. This gap greatly reduced pressure loss across the fin array; however, the benefit of adding additional offset spacing diminished with increasing offset distance.
- Utilizing the ratio of j/f_{app} obtain via numerical simulation, each of the designed novel fin arrays was compared to a baseline proprietary geometry. Of the novel designs simulated, the 200µm-300µm array performed the best, resulting in a 20% improvement in j/f_{app}.

- From the experiments performed, measured Fanning friction factor across each of the cold plates was between 3%-46% above simulation predictions.
- Print orientation was found to have an effect on pressure loss across the 200µm-0µm cold plate, reducing pressure loss by 12% when printed in the horizontal orientation.
- After x-ray CT scans were performed on each cold plate, it was discovered that both the 200µm-100µm and 200µm-200µm cold plates possessed the nearly identical offset distances for a currently unknown reason. This highlights the need for non-destructive evaluation and quality control of AM parts.

Future work on this project should continue the experimental analysis of the AM cold plates by including analysis of the thermal performance of each design. Additionally, full size test coupons of each wavy fin structures, which showed great promise in numerical simulations, should be printed. Additive Manufacturing offers great flexibility when designing novel heat removal devices to meet the ever growing requirements of electronic thermal management; however, as has been illustrated in this study, more research is needed to further examine the printing and performance of these cold plates and heat exchangers.

Chapter 7: References

[1] F. P. Incropera and D. P. DeWitt, *Fundamentals of Heat and Mass Transfer 4th Edition*

[2] R. K. Shah and A. L. London, *Laminar Flow Forced Convection in Ducts*. New York: Accademic Press Inc, 1978.

[3] W. M. Kays and A. L. London *Compact Heat Exchangers*. McGraw-Hill Inc, 1984.

[4] R. M. Manglik and A. E. Bergles, "Heat transfer and pressure drop correlations for the rectangular offset strip fin compact heat exchanger," *Experimental Thermal and Fluid Science*, vol. 10, no. 2, pp. 171-180, 1995/02/01/ 1995, doi: https://doi.org/10.1016/0894-1777(94)00096-Q.

[5] S. Kakac, R. K. Shah, and A. E. Bergles, *Low Reynolds Number Flow Heat Exchangers* Hemisphere Publishign Corporation 1983.

[6] S. M. Thompson, L. Bian, N. Shamsaei, and A. Yadollahi, "An overview of Direct Laser Deposition for additive manufacturing; Part I: Transport phenomena, modeling and diagnostics," *Additive Manufacturing*, vol. 8, pp. 36-62, 2015/10/01/ 2015, doi: https://doi.org/10.1016/j.addma.2015.07.001.

[7] J. Kranz, D. Herzog, and C. Emmelmann, "Design guidelines for laser additive manufacturing of lightweight structures in TiAl6V4," *Journal of Laser Applications*, vol. 27, no. S1, 2015, doi: 10.2351/1.4885235.

[8] R. Konečná, G. Nicoletto, S. Fintová, and M. Frkáň, "As-built surface layer characterization and fatigue behavior of DMLS Ti6Al4V," *Procedia Structural Integrity*, vol. 7, pp. 92-100, 2017/01/01/ 2017, doi: https://doi.org/10.1016/j.prostr.2017.11.065.

[9] A. Kover. "Transformation In 3D: How A Walnut-Sized Part Changed The Way GE Aviation Builds Jet Engines." https://www.ge.com/news/reports/transformation-3d-walnut-sized-part-changed-way-ge-aviation-builds-jet-engines (accessed August 23, 2021).

[10] N. C. DeJong, L. W. Zhang, A. M. Jacobi, S. Balachandar, and D. K. Tafti, "A Complementary Experimental and Numerical Study of the Flow and Heat Transfer in Offset Strip-Fin Heat Exchangers," *Journal of Heat Transfer*, vol. 120, no. 3, pp. 690-698, 1998, doi: 10.1115/1.2824338.

[11] H. M. Joshi and R. L. Webb, "Heat transfer and friction in the offset stripfin heat exchanger," *International Journal of Heat and Mass Transfer*, vol. 30, no. 1, pp. 69-84, 1987/01/01/ 1987, doi: https://doi.org/10.1016/0017-9310(87)90061-5.

[12] M. C. William Kays, Bernhard Weigand, *Convective Heat Transfer* (McGraw-Hill series in Mechanical Engineering). McGraw-Hill 2005.

[13] M. Wong, I. Owen, C. J. Sutcliffe, and A. Puri, "Convective heat transfer and pressure losses across novel heat sinks fabricated by Selective Laser Melting," *International Journal of Heat and Mass Transfer*, vol. 52, no. 1-2, pp. 281-288, 2009, doi: 10.1016/j.ijheatmasstransfer.2008.06.002.

[14] J. Kuehndel, B. Kerler, and C. Karcher, "Selective laser melting in heat exchanger development - experimental investigation of heat transfer and pressure drop

characteristics of wavy fins," *Heat and Mass Transfer*, vol. 54, no. 8, pp. 2187-2193, 2018/08/01 2018, doi: 10.1007/s00231-018-2352-0.
[15] M. Khoshvaght-Aliabadi, M. Samani, F. Hormozi, and A. Asl, "3D-CFD simulation and neural network model for the j and f factors of the wavy fin-and-flat tube heat exchangers," *Brazilian Journal of Chemical Engineering*, vol. 28, pp. 505-520, 09/01 2011, doi: 10.1590/S0104-66322011000300016.
[16] M. A. Y. S. Muzychka, "MODELS FOR PRESSURE DROP AND HEAT TRANSFER IN AIR COOLED COMPACT WAVY FIN HEAT EXCHANGERS," *Journal of Enhanced Heat Transfer*, vol. 18, no. 3, pp. 191-207, 2011.
[17] D. J. Saltzman *et al.*, "Experimental comparison of a traditionally built versus additively manufactured aircraft heat exchanger," presented at the 55th AIAA Aerospace Sciences Meeting, 2017.
[18] C. K. Stimpson, J. C. Snyder, K. A. Thole, and D. Mongillo, "Roughness Effects on Flow and Heat Transfer for Additively Manufactured Channels," *Journal of Turbomachinery*, vol. 138, no. 5, 2016, doi: 10.1115/1.4032167.
[19] D. C. Company, "DOWTHERMTM SR-1 Fluid Technical Data Sheet," 180-01312-0417 [Online]. Available: https://www.dow.com/en-us/pdp.dowtherm-sr-1-heat-transfer-fluid-dyed.25630z.html
[20] D. Tuckerman and R. Pease, "High-performance heat sinking for VLSI," *IEEE Electron Device Letters*, vol. 2, pp. 126-129, 1981.
[21] R. W. Knight, D. J. Hall, J. S. Goodling, and R. C. Jaeger, "Heat sink optimization with application to microchannels," *IEEE Transactions on Components, Hybrids, and Manufacturing Technology*, vol. 15, no. 5, pp. 832-842, 1992, doi: 10.1109/33.180049.
[22] W. D. G. Pahl, J. Feldhusen, K-H Grote, *Engineering Design: A Systematic Appraoch* 3rd ed. Springer-Verlag London 2007.
[23] *Parker O-Ring Handbook*, 50th Anniversary Edition ed.: Parker Hannifin Corporation, 2021, p. 292.
[24] J. Rinker. "P&IDs (Piping & Instrumentation Diagrams) and P&ID Valve Symbol Library." Assured Automation. (accessed 2021).
[25] *Ultrapure Fluid Handling Integrated Flow Controller Series Brochure*. (2014). www.levitronix.com: Levitronix.
[26] B. Corporation, "Kodiak Recirculating Chiller Technical Manual," 2019.
[27] "Spatial Discretization." ANSYS Inc. https://www.afs.enea.it/project/neptunius/docs/fluent/html/th/node366.htm (accessed 9/15, 2021).
[28] J. P. Oliveira, A. D. LaLonde, and J. Ma, "Processing parameters in laser powder bed fusion metal additive manufacturing," *Materials & Design*, vol. 193, p. 108762, 2020/08/01/ 2020, doi: https://doi.org/10.1016/j.matdes.2020.108762.
[29] A. Yadollahi and N. Shamsaei, "Additive manufacturing of fatigue resistant materials: Challenges and opportunities," *International Journal of Fatigue*, vol. 98, pp. 14-31, 2017/05/01/ 2017, doi: https://doi.org/10.1016/j.ijfatigue.2017.01.001.
[30] H. W. C. W. G. Steele, *Experimental Validation, and Uncertainty Analysis for Engineers* 3rd ed. John Wiley & Sons, 2009.

Appendix A: Conversion of PAO to DOW Therm SR1

Constants: PAO Thermophysical Properties taken at (15°C)

The thermophysical properties of PAO were calculated at the inlet temperature specified in the SOW (15°C).

$$\rho = 797.753\ \frac{kg}{m^3}$$

$$\mu = 0.00863 \frac{N * s}{m^2}$$

$$C_p = 2181.323 \frac{J}{kg * k}$$

$$k = 0.144 \frac{W}{m * K}$$

Mass Flow Rate Conversions:

The mass flow rate specified by in the SOW is converted to SI units.

$$\dot{m}_{L3} = [1.5 : 5]\ \frac{lbm}{min}$$

$$\dot{m}_{SI} = [1.5 : 5]\ \frac{lbm}{min} * 0.00755987 \frac{\frac{kg}{s}}{\frac{lbm}{min}} = [0.0113 : 0.0378] \frac{kg}{s}$$

Flow in Pipe Conversions:

Finding the volumetric flow rate range for the PAO.

$$\dot{m}_{SI} = \rho * V * A_c$$

$$\dot{V}_{GPM} = \frac{\dot{m}_{SI}}{\rho} = \frac{[0.0113 : 0.0378]\frac{kg}{s}}{797.753\frac{kg}{m^3}} * 15850.372\frac{GPM}{\frac{m^3}{s}} = [0.2253 : 0.751]\ GPM$$

$$\dot{V}_{GPM} \cong [0.2253 : 0.751]\ GPM * \frac{3.785\ LPM}{1\ GPM} \cong [0.85 : 2.843]\ LPM$$

Finding Reynolds Number for flow through the pipe. ID = 0.5" and OD = 0.75"

$$Re_{pipe} = \frac{4 * \dot{m}_{SI}}{\mu * \pi * ID} = \frac{4 * [0.0113 : 0.0378]\frac{kg}{s}}{0.00863\frac{N * s}{m^2} * \pi * \left(0.5\ in * 0.0254\frac{m}{in}\right)} = [131.3 : 439.1]$$

Beginning conversions to DOW Therm SR1 at 15°C:

Constants:

$\rho = 1076.4\frac{kg}{m^3}$

$\mu = 0.00497\frac{N * s}{m^2}$

Conversion of Re values:

Reynolds number for PAO and DOW Therm SR1 is being set equal in the pipe:

$$Re_{pao} = Re_{DOW}$$

$$Re_{pao} = \frac{\rho * u_m * D_h}{\mu}\Big|_{DOW}$$

$$Re_{pao} * \frac{\mu}{\rho * D_h}\Big|_{DOW} = u_m$$

The mean velocity of the DOW Them SR1 in the ½" ID pipe is:

$$u_m = Re_{pao} * \left(\frac{\mu}{\rho * D_h}\right)_{DOW} = [527 : 1756.5] * \left(\frac{0.00497 \frac{N * s}{m^2}}{1076.4 \frac{kg}{m^3} * \left(0.5\ in * 0.0254 \frac{m}{in}\right)}\right)$$

$$u_m = [0.0478 : 0.160]\ m/s$$

$$Re_{DOW} = [131.3 : 439.1]$$

The volumetric flow rate in the pipe is:

$$\dot{V}_{DOW} = u_m * \frac{\pi}{4} * ID^2 = [0.0478 : 0.160] \frac{m}{s} * \frac{\pi}{4} * \left(0.5\ in * 0.0254 \frac{m}{in}\right)^2$$

$$= [6.0613 :\ 20.204] E^{-6} \frac{m^3}{s}$$

$$\dot{V}_{DOW} = [6.0613 :\ 20.204] E^{-6} \frac{m^3}{s} *\ 15850 \frac{GPM}{\frac{m^3}{s}} = [\ 0.0961 : 0.3202]\ GPM$$

$$\dot{V}_{DOW} = [\ 0.0961 : 0.3202]\ GPM * \frac{3785\ mLPM}{1\ GPM} \cong [363.6 : 1212.1]\ mLPM$$

The mass flow rate of DOW Therm SR1 is:

$$\dot{m}_{DOW} = \rho_{DOW} * \dot{V}_{DOW}$$

$$\dot{m}_{DOW} = 1076.4\frac{kg}{m^3} * [6.0613 : 2.0204]E^{-6}\frac{m^3}{s} = [0.0065 : 0.0217]\frac{kg}{s}$$

$$\dot{m}_{DOW} = [0.0065 : 0.0217]\frac{kg}{s} * \frac{1}{0.00756}\frac{\frac{lbm}{min}}{\frac{kg}{s}} = [0.863 : 2.877]\frac{lbm}{min}$$

Velocity at Manifold Inlet

The velocity of DOW Therm SR1 coming in the manifold is calculated below.

$$V_{manifold,inlet} = \frac{\dot{m}_{SI}}{\rho * A_{c-manifold}} = \frac{[0.0065 : 0.0217]\frac{kg}{s}}{1076.4\ \frac{kg}{m^3} * \frac{\pi}{4}\left(0.180\ in * 0.0254\frac{m}{in}\right)^2}$$

$$= [\ 0.369 :\ 1.231]\frac{m}{s}$$

Velocity at manifold exit:

Once the DOW Therm SR1 exits into the manifold from the tubing it will spread out, losing fluid velocity. The dimensions at the Manifold Outlet are: L = 2" H = 0.1"

For the same mass flow rate, the fluid velocity at the manifold exit becomes:

$$V_{manifold,exit} = \frac{\dot{m}_{SI}}{\rho A_{c-manifold}} = \frac{[0.0065 : 0.0217]\frac{kg}{s}}{1076.4\ \frac{kg}{m^3}\left(2\ in * 0.1in * 0.00064516\frac{m^2}{in^2}\right)}$$

$$= [\ 0.0470 :\ 0.157]\frac{m}{s}$$

Estimated Re at Manifold Exit:

$$Re_{manifold,exit} = \frac{\rho V_{manifold,exit} D_{h-manifold}}{\mu}$$

$$Re_{manifold,exitl} = \frac{1076.4\ \frac{kg}{m^3}[\ 0.0470 :\ 0.157]\frac{m}{s}\ 0.004838\ m}{0.00497\frac{Ns}{m^2}} = [49.3 : 164.2]$$

Velocity in channel:

The mean velocity in the flow channels within the cold plate can be found be a simple continuity expression between the velocity at the manifold exit and the ratio of cross sectional areas between the area of fluid entering a single channel from the manifold and the area inside the channel.

$$u_{m-channel} = V_{manifold,exit}\frac{A_{c-manifold}}{A_{c-channel}}$$

$$u_{m-channel} = \left[\ 0.0470 :\ 0.157\frac{m}{s}\right]\left(\frac{2.687\ E^{-6}\ m^2}{2.179E^{-6}\ m^2}\right)$$

$$u_{m-channel} = \frac{[0.0580 : 0.194]m}{s}$$

The estimated Re in channel can then be found by:

$$Re_{channel} = \frac{\rho u_{m-channel} D_{h-channel}}{\mu}$$

$$Re_{channel} = \frac{1076.4\ \frac{kg}{m^3}[\ 0.0580 : 0.194]\frac{m}{s}\ 0.001216\ m}{0.00497\frac{Ns}{m^2}} = [15.3 : 51.1]$$

Appendix B: Uncertainty Analysis

Experimental uncertainty analysis was performed utilizing a Taylor Series Method (TSM) of analysis [30]. In this analysis the individual uncertainties associated with flow sensor uncertainty, pressure sensor uncertainty, standard deviation ($\sigma_{\Delta P}$) in pressure readings, standard deviation (σ_{D_h}) in hydraulic diameter measurements, standard deviation (σ_L) in the length of the cold plate measurement, standard deviation (σ_ρ) in fluid density calculations, and standard deviation (σ_μ) in fluid viscosity calculations are multiplied by the partial derivative of the apparent Fanning friction factor equation with respect to the relevant variable.

Due to the large changes in temperature some of the experiments experienced over their long run times, the assumption was made that the error associated with the accuracy of the T-type thermocouples used to measure the fluid temperature was much less than the error contributed by the changing temperature of the working fluid over the course of a long experiment. To calculate the uncertainty associated with changing fluid properties, the mean fluid temperature at each time step was first calculated as the average between the inlet and outlet thermocouples. Then the density and viscosity at each time step was calculated using the mean fluid temperatures and a curve fit equation to the DOW Therm SR1 data sheet. The standard deviation of these density and viscosity calculations, σ_ρ and σ_μ, was used in the following uncertainty analysis.

$$f_{app}\big|_{TSM} = \left(\left(u_{flow\,rate}\right)^2 \left(\frac{\partial f_{app}}{\partial u_m}\right)^2 + (\sigma_{\Delta P})^2 \left(\frac{\partial f_{app}}{\partial \Delta P}\right)^2 + \right.$$

$$\left. \left(u_{pressure}\right)^2 \left(\frac{\partial f_{app}}{\partial \Delta P}\right)^2 + \left(\sigma_{\mathrm{D_h}}\right)^2 \left(\frac{\partial f_{app}}{\partial \mathrm{D_h}}\right) + (\sigma_{\mathrm{L}})^2 \left(\frac{\partial f_{app}}{\partial \mathrm{L}}\right) + \left(\sigma_{\rho}\right)^2 \left(\frac{\partial f_{app}}{\partial \rho}\right) \right)^{\frac{1}{2}}$$

Where:

$$\frac{\partial f_{app}}{\partial u_m} = \frac{1}{4}(\overline{\Delta P}) \left(\frac{\overline{D_h}}{\bar{L}}\right) \left(\frac{-4}{\bar{\rho}(\overline{u_m})^3}\right)$$

$$\frac{\partial f_{app}}{\partial \Delta P} = \frac{1}{4} \left(\frac{\overline{D_h}}{\bar{L}}\right) \left(\frac{2}{\bar{\rho}(\overline{u_m})^2}\right)$$

$$\frac{\partial f_{app}}{\partial \mathrm{D_h}} = \frac{1}{4}(\overline{\Delta P}) \left(\frac{1}{\bar{L}}\right) \left(\frac{2}{\bar{\rho}(\overline{u_m})^2}\right)$$

$$\frac{\partial f_{app}}{\partial L} = \frac{1}{4}(\overline{\Delta P}) \left(-\frac{\overline{D_h}}{\bar{L}^2}\right) \left(\frac{2}{\bar{\rho}(\overline{u_m})^2}\right)$$

$$\frac{\partial f_{app}}{\partial \rho} = \frac{1}{4} \left(\frac{\overline{D_h}}{\bar{L}}\right) \left(\frac{-2}{\bar{\rho}^2(\overline{u_m})^2}\right)$$

The uncertainty in the measured flow rate was found by multiplying the advertised accuracy of the sensor multiplied by the measured volumetric flow rate. This volumetric flow rate must then be converted into a mean channel velocity (u_m) using the process describe in **Appendix A**.

$$u_{flow\,rate} = 1\%(\dot{V}_{measured})$$

Similarly, the uncertainty in the measured pressure loss was found by multiplying the advertised accuracy of the pressure sensor by the measured pressure value.

$$u_{pressure} = 0.8\%(\Delta P_{measured})$$

Much more simplistically, the uncertainty in the channel Reynolds number is calculated from the uncertainty in the flow rate values, standard deviation ($\sigma_{\mathrm{D_h}}$) in hydraulic diameter measurements, standard deviation (σ_{ρ}) in fluid density calculations, and standard deviation (σ_{μ}) in fluid viscosity calculations.

$$Re_{channel}|_{TSM} = \sqrt{\left(u_{flow\ rate}\right)^2\left(\frac{\partial Re}{\partial \mathrm{u_m}}\right)^2 + \left(\sigma_{\mathrm{D_h}}\right)^2\left(\frac{\partial Re}{\partial \mathrm{D_h}}\right)^2 + \left(\sigma_{\mu}\right)^2\left(\frac{\partial Re}{\partial \mu}\right)^2 + \left(\sigma_{\rho}\right)^2\left(\frac{\partial Re}{\partial \rho}\right)^2}$$

Where:

$$\frac{\partial Re}{\partial u_m} = \frac{\bar{\rho}\overline{D_h}}{\bar{\mu}}$$

$$\frac{\partial Re}{\partial D_h} = \frac{\bar{\rho}\overline{u_m}}{\bar{\mu}}$$

$$\frac{\partial Re}{\partial \mu} = -\frac{\bar{\rho}\overline{D_h}\overline{u_m}}{\bar{\mu}^2}$$

$$\frac{\partial Re}{\partial \rho} = \frac{\overline{D_h}\overline{u_m}}{\bar{\mu}}$$

Sample Calculation:

The sample calculation below will be performed using the following data points collected from experiments.

$$\overline{\Delta P} = 716\ Pa$$

$$\overline{u_m} = 0.0610\ \mathrm{m/s}$$

$$\sigma_{\Delta P} = 3.88\ Pa$$

$$\sigma_{D_h} = 2.05 \times 10^{-5}\ m$$

$$\sigma_L = 7.42 \times 10^{-5}\ m$$

$$\sigma_\rho = 3.15 \times 10^{-2}\ \frac{kg}{m^3}$$

$$\sigma_\mu = 7.42 \times 10^{-6}\ \frac{Ns}{m^2}$$

$$\overline{D_h} = 1.17 \times 10^{-3} m$$

$$\bar{L} = 5.097 \times 10^{-2}\ \mathrm{m}$$

$$\bar{\rho} = 1074 \frac{kg}{m^3}$$

$$\bar{\mu} = 0.00433 \frac{Ns}{m^2}$$

First, the value of f_{app} can be calculated using the method below from mean values.

$$f_{app-calculated} = \frac{1}{4}(\overline{\Delta P})\left(\frac{\overline{D_h}}{\bar{L}}\right)\left(\frac{2}{\bar{\rho}(\overline{u_m})^2}\right)$$

$$f_{app-calculated} = \frac{1}{4}(716\ Pa)\left(\frac{1.17 \times 10^{-3} m}{5.097 \times 10^{-2}\ \mathrm{m}}\right)\left(\frac{2}{1074\frac{kg}{m^3}\left(0.0610\frac{\mathrm{m}}{\mathrm{s}}\right)^2}\right)$$

$$f_{app-calculated} = 2.06$$

Solving for the uncertainty in the flow rate:

$$u_{flow\ rate} = 1\%(\dot{V}_{measured})$$

$$u_{flow\ rate} = 0.000362\frac{m}{s}$$

Solving for the uncertainty in the pressure sensor:

$$u_{pressure} = 0.8\%(\Delta P_{measured})$$

$$u_{pressure} = 0.8\%(716\ \mathrm{Pa})$$

$$u_{pressure} = 0.571\ Pa$$

Standard deviation of collected pressure data, density, viscosity, hydraulic diameter, and cold plate length calculations were found using Microsoft Excel.

$$\sigma_{\Delta P} = 3.88\ Pa$$

$$\sigma_{D_h} = 2.05 \times 10^{-5}\ m$$

$$\sigma_{L} = 7.42 \times 10^{-5}\ m$$

$$\sigma_{\rho} = 3.15 \times 10^{-2}\ \frac{kg}{m^3}$$

$$\sigma_{\mu} = 7.42 \times 10^{-6} \frac{Ns}{m^2}$$

Solving for the partial derivative of f_{app} with respect to the mean channel velocity:

$$\frac{\partial f_{app}}{\partial u_m} = \frac{1}{4}(\overline{\Delta P})\left(\frac{\overline{D_h}}{\bar{L}}\right)\left(\frac{-4}{\bar{\rho}(\overline{u_m})^3}\right)$$

$$\frac{\partial f_{app}}{\partial u_m} = \frac{1}{4}(716\ Pa)\left(\frac{1.17 \times 10^{-3} m}{5.097 \times 10^{-2}\ \mathrm{m}}\right)\left(\frac{-4}{1074\frac{kg}{m3}\left(0.0610\frac{\mathrm{m}}{\mathrm{s}}\right)^3}\right)$$

$$\frac{\partial f_{app}}{\partial u_m} = -67.4\left(\frac{m}{s}\right)^{-1}$$

Solving for the partial derivative of f_{app} with respect to the mean pressure change across the cold plate:

$$\frac{\partial f_{app}}{\partial \Delta P} = \frac{1}{4}\left(\frac{\overline{D_h}}{\bar{L}}\right)\left(\frac{2}{\bar{\rho}(\overline{u_m})^2}\right)$$

$$\frac{\partial f_{app}}{\partial \Delta P} = \frac{1}{4}\left(\frac{1.17 \times 10^{-3} m}{5.097 \times 10^{-2}\ \mathrm{m}}\right)\left(\frac{2}{1074\frac{kg}{m3}\left(0.0610\frac{\mathrm{m}}{\mathrm{s}}\right)^3}\right)$$

$$\frac{\partial f_{app}}{\partial \Delta P} = 2.87 \times 10^{-3}\ Pa^{-1}$$

Solving for the partial derivative of f_{app} with respect to the hydraulic diameter of the channel:

$$\frac{\partial f_{app}}{\partial \mathrm{D}_h} = \frac{1}{4}(\overline{\Delta P})\left(\frac{1}{\bar{L}}\right)\left(\frac{2}{\bar{\rho}(\overline{u_m})^2}\right)$$

$$\frac{\partial f_{app}}{\partial \mathrm{D}_h} = \frac{1}{4}(716\ Pa)\left(\frac{1}{5.097 \times 10^{-2}\ \mathrm{m}}\right)\left(\frac{2}{1074\frac{kg}{m^3}\left(0.0610\frac{\mathrm{m}}{\mathrm{s}}\right)^2}\right)$$

$$\frac{\partial f_{app}}{\partial \mathrm{D}_h} = 1760\ m^{-1}$$

Solving for the partial derivative of f_{app} with respect to the length of the cold plate:

$$\frac{\partial f_{app}}{\partial L} = \frac{1}{4}(\overline{\Delta P})\left(-\frac{\overline{D_h}}{\bar{L}^2}\right)\left(\frac{2}{\bar{\rho}(\overline{u_m})^2}\right)$$

$$\frac{\partial f_{app}}{\partial L} = \frac{1}{4}(716\ Pa)\left(-\frac{1.17 \times 10^{-3} m}{(5.097 \times 10^{-2}\ \mathrm{m})^2}\right)\left(\frac{2}{1074\frac{kg}{m^3}\left(0.0610\frac{\mathrm{m}}{\mathrm{s}}\right)^2}\right)$$

$$\frac{\partial f_{app}}{\partial L} = -40.3\ m^{-1}$$

Solving for the partial derivative of f_{app} with respect to the density of the working fluid:

$$\frac{\partial f_{app}}{\partial \rho} = \frac{1}{4}(\overline{\Delta P})\left(\frac{\overline{D_h}}{\bar{L}}\right)\left(\frac{-2}{\bar{\rho}^2(\overline{u_m})^2}\right)$$

$$\frac{\partial f_{app}}{\partial \rho} = \frac{1}{4}(716\ Pa)\left(\frac{1.17 \times 10^{-3} m}{5.097 \times 10^{-2}\ \mathrm{m}}\right)\left(\frac{-2}{\left(1074\frac{kg}{m^3}\right)^2\left(0.0610\frac{\mathrm{m}}{\mathrm{s}}\right)^2}\right)$$

$$\frac{\partial f_{app}}{\partial \rho} = -1.91 \times 10^{-3}\frac{m^3}{kg}$$

Now the total uncertainty in the calculated apparent Fanning friction factor value can be found using the Taylor Series Method.

$$f_{app}\big|_{TSM} = \Bigg(\left(u_{flow\ rate}\right)^2\left(\frac{\partial f_{app}}{\partial u_m}\right)^2 + (\sigma_{\Delta P})^2\left(\frac{\partial f_{app}}{\partial \Delta P}\right)^2 +$$

$$\left(u_{pressure}\right)^2\left(\frac{\partial f_{app}}{\partial \Delta P}\right)^2 + \left(\sigma_{\mathrm{D_h}}\right)^2\left(\frac{\partial f_{app}}{\partial \mathrm{D_h}}\right) + (\sigma_{\mathrm{L}})^2\left(\frac{\partial f_{app}}{\partial \mathrm{L}}\right) + \left(\sigma_{\rho}\right)^2\left(\frac{\partial f_{app}}{\partial \rho}\right)\Bigg)^{\frac{1}{2}}$$

By its components:

$$\left(u_{flow\ rate}\right)^2\left(\frac{\partial f_{app}}{\partial u_m}\right)^2 = \left(0.000362\frac{m}{s}\right)^2\left(67.4\left(\frac{m}{s}\right)^{-1}\right)^2 = 5.95 \times 10^{-4}$$

$$(\sigma_{\Delta P})^2\left(\frac{\partial f_{app}}{\partial \Delta P}\right)^2 = (3.88\ Pa)^2(2.87 \times 10^{-3}\ Pa^{-1})^2 = 1.24 \times 10^{-4}$$

$$\left(u_{pressure}\right)^2\left(\frac{\partial f_{app}}{\partial \Delta P}\right)^2 = (0.571\ Pa)^2(2.87 \times 10^{-3}\ Pa^{-1})^2 = 2.69 \times 10^{-6}$$

$$\left(\sigma_{\mathrm{D_h}}\right)^2\left(\frac{\partial f_{app}}{\partial \mathrm{D_h}}\right) = (2.05 \times 10^{-5}\ m)^2(1760\ m^{-1})^2 = 1.30 \times 10^{-3}$$

$$(\sigma_{\mathrm{L}})^2\left(\frac{\partial f_{app}}{\partial \mathrm{L}}\right) = (7.42\times10^{-5}\,m)^2(-40.3\,m^{-1})^2 = 8.94\times10^{-6}$$

$$(\sigma_{\rho})^2\left(\frac{\partial f_{app}}{\partial \rho}\right) = \left(3.15\times10^{-2}\,\frac{kg}{m^3}\right)^2\left(-1.91\times10^{-3}\,\frac{m^3}{kg}\right)^2 = 3.62\times10^{-9}$$

Reinserting the components into the full equation:

$$f_{app}\big|_{TSM} = \big((5.95\times10^{-4}) + (1.24\times10^{-4}) + (2.69\times10^{-6}) + (1.30\times10^{-3}) + (8.94\times10^{-6}) + (3.62\times10^{-9})\big)^{\frac{1}{2}}$$

$$f_{app}\big|_{TSM} = 0.0451$$

The total uncertainty in the calculated apparent Fanning friction factor can now be calculated as:

$$f_{app} = 2.06 \pm 0.0451$$

The total uncertainty in the calculated channel Reynolds number is calculated in much the same way as the apparent Fanning friction factor. First the channel Reynolds number is calculated from mean properties.

$$Re_{channel} = \frac{\bar{\rho}\overline{D_h}\,\overline{u_m}}{\bar{\mu}} = \frac{\left(1074\,\frac{kg}{m^3}\right)(1.17\times10^{-3}m)\left(0.0610\,\frac{\mathrm{m}}{\mathrm{s}}\right)}{0.00433\,\frac{Ns}{m^2}} = 17.7$$

Now, uncertainty can be calculated using Taylor Series Method.

$$Re_{channel}|_{TSM} = \sqrt{(u_{flow\,rate})^2\left(\frac{\partial Re}{\partial \mathrm{u_m}}\right)^2 + (\sigma_{\mathrm{D_h}})^2\left(\frac{\partial Re}{\partial \mathrm{D_h}}\right)^2 + (\sigma_{\mu})^2\left(\frac{\partial Re}{\partial \mu}\right)^2 + (\sigma_{\rho})^2\left(\frac{\partial Re}{\partial \rho}\right)^2}$$

Where:

$$\frac{\partial Re}{\partial u_m} = \frac{\bar{\rho}\overline{D_h}}{\bar{\mu}} = \frac{\left(1074\,\frac{kg}{m^3}\right)(1.17\times10^{-3}m)}{0.00433\,\frac{Ns}{m^2}} = 290\,\frac{m^{-1}}{s}$$

$$\frac{\partial Re}{\partial D_h} = \frac{\bar{\rho}\overline{u_m}}{\bar{\mu}} = \frac{\left(1074\,\frac{kg}{m^3}\right)\left(0.0610\,\frac{\mathrm{m}}{\mathrm{s}}\right)}{0.00433\,\frac{Ns}{m^2}} = 15130\,\frac{1}{m}$$

$$\frac{\partial Re}{\partial \mu} = -\frac{\bar{\rho}\overline{D_h}\overline{u_m}}{\bar{\mu}^2} = -\frac{\left(1074\,\frac{kg}{m^3}\right)(1.17\times10^{-3}m)\left(0.0610\,\frac{\mathrm{m}}{\mathrm{s}}\right)}{\left(0.00433\,\frac{Ns}{m^2}\right)^2} = -4088\,\frac{1}{\frac{Ns}{m^2}}$$

$$\frac{\partial Re}{\partial \rho} = \frac{\overline{D_h}\overline{u_m}}{\bar{\mu}} = 0.0165\ \frac{kg}{m^3}$$

By its components:

$$\left(u_{flow\ rate}\right)^2\left(\frac{\partial Re}{\partial \mathrm{u_m}}\right)^2 = \left(0.000362\,\frac{m}{s}\right)^2\left(290\,\frac{m^{-1}}{s}\right)^2 = 0.01102$$

$$\left(\sigma_{\mathrm{D_h}}\right)^2\left(\frac{\partial Re}{\partial \mathrm{D_h}}\right)^2 = (2.05\times10^{-5}\ m)^2\left(15130\,\frac{1}{m}\right)^2 = 0.0962$$

$$\left(\sigma_{\mu}\right)^2\left(\frac{\partial Re}{\partial \mu}\right)^2 = \left(7.42\times10^{-6}\ \frac{Ns}{m^2}\right)^2\left(-4088\,\frac{1}{\frac{Ns}{m^2}}\right)^2 = 9.20\times10^{-4}$$

$$(\sigma_\rho)^2 \left(\frac{\partial Re}{\partial \rho}\right)^2 = \left(3.15 \times 10^{-2}\ \frac{kg}{m^3}\right)^2 \left(0.0165\ \frac{m^3}{kg}\right)^2 = 2.70 \times 10^{-7}$$

Reinserting the components into the full equation:

$$Re_{channel}|_{TSM} = \sqrt{(u_{flow\ rate})^2 \left(\frac{\partial Re}{\partial u_m}\right)^2 + (\sigma_{D_h})^2 \left(\frac{\partial Re}{\partial D_h}\right)^2 + (\sigma_\mu)^2 \left(\frac{\partial Re}{\partial \mu}\right)^2 + (\sigma_\rho)^2 \left(\frac{\partial Re}{\partial \rho}\right)^2}$$

$$Re_{channel}|_{TSM} = \sqrt{0.01102 + 0.0962 + 9.20 \times 10^{-4} + 2.70 \times 10^{-7}}$$

$$Re_{channel}|_{TSM} = 0.329$$

The total uncertainty in the calculated apparent Fanning friction factor can now be calculated as:

$$Re_{channel} = 17.7 \pm 0.329$$